Investigation of the industrial NH3 oxidation by CFD simulations including detailed surface kinetics

Wiser, Artur

(2020)

Investigation of the industrial NH_3 oxidation by CFD simulations including detailed surface kinetics

TECHNISCHE
UNIVERSITÄT
DARMSTADT

Vom Fachbereich Chemie
der Technischen Universität Darmstadt

zur Erlangung des Grades
Doktor-Ingenieurs (Dr.-Ing.)

Dissertation
von Artur Wiser
aus Kursk

Erstgutachter:	Prof. Dr.-Ing. Herbert Vogel
Zweitgutachter:	Prof. Dr. Martin Votsmeier

Darmstadt 2020

Artur, Wiser: Investigation of the industrial NH3 oxidation by CFD simulations including detailed surface kinetics
Darmstadt, Technische Universität Darmstadt,
Jahr der Veröffentlichung der Dissertation auf TUprints: 2020
URN: urn:nbn:de:tuda-tuprints-172087
Tag der Einreichung: 08.09.2020
Tag der mündlichen Prüfung: 21.10.2020

Die vorliegende Arbeit wurde in der Zeit vom **Januar 2014** bis **August 2018** im Fachbereich Chemie am Ernst-Berl-Institut für Technische und Makromolekulare Chemie der **Technischen Universität Darmstadt** unter der Leitung von **Herrn Prof. Dr.-Ing. H. Vogel** angefertigt.

Teile der vorliegenden Arbeit sind bereits veröffentlicht oder auf Tagungen präsentiert worden:

Vorträge

Investigations of Industrial NH3 Oxidation by Computational Fluid Dynamics Simulations including Detailed Surface
251st ACS Spring National Meeting,

2016 San Diego, USA

Why does Industrial NH3 Oxidation require Complex Gauze Structures?
5th International Conference on Structured Catalysts and Reactors

2016, San Sebastian, Spain

Investigations of Industrial NH3 Oxidation by CFD Simulations including Detailed Surface
XXII International Conference on Chemical Reactors CHEMREACTOR-22

2016, London, Great Britain

Poster

Why does Industrial NH3 Oxidation require Complex Gauze Structures?

A CFD Study using Mechanistic Kinetics

Jahrestreffen Reaktionstechnik 2016,

2016, Würzburg, Germany,

Investigation of industrial NH3 Oxidation by CFD Simulation.

Computational and experimental based study of ammonia oxidation in bench scaled reactor.

International Combustion institute summer school 2016,

2016, Bensheim, Germany,

Flow simulation of Ammonia Oxidation over Complex industrial gauzes using detailed surface kinetics

ESCRE 2015 – European Symposium on Chemical Reaction Engineering,

2015, Fürstenfeldbruck, Deutschland

Flow simulation of ammonia oxidation over complex industrial gauzes using detailed surface kinetics

48. Jahrestreffen Deutsche Katalytiker,

2015, Weimer, Deutschland

Zusammenfassung

Das Ostwaldverfahren ist das gängige Verfahren zur Herstellung der Salpetersäure. Die Ammoniakoxidation ist der erste Schritt dieses Verfahrens. Dabei wird Ammoniak bei Temperaturen zwischen 850 – 910 °C - katalysiert durch Platin-Rhodium-Netze - zu NO oxidiert. Bei dieser Reaktion treten Stickstoff (N_2) und Lachgas (N_2O) als Nebenprodukte auf. Die Bildung von N_2O ist besonders kritisch und soll soweit wie möglich verringert werden, da es nicht nur die Selektivität des gewünschten Produkts (NO) herabsetzt, sondern auch ein starkes Treibhausgas ist, welches zur Erderwärmung beiträgt.

Aufgrund der großen industriellen Bedeutung des Ostwaldprozesses gibt es viele und umfangreiche Grundlagenarbeiten, die in ihrer Mehrzahl auf das Verständnis des chemischen Reaktionsmechanismus ausgerichtet sind. Die Ammoniakoxidation ist eine massentransferlimitierte Reaktion. Erstaunlicherweise gibt es, trotz der Vielzahl an publizierten Grundlagenarbeiten, nur sehr wenige Ansätze, die den Effekt des Stofftransportes berücksichtigen [War 2013, Kli2017b] und keine Arbeiten, die die vorhandenen Reaktionsmechanismen in einer Strömungssimulation eines Reaktors mit aufgelösten katalytischen Platinnetzen gekoppelt modellieren. Aber nur eine kombinierte Betrachtung von Oberflächenmechanismus, Strömungsdynamik sowie Stoff- und Wärmetransport erlauben ein realistisches Bild der Ammoniakoxidation unter industriellen Bedingungen. Ein Anliegen dieser Arbeit ist es, diese Wissenslücke zu schließen.

Hier wird ein Modellierungsansatz vorgestellt, bei dem ein aus der Literatur bekannter kinetischer Mechanismus in einer CFD-Simulation unter Verwendung von Look-up Tabellen implementiert wird. Folgende Anwendungsfelder für solche CFD-Simulationen werden in der vorliegenden Arbeit behandelt:

- Der Einfluss der Geometrie von katalytischen Netzen auf die Selektivitäten der Reaktionsprodukte.
- Der Einfluss der Oberflächenrestrukturierung des Katalysators auf die Selektivitäten der Reaktionsprodukte.
- CFD-Simulationen eines Ammoniakoxidationslaborreaktors mit ortsaufgelösten Katalysatornetzen.

Viele Katalysatorproduzenten behaupten, dass die Netzgeometrie die Produktselektivitäten bei der Ammoniakoxidation beeinflussen kann. Es existieren hierzu zurzeit noch keine wissenschaftlichen Studien, die diesen Einfluss systematisch untersucht haben.

In dieser Arbeit wurden zum ersten Mal katalytische Platin-Rhodium-Netze mittels CFD Simulationen mit komplexem kinetischem Mechanismus der Ammoniakoxidation untersucht. Dabei wurden reale industriell eingesetzte gestrickte und gewebte Netzgeometrien berechnet. Die Ergebnisse können wie folg zusammengefasst werden:

- Die CFD-Simulationen zeigen ein realistisches Konzentrations- und Temperaturprofil im Katalysatorpaket.
- Die N_2O Selektivität variiert entlang des Perimeters. An der vorderen Seite des Drahtes werden höhere N_2O Selektivitäten beobachtet.
- Der Winkel, unter welchem die Strömung auf den Draht trifft, beeinflusst die N_2O Selektivität.
- In einer komplexen industriellen Netzgeometrie weisen einzelne Drähte unterschiedliche Produktselektivitäten auf. Diese werden von der Position des Drahtes in der Netzgeometrie und somit von lokalen Massentransferkoeffizienten beeinflusst.
- Letztendlich zeigt sich, dass moderne dreidimensionale Stricknetze in der Simulation bessere N_2O Selektivitäten aufweisen, als zweidimensionale Webnetze.

Ein weiteres Kapitel dieser Arbeit wurde dem Einfluss der Oberflächenrestrukturierung des Katalysators (Wachstum der Blumenkohlstrukturen) während der Ammoniakoxidation gewidmet. Zu diesem Zweck wurde ein CFD-Modell entwickelt, welches auf computertomographischen Aufnahmen basiert. Damit konnte die reale restrukturierte Oberfläche des Katalysatordrahtes in einer Strömungssimulation abgebildet werden.

Die Simulationsergebnisse zeigen, dass die Produktselektivitäten auf der Katalysatoroberfläche nicht uniform sind, sondern mit der lokalen Position variieren. Die N_2O Selektivitäten auf den Auswüchsen der Blumenkohlstrukturen sind höher als die am Drahtkörper. Außerdem beteiligen sich die Auswüchse stark an der Reaktion, so dass die restliche Katalysatorfläche einen relativ geringen Einfluss auf die Reaktion hat. Diese Erkenntnisse zeigen, dass zwischen Simulationen mit glatter und solche mit restrukturierter Oberfläche ein signifikanter Unterschied besteht.

Für die Anpassung der rechnerisch einfacheren glatten Netzmodelle wird in dieser Arbeit ein Oberflächenfaktor eingeführt, der die Reaktionsraten so anpasst, dass die Ergebnisse der Modelle von restrukturierten und glatten Drähten übereinstimmen. Das komplexere Model

mit restrukturierter Oberfläche muss daher nur einmalig erstellt und gerechnet werden. Basierend auf diesen Ergebnissen kann ein Oberflächenfaktor für die Modelle mit glatten Drähten bestimmt und validiert werden, sodass für weitere Arbeiten einfachere und schnellere Simulationen mit der glatten Katalysatoroberfläche durchgeführt werden können.

Im Abschlusskapitel dieser Arbeit wird ein Modell eines Laborreaktors erstellt und gerechnet. Bei diesem Reaktormodell werden einzelne Katalysatordrähte (100 μm Durchmesser) im Laborreaktor mit einem Durchmesser von 30 mm aufgelöst. Darüber hinaus wird ein detailliertes kinetisches Modell für die Reaktion an der Katalysatoroberfläche eingesetzt.

Die Ergebnisse der Simulationen auf der Netzskala zeigen, dass die N_2O Selektivität stark von den Strömungsbedingungen abhängig ist. Die verschiedenen Drähte beeinflussen das Strömungsfeld und somit auch den Massentransfer, was zu unterschiedlichen Produktselektivitäten an verschiedenen lokalen Stellen des Netzes führt. Diese Beobachtung unterstützt die Erkenntnis, dass eine Optimierung der Netzgeometrie zu effektiveren Katalysatoren für den industriellen Einsatz führt.

Auf der Reaktorebene zeigen die Simulationen, dass erhöhte N_2O Selektivitäten in Bereichen nah der Reaktorwand beobachtet werden. Die Katalysatortemperatur an diesen Stellen wird durch Wärmeverluste gesenkt, was die Kinetik der Reaktion in Richtung des Nebenproduktes N_2O verschiebt. Die Simulationsergebnisse von Modellen mit unterschiedlichen Reaktordurchmessern haben gezeigt, dass die Größe, der von dem Wärmeverlust betroffenen Zone, gleich bleibt. Daraus folgt, dass in einem industriellen Reaktor mit einem Durchmesser von mehreren Metern diese Randzone kaum eine Rolle spielt, wohingegen bei einem typischen Laborreaktor mit einem Durchmesser von wenigen Zentimetern die Selektivitäten stark von den Wärmeverlusten beeinflusst werden.

Darüber hinaus bieten mehrskalige Reaktorsimulationen die Möglichkeit, kinetische Mechanismen auch bei nicht perfekten Reaktoren zu validieren. Dabei werden die Unvollkommenheiten des Reaktors in einem Modell mit aufgenommen und simuliert. So können im nächsten Schritt die Modellergebnisse mit den Laborergebnissen verglichen und validiert werden.

Abstract

In the Ostwald process ammonia is catalytically oxidized to NO at short contact times on platinum/rhodium gauzes. Besides NO as main product, N_2 and N_2O are also produced. Especially the formation of N_2O is critical because of its large environmental influence as greenhouse gas.

Motivated by its large industrial importance, substantial fundamental research has been directed towards the mechanistic understanding of the process. The individual steps contributing to the overall reaction have been studied in numerous surface science studies [Reb2002, Sch2005, Kra2008]. Furthermore, a number of mechanistic kinetic models have been published based on the surface science information [Off2206]. More recently, the individual steps of the mechanism were studied by quantum mechanical methods and a surface kinetic model was assembled based on this work [Nov2008].

Surprisingly, despite all this fundamental research, there seems to be very little number of published works [War2013, Kli2017b] which consider the effect of mass transfer limitation and no published work that applies the existing reaction mechanisms in a flow simulation of the platinum gauze reactor. This is even more surprising, since the reaction is known to be strongly heat- and mass transfer controlled so that only a combined treatment of surface chemistry, flow, diffusion and heat conduction can reveal, in how far the existing kinetic models provide a realistic picture of ammonia oxidation under relevant industrial conditions.

This thesis describes a modelling approach where a mechanistic model of ammonia oxidation on platinum previously published by Kraehnert and Baerns was implemented in a CFD simulation using the rate mapping approach [Vot209]. Three main application fields for this modelling approach have been handled in this work:

- Geometry influence on the process performance of the catalytic gauze
- Influence of the catalyst surface restructuring on the process performance
- CFD modelling of the laboratory scale reactor including complex chemistry on the wire gauzes.

Since the ammonia oxidation is a mass transfer limited process, the influence of the geometry of catalytic gauzes have to play an important role for reaction product selectivity. Catalytic gauze suppliers suggested this since the establishing of knitted gauze types in the industry. Although very little scientific relevant studies has been made in this area (War2013).

Investigation of different wire and gauze geometries using the combination of CFD and detailed kinetics modelling can be summarized as follows:

- Realistic temperature (900 °C wire temperature) and concentration fields are obtained by the CFD simulation.
- On each single wire, the N_2O selectivity varies along the perimeter of the wire. The N_2O selectivity is highest on the front side of the wire and decreases towards the rear side.
- Thicker wires show a lower N_2O selectivity than thinner wires.
- The relative angle of the wire to the fluid flow has an influence on the product selectivity. Higher attack angle of the fluid on catalyst surface results in lower N_2O selectivity.
- In complex industrial gauze, the selectivity on the individual wires depends on the relative position of the wires in the gauze structure and is determined by local mass transfer effects.
- Finally, it is shown, that the simulation predicts a reduced N_2O selectivity for current industrial gauze designs, compared to conventional woven gauzes.

The next application field for coupled CFD and detailed kinetics modelling is the investigation of the role of catalyst surface reconstruction during the ammonia oxidation process. The surface of PtRh catalytic wires is originally smooth and became reconstructed during the reaction. So called “cauliflower” structures can be observed on used wires after several hour under reaction conditions. A CFD model based on computer tomography images has been developed for this investigation.

The simulations results show that the product selectivity (NO and N_2O) are not uniform of the restructured surface. The excrescences protruding in the reaction mixture are much stronger involved in the reaction and the selectivity of N_2O on these areas is much higher than on the wire body. It leads to a significant different between smooth wire and restructured wire models. Although it has been shown that a surface factor, which influence the catalyst surface concentration, for smooth wire models can be adjusted in a way to reproduce the results of restructured wire model. The complex restructured wire model has to be made and calculated just once to validate the surface factor, which can be implemented then for much more simple models with smooth wire surface.

The models of laboratory scale reactor demonstrate the feasibility of a wire scale resolved (wire diameter 100 μm) simulations of a full lab reactor (reactor diameter up to 30 mm) using surface kinetics.

On the gauze scale, it is observed that the N_2O selectivity is strongly influenced by the local flow conditions around the wire which leads to a variation of the local N_2O selectivity with the position on the gauze. The different wires in the gauze interact through their effect on the flow field which explains why the N_2O selectivity of industrial reactors can be improved by optimization of the gauze geometry. For example, a low N_2O selectivity is predicted where one wire shadows another, while high N_2O selectivity is predicted at stagnation points of the flow.

The reactor scale simulations show that an increased N_2O selectivity is expected in an outer zone of the reactor where the temperature is lowered by heat losses. Simulating reactors of different diameters, it is found that the size of the zone affected by the heat losses is independent of the reactor diameter. This means that for a typical lab reactor the N_2O selectivity is strongly influenced by the heat loss.

Furthermore, multi-scale simulations such as presented in this work might offer the possibility to validate kinetic mechanisms even with imperfect reactor data, by including the imperfections of the reactor in the model and then comparing lab measurements to the model predictions.

Danksagung

An dieser Stelle möchte ich mich bei allen herzlich bedanken, die zum Gelingen dieser Arbeit beigetragen haben. Mein besonderer Dank gilt:

Prof. Dr.-Ing H. Vogel für die Möglichkeit, diese Arbeit durchführen zu können, seine fachliche Unterstützung und sein Vertrauen. Ein besonderer Dank gilt Ihrer persönlichen, kontinuierlichen Betreuung und fachlichen Unterstützung über den gesamten Zeitraum der Arbeit.

Mein besonderer Dank für die wissenschaftliche Unterstützung in allen Phasen der Arbeit, den kontinuierlichen Informationsaustausch, die Übernahme des Korreferats und vor allem für das entgegengebrachte Vertrauen gilt Herrn Prof. Dr. Martin Votsmeier. Die zahlreichen Gespräche auf intellektueller und persönlicher Ebene werden mir immer als bereichernder und konstruktiver Austausch in Erinnerung bleiben.

Herrn Prof. Dr.-Ing. A. Drochner für die seine zahlreichen Ratschläge und die fruchtbaren Diskussionen.

Des Weiteren gilt mein Dank Herrn Dirk Born (Umicore), der als Projektleiter immer mit mannigfachen Ideen mich fachlich unterstützt und mir einen kritischen Zugang zu dieser Thematik eröffnet hat.

Allen Kollegen des Arbeitskreises für die gute Zusammenarbeit.

Ganz besonders möchte ich mich bei meinen Eltern Victor und Natalia Vizer bedanken. Speziell bin ich für ihre Geduld, Rücksichtnahme und für die unaufhörliche Unterstützung in aller Hinsicht dankbar.

An letzter, doch eigentlich an erster Stelle möchte ich meiner Ehefrau Evgeniya danken. Vornehmlich bin ich für unsere gemeinsamen Gespräche, ihre Hilfe in Wort und Tat, für ihre Rücksichtnahme und uneingeschränkten Aufmunterungen sowie für jede einzelne Umarmung in der schwierigen Endphase dieser Dissertation dankbar.

Für meine Familie

List of symbols

Symbol	Description	Value/unit
A	Area	m^2
a	Specific surface	m^{-1}
c	Molar concentration	mol m^{-3}
c_p	Molar heat capacity at constant pressure	J mol^{-1} K^{-1}
d	Diameter	m
D	Diffusion coefficient	m^2 s^{-1}
e	Specific internal energy	J kg^{-1}
E_A	Activation energy	J mol^{-1}
f	Volume force	N kg^{-1}
$\Delta_R H^{\ominus}$	Standard enthalpy of reaction	J mol^{-1}
$\Delta_f H^{\ominus}$	Standard enthalpy of formation	J mol^{-1}
$\Delta_R h$	Specific heat of reaction	J kg^{-1}
$\Delta_R H$	Enthalpy of reaction	J mol^{-1}
$\Delta_f H$	Enthalpy of formation	J mol^{-1}
J	Molar flux	mol m^{-2} s^{-1}
j_D	Chilton and Colburn J-factor heat transfer correlation	
j_H	Chilton and Colburn J-factor mass transfer correlation	
k	Rate constant	
k_b	Bolzmann constant	1.38 e-23 J K^{-1}
Le	Lewis number (Sc/Pr)	

M	Molar mass	kg mol^{-1}
$\dot{m}$	Mass flow	kg s^{-1}
μ_{12}	Reduced mass of two gas molecules	
n	Rate exponents	
p	Partial pressure	Pa
Pr	Prandtl number	
σ	Collision diameter	
$\dot{q}$	Specific heat source term	W kg^{-1}
$\dot{\Theta}$	Rate of change of the surface coverage	s^{-1}
$\dot{Q}$	Heat source term	W m^{-3}
R	Universal gas constant	8.314 J mol^{-1} K^{-1}
r	Surface reaction rate	mol m^{-2} s^{-1}
Re	Reynolds number	
s	Mass source term	kg $m^{-3}s^{-1}$
S	Momentum source term	N kg^{-1}
S	Selectivity	
Sc	Schmidt number	
Sh	Sherwood number	
$T^{\ominus}$	Standard temperature	298.15 K
T	Temperature	K
t	Time	s
T_{ref}	Reference temperature	385 °C

u	velocity	$m\ s^{-1}$
V	Volume	m^3
$\dot{V}$	Volume flow	$m^3\ s^{-1}$
w	Mass fraction	
X	Conversion	
α	Permeability	m^{-2}
β	Forchheimer coefficient	m^{-1}
β	Mass transfer coefficient	$m\ s^{-1}$
η	Dynamic viscosity	Pa s
θ	Surface coverage	
κ	Thermal conductivity	$W\ m^{-1}\ K^{-1}$
ξ	Volume viscosity	Pa s
ρ	Density	$kg\ m^{-3}$
τ	Residence time	s
τ_{ij}	Normal/shear stress	$N\ m^{-2}$
υ	Stoichiometric coefficient	
υ_i	Empiric diffusional volume	
Ω_{12}	Collision integral	

Table of contents

1. Introduction

Nitric acid is one of the most important commodities in the chemical industry. The annual worldwide production is estimated as more than 80 mio. tons a year with a market value of around US$ 15 billion. Nitric acid is used, for example, as intermediate for the production of adipin acid for further processing to nylon polymers. But the largest (80 %) part is used for production of nitrogen fertilizers [Hay2018]. A continuing growth of the earth population requires a fast increase in production of food. Consequently, the demand in synthetic, nitrogen- based fertilizers will always grow.

Nitric acid is produced in the Ostwald process, which has been industrially established for more than 100 years. In the first step of the process, ammonia is oxidized to a meta-stable nitrous oxide (NO) in a heterogeneously catalyzed reaction. Knitted and woven gauzes made of platinum sand platinum alloys are mostly used as catalyst. In the next step, NO is further oxidized to NO_2 and then NO_2 is absorbed in water to nitric acid. Especially interesting from the reaction engineering point of view is the first step of the process – oxidation of ammonia. As mentioned before, the process was successfully used in the industry for more than a century, nevertheless ammonia oxidation is far from being completely understood. The reaction is driven by mass and heat transfer phenomena under industrial conditions. The mass transfer and kinetic phenomena cannot be investigated separately by laboratory experiments because those effects are overlaying and the isolation of them is nearly impossible.

Therefore, ammonia oxidation can be a very good example for investigating it “in-silico” by means of computer modeling. Nowadays, powerful computers and fast algorithms give us a possibility to carry out very complex, reality-near models. For example, in computational fluid dynamics (CFD) simulations the kinetic and mass transfer effects can be modeled and their influence on the process can be investigated. In this way, different published reaction kinetics can be modeled together with mass transfer effects under industrial reaction conditions.

Another industrially significant aspect is the geometry of the catalytic gauzes, which can influence the reaction performance. Nowadays there are no scientific based criteria for designs of catalytic gauzes. In this case CFD modeling of different gauze geometries can bring significant benefits for catalyst manufactures.

The next, not completely understood, process during the ammonia oxidation is the restructuring of the catalyst surface during the reaction. These phenomena lead not only to

the change of surface morphology but also to an unrecoverable loss of platinum and decline of catalysts mechanical stability. Models based on tomography images of used catalytic wires and CFD can reveal valuable information about the restructuring process and the influence on the reaction performance.

In this contribution the main focus is given to the investigation of different geometries of industrial gauzes and their influence on the ammonia oxidation process. The models incorporate both a complex industrial geometry as well as detailed reaction kinetics. Another important aspect addressed in this work is the combination of CFD modeling with geometries based on tomography images.

Summarizing all the aspects, an approach has been created in this work to investigate and better understand the ammonia oxidation process by means of modern computer-based technologies.

2. Motivation and scope of this work

Ammonia oxidation is the first step of the Ostwald process for the production of nitric acid. Although the process has been developed by the German chemist Wilhelm Ostwald at the beginning of 20th century, since that time only minor changes have been done in the industrial technology. The first step, the ammonia oxidation, has a quite good performance, yielding about 95-97 % of the desired product NO. Nevertheless, one of the undesired reactions leads to a building of nitrous oxide (N_2O), which is a very strong greenhouse gas (300 times stronger compared to CO_2). Nowadays, there exist technologies to destroy produced N_2O in secondary or tertiary steps of the process (e. g. SCR). Those technologies are expensive and require an additional catalyst, which can enable the decomposition of produced N_2O, but the reaction which leads to N_2O remains unchanged. The concentration of N_2O in the atmosphere is increasing from year to year. Figure 2.1 shows the global trend of N_2O concentration at different places in Germany [UBA2017].

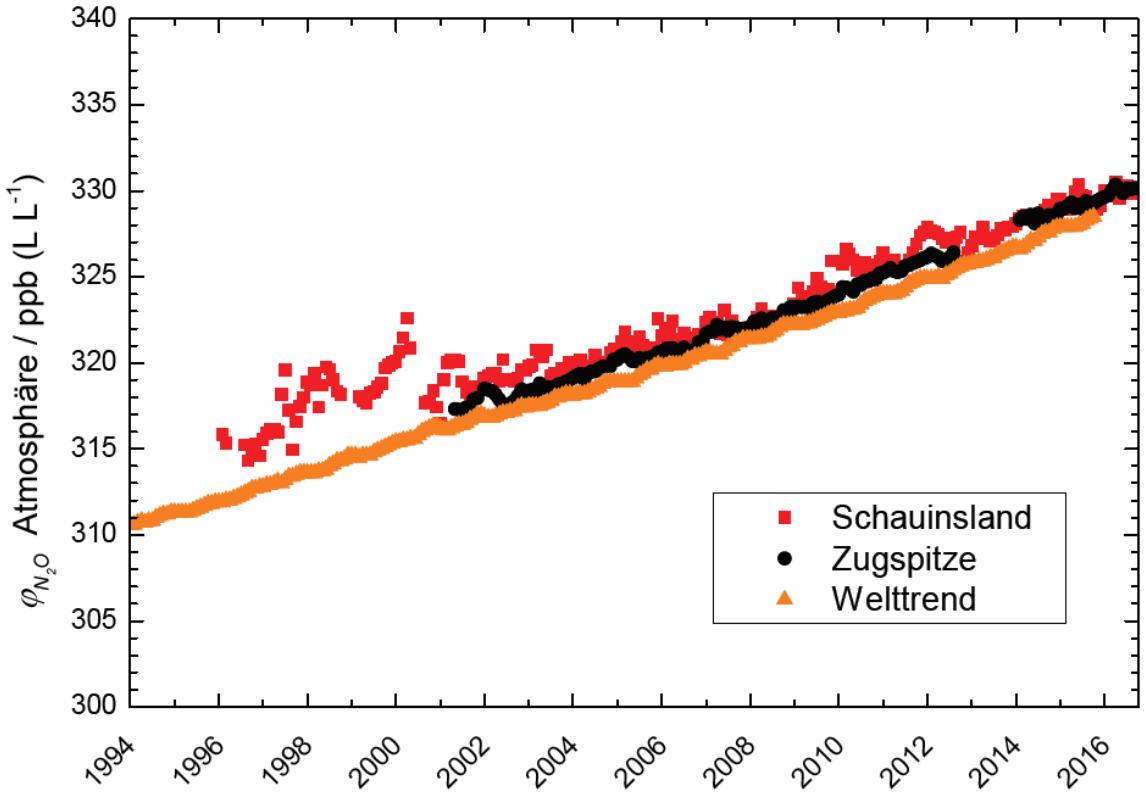

Figure 2.1: Concentration of N_2O in the atmosphere at different location. Messured from 1994 until 2016 [UBA2017].

Today application of knitted platinum (or platinum alloys with other metals) gauzes is state of the art in modern ammonia combustion reactors. The gauzes can have a very complex three-dimensional structure, and a reactor's catalyst package can consist of several types of gauzes. This should increase the NO yield and reduce the N_2O selectivity as well as the loss of expensive platinum, although the design of the catalytic gauzes is empirically based and doesn't have a solid scientific background.

An elegant and economical way for N_2O emission reduction during ammonia oxidation is to suppress the N_2O production directly on the catalyst. Such an approach requires a very good and deep understanding of the reaction process. Since the ammonia oxidation under the industrial condition is known to be driven by mass transport, only a combination of all ongoing steps during the reaction (mass transport toward the catalyst surface and reaction kinetic on the catalyst) can reveal a realistic picture of the process. The combined consideration of mass transfer and reaction kinetics can provide important knowledge, which can be used for the optimization of reaction condition and catalyst design.

Surprisingly, until now only a few attempts have been made for the modeling of ammonia oxidation reaction kinetics combined with mass transfer phenomena. Nowadays, the availability of powerful computers and fast algorithms makes it possible to perform computational fluid dynamics (CFD) simulations for such complex systems as ammonia oxidation. CFD modeling finds a very broad application in different scientific areas, reaching from aerodynamics to meteorology. The benefit of CFD modeling for the simulation of ammonia oxidation is the possibility to combine the calculation of chemical kinetics on the catalyst surface and fluid flow through the catalytic gauze. As already mentioned before, the ammonia oxidation under the industrial condition is driven by mass transfer. Therefore, the geometry of the catalytic gauze influences the mass transfer and consequently the reaction performance as well.

One of the targeted aims of this work is the implementation of CFD simulations with detailed reaction kinetics for the more scientific-based catalyst design and optimization regarding N_2O selectivity.

Another significant aspect of industrial ammonia oxidation on platinum gauzes is the unrecoverable loss of platinum due to the catalyst surface restructuring. On the one hand, this process causes high cost regarding the high platinum price, and on the other hand, it leads to a degradation of catalyst's mechanical stability. The development of metal prices used for ammonia oxidation catalyst is shown in the figure 2.2. Especially in case of high-pressure

plants, the platinum loss can rise to 0.4 g per tonne of 100 % nitric acid [War2013, Con1967]. Special palladium catchment gauzes can be installed after the catalytic gauzes for recycling of platinum and reduction of irreversible loss.

The restructuring process is not completely understood until now. The most supported scheme is the internal diffusion of Pt to the surface and its evaporation as volatile PtO_2. In the next step gaseous PtO_2 sublimes on colder wire regions, this leads to surface reconstruction and building of so-called “cauliflower” structures. The diameter and the catalytic performance of wires change hence to the restructuring process during the industrial production campaign.

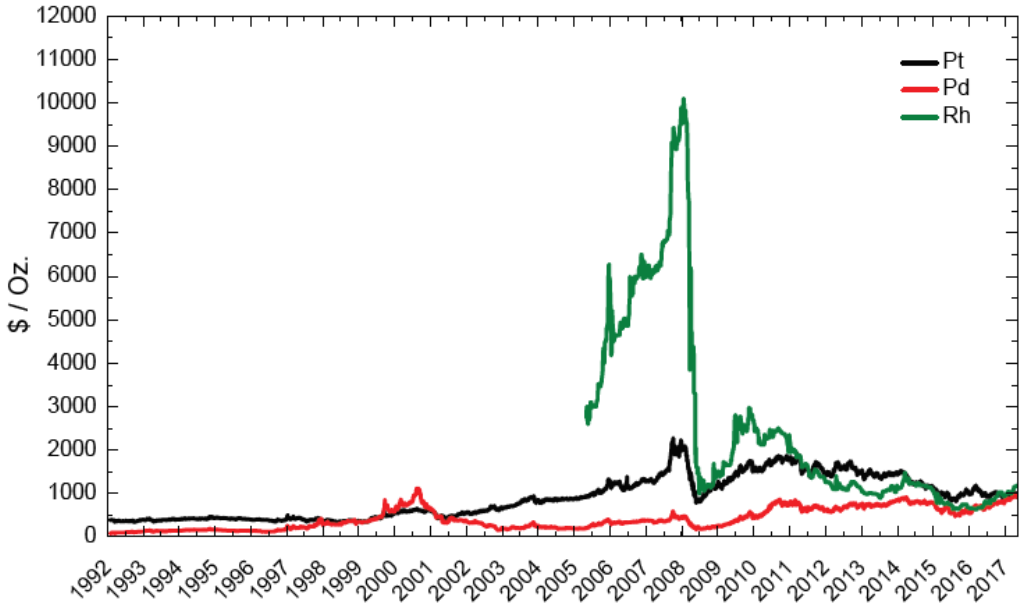

Figure 2.2: Price development from 1992 until 2017 for Oz. of Platinum, Palladium and Rhodium [Joh2017].

The modern computational tomography technology provides us with an opportunity to create a very realistic computational image of the reconstructed wire surface. This image can be transformed into a geometry, which can be used for CFD modeling. CFD models based on CT images and including the detailed chemical kinetics can reveal valuable information about the reconstruction process and the influence of this process on the reaction performance. This knowledge can help not only to better understand the reconstruction process but also how the surface reconstruction could be avoided or to develop better solutions for platinum recovery.

Such simulations have never been done before. Furthermore, they are very challenging regarding the geometry creation process and regarding computational power.

This work begins with a brief overview of the Ostwald process and ammonia oxidation technologies, describing the historical development and what's considered state of the art today.

The next part is a literature review covering the recent works on the ammonia oxidation process and catalysts. Firstly, the global kinetics of ammonia oxidation reaction is discussed. There exist several proposals for the kinetic mechanism ranging from 12 up to 44 elementary reaction steps. A brief review about the remarkable mechanisms is given as well.

The next part of the literature review considers the reconstruction of the catalyst surface during the reaction under industrial conditions. The published ways, of how the reconstruction and growing of so-called “cauliflower” structures develop is described there. Furthermore, a work is mentioned for imaging and investigation of reconstructed wires using computer tomography.

The last part of the literature review focuses mainly on recently published works about the modeling of ammonia oxidation. The first attempts of CFD modeling of ammonia oxidation have been done in the mentioned publications. Methods for the implementation of detailed chemical kinetics in CFD simulations and the validation of such simulations in laboratory reactor are described in works from Klingenberger, Teng-Wand and Heydt and Warner. The current contribution can be seen as follow-up research based on the aforementioned publications.

Then a short theoretical part follows, where the mathematical and computational methods are briefly described.

The results of the present work can be divided into three main chapters. In the first chapter, the development of CFD models based on complex industrial wire geometries is described. Some phenomena such as thermal radiation and the wire position in the reactor are investigated in this chapter. Moreover, a scientific explanation is given for the superior behavior of woven gauzes over knitted ones.

The second results chapter is dedicated to the reconstruction of the platinum wire surface during the ammonia oxidation. Here CFD simulations have been developed and performed considering real surface geometry after the reconstruction process. The geometry was created using tomography images of a part of the catalytic wire after being several hours in industrial ammonia oxidation reactor.

The third part describes the CFD simulation for a laboratory scale reactor, which has been built and tested by Heydt at TU Darmstadt. A comparison of reactors with 10 mm and 30 mm diameter has been drawn.

Furthermore, it is worthwhile to mention that three main parts of the results chapters are designed as alone standing publications with brief but specific introduction and conclusion sub-chapters.

The last chapter of the current contribution draws general conclusions about the performed research. Furthermore, it gives some suggestions for further development and implementation of computational fluid dynamics in the optimization of the ammonia oxidation process and catalyst development.

3. Theory

3.1. Ostwald Process

The heterogeneously catalyzed oxidation of ammonia with oxygen to nitrogen monoxide is the first step of the Ostwald process, which is broadly used for nitric acid production. Nowadays nitric acid is one of the largest commodities in the chemical industry. The annual production is about 55 million tons with the majority used for inorganic fertilizers such as ammonium nitrate and calcium ammonium nitrate. A minor amount is used for the production of explosives and adipic acid (Fig 3.1.).

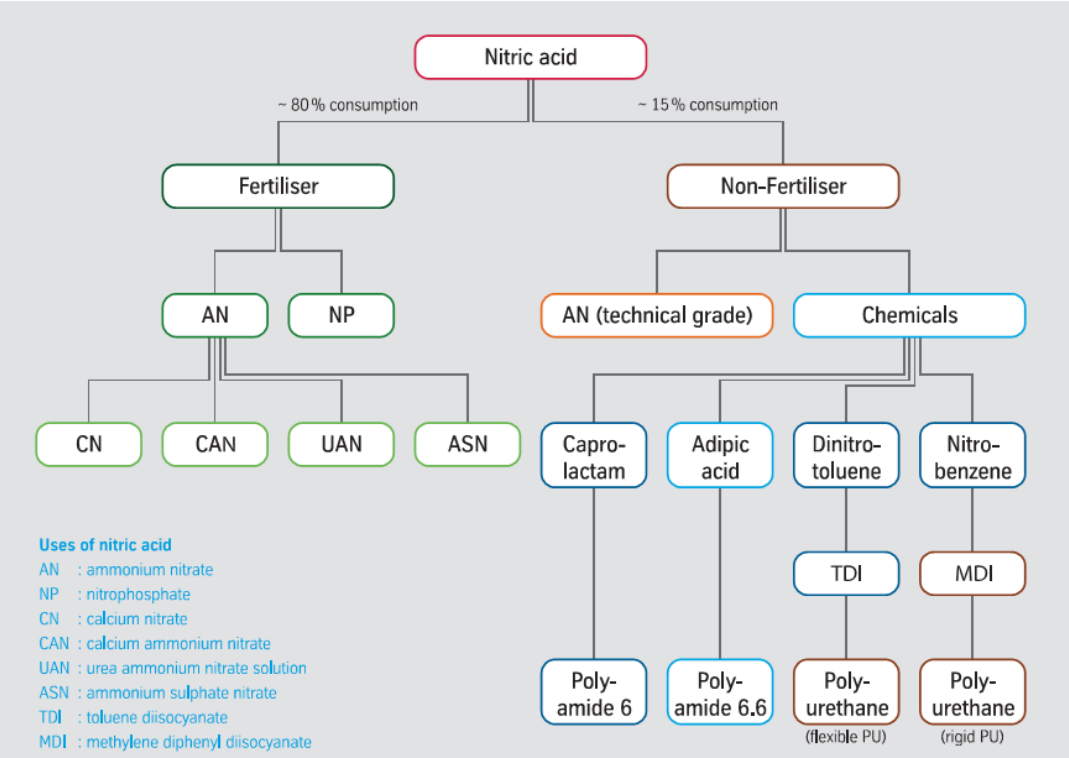

Figure 3.1: Uses of nitric acid in fertilizer and non-fertilizer Industries [tkIS2017].

The Ostwald process is divided into three reactions. In the first step, gaseous ammonia is converted with atmospheric oxygen over a Pt/Rh catalyst, yielding nitric oxide and water.

$$4NH_3(g) + 5O_2 \rightarrow 4\,NO(g) + 6\,H_2O(g) \qquad \Delta_R H^{\ominus} = -904\ kJ\ mol^{-1} \qquad \text{Reaction. 3.1}$$

Therefore, the selectivity toward NO is very high and amounts over 95 %; some undesirable byproducts are formed by following side reactions 3.2 and 3.3:

$$4NH_3 + 3\,O_2 \rightarrow 2\,N_2 + 6\,H_2O \qquad \Delta_R H^{\ominus} = -1260\ kJ\ mol^{-1} \qquad \text{Reaction. 3.2}$$

$$2\,NH_3 + 2\,O_2 \rightarrow N_2O + 3\,H_2O \qquad \Delta_R H^{\ominus} = -736\ kJ\ mol^{-1} \qquad \text{Reaction. 3.3}$$

After passing the catalyst, the reaction mixture is rapidly quenched to prevent the decomposition of metastable NO. The nitrogen monoxide forms NO_2 with excess or supplied oxygen by the following reaction 3.4. NO_2 can dimerize to dinitrogen tetroxide.

$$2\,NO\,(g) + O_2(g) \rightarrow 2NO_2(g) \qquad \Delta_R H^{\ominus} = -1127\ kJ\ mol^{-1} \qquad \text{Reaction. 3.4}$$

$$2\,NO_2\,(g) \rightleftharpoons N_2O_4(g) \qquad \Delta_R H^{\ominus} = -58\ kJ\ mol^{-1} \qquad \text{Reaction. 3.5}$$

The last step of the Ostwald process is the reactive absorption of nitrogen dioxide and dinitrogen tetraoxide in water. The reaction mechanism in the gas phase is very complex and contains several species and intermediates, so only the main route is described by the following reaction 3.6:

$$3NO_2(g) + H_2O \rightarrow 2\,HNO_3(aq) + NO(g) \qquad \Delta_R H^{\ominus} = -138\ kJ\ mol^{-1} \qquad \text{Reaction. 3.6}$$

The overview of the whole nitric acid process can be seen in the following block diagram (Figure 3.2):

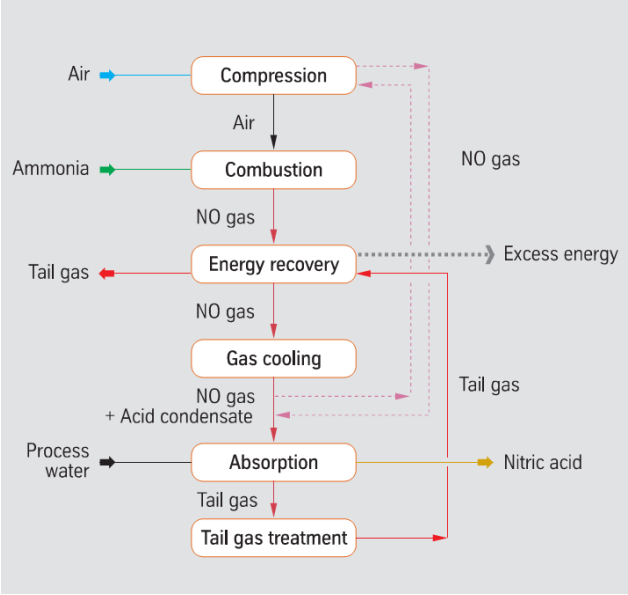

Figure 3.2: Block diagram of the Ostwald process [tkIS2017].

3.2. History

The knowledge of nitric acid production exists since the Middle Ages. First, successful attempts to convert ammonia and oxygen to nitric acid were carried out in the 1780s[t], the fact of using platinum as a catalyst for this process is documented in 1824 [Mit1953, Hen1824, War2013]. Industrial production of nitric acid was based on sodium nitrate (Chile saltpeter) at the end of nineteenth and early twentieth century. In the same period, there were several attempts to produce nitrogen monoxide by direct combustion of air in an electric arc. This process was developed by Birkeland and Eyde but due to poor energy efficiency (combustion temperature > 2000°C), it has been abandoned. The energy requirement was about 60 000 kWh electrical energy per tonne of fixed nitrogen, which corresponds to the burning of 20 tonnes of coal. [Jes2013]. In 1900, Wilhelm Ostwald began his work on the catalytic conversion of ammonia with air oxygen to nitrogen monoxide using platinized asbestos [Mit1953]. The ammonia became highly available since the beginning of industrial production by Haber-Bosch processes. Already in 1906, the first industrial facility with a capacity of 300 kg d^{-1} nitric acid came on stream [Thi2000]. Curled platinum ribbons were used as a catalyst in the first Ostwald plants. The platinum loss in such plant was very considerable (about 3%), which was the reason for the high production cost of nitric acid [War2013]. The next major change in the process came with the development of platinum gauze as the catalyst for ammonia oxidation. This development was introduced by the investigation of Karl Kaiser in 1911. Ostwald showed that NO yield was increased by reduction of residence time or contact time of reaction mixture with the catalyst. Exploiting this fact, Kaiser proposed a gauze catalyst of 0.06 mm diameter wire made from platinum. Such a type of catalytic gauze was used in the industry until the 1990s [And1926, And1926a,War-2013].

Further process changes were introduced by the development of high and double pressure plants due to the wide availability of stainless steel. According to the principle of Le Chatelier, it is evident that the oxidation of NO, as well as the adsorption of NO_2, are favored by high pressure. Firstly, increasing the operating pressure leads to smaller absorber equipment. Secondly, it reduces the required residence time for the oxidation of NO to NO_2. Rise of the operating pressure from 1 bar to 8 bars reduces the required residence time by a factor of 512 [War2013, Chi1968]. Nowadays, three different types of single pressure process can be distinguished:

- low-pressure plants (1-3 bar),
- middle-pressure plants (3-7 bar)
- high-pressure plants (8 -14 bar).

More recently, dual-pressure plants have been developed. In such a kind of plant, the combustion is carried out by middle pressure (4-6 bar) and the absorption by high pressure (9-12 bar). The last major change in the process was the replacement of woven platinum gauzes with knitted in the early 1990's. The catalyst manufacturers, as well as nitric acid plants operator, claimed following benefits by using knitted gauzes:

- faster manufacturing of the gauze
- the decrease in the platinum losses
- the increase in the combustion efficiency [Hor1991, Hor1993].

Although there exists almost no academic studies, which can clearly explain improvements to the combustion efficiency and catalyst performance [War2013].

3.3. Operating conditions and thermodynamics

The following stability diagram (Figure 3.3) of the main reactions of the Ostwald process can describe the thermodynamics of the nitric acid production.

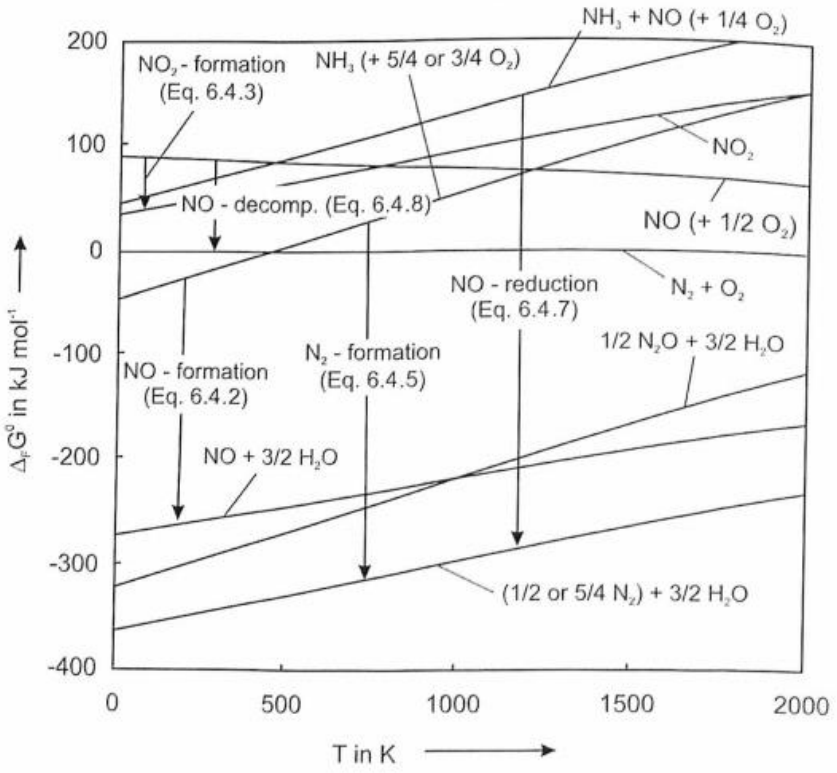

Figure 3.3: Stability diagram of main reactions of nitric acid process [Jes2013].

The stability diagram is a graphical representation of standard Gibbs function ($\Delta_F G^0_{products}$ and $\Delta_F G^0_{educts}$) of formation of all reaction participants. The thermodynamically favoured reaction can be easily identified - $\Delta_F G^0_{products}$ should be below the $\Delta_F G^0_{educts}$. The following observation can be done:

- NO, N_2 and N_2O are thermodynamically favoured products of ammonia combustion.
- The production of N_2 is an undesired reaction and is more favoured than the production of NO. The selectivity of the catalyst plays a large role in favouring NO and suppressing N_2.

- NO can decompose by the operating temperature (~900 °C). It is important to cool the reaction mixture rapidly below 700 K. At this temperature, NO is metastable and decomposition does take place.

Produced NO can be reduced by NH3, so it is important to maintain high gas velocities (1-3 m/s) and short contact time (~1 ms) with the catalyst to suppress the NO reduction.

The Table 3.1 represents the typical operating conditions for ammonia oxidation by different design pressures. For a better understanding of the process conditions the most important of them are described more detailed below.

Table 3.1: Process conditions of nitric acid plants [Jes2013].

Process parameter	Atmospheric pressure	Medium pressure	High pressure
Pressure / bar (abs)	1.0	2.5 - 6.5	7.0 – 12.0
Catalyst temperature / °C	820 - 860	840 - 900	890 – 930
Preheating temperature of the feed gas / °C	30 - 60	140 - 210	>210
Number of catalyst gauzes	3 - 6	5 - 12	>12
Gross loss / mg t^{-1} HNO_3 (100%)	50 - 80	80 - 200	200 - 350
Average NO-selectivity / %	95 - 98	93 - 97	90 - 93
Campaign length / days	300 - 450	120 - 300	70 – 120
Specific load / t N(NH_3) m^{-2} day^{-1}	2 - 6	6 - 17	<35
Gas velocity / m s^{-1}	1.2 – 1.8	1.8 – 2.5	3 - 8

The basic trends needed for an understanding of the process are described in following. The temperature of the first gauze plays a major role and the factors, which can influence it are described below.

Wire temperature: the surface temperature of the catalytic wire can be described by the following equation 3.1 [War2013]:

$$T_w \approx T_{in} + \frac{D_{NH_3}}{\lambda} \cdot c_{NH_3,bulk} \cdot \Delta_R H \qquad \text{Eq. 3.1}$$

T_w is the wire temperature, T_{in} is the temperature on the reactor inlet, $D_{NH_3}$is the diffusion coefficient of ammonia, λ is the thermal conductivity, $c_{NH_3,bulk}$ is the inlet ammonia concentration and $\Delta_R H$ is the reaction enthalpy.

All the quantities of equation 3.1 are depended on wire temperature, with only one exception of inlet temperature. The solution of this equation is not obvious and can become very

complex. Still, it can give a good picture about the relationship of wire temperature with other process parameters.

Inlet Temperature: Higher inlet temperature leads to a higher wire temperature. It is noteworthy that the temperature of the first wire is higher than the temperature after the catalyst. It is specially the case if the Lewis number (ration of thermal diffusivity to mass diffusivity) is below 1. [War 2013].

Composition: A higher ammonia concentration in the feed leads to a higher bulk concentration and gives rise to wire temperature.

Gas velocity/gauze loading: Linear gas velocity in the reactor, mass flux or residence time does not influence the wire temperature. It can be explained by the fact, that two factors cancel each other. The boundary layer around the wire decreases with higher gas velocity, which makes the ammonia transport to the catalyst more efficient but on the other hand, it eases the heat release from the catalyst surface [Nie2013, Kli2017a].

Pressure: According to the Eq 3.1 pressure does not influence the wire temperature.

The dependencies of the NO selectivity on the process parameters are given by Warner and can be summarized as follows:

- The NO selectivity is a function of the mass transfer coefficient (which incorporates the burner loading and gauze type), the inlet ammonia and oxygen concentrations, and the gauze temperature.
- Pressure does not affect the selectivity to N_2 but does affect the N_2O selectivity. Increasing pressure reduces the selectivity to the desired product because of Le Chatelier's principle. Warner showed with a more detailed thermodynamic examination, that this is not the case in the given system. He claims that the decrease in NO selectivity with increasing pressure is due to the promotion of N_2O formation [Thi2000; War2013].
- NO, and N_2O are not decomposed on the gauze at an appreciable rate. Warner checked this thesis with two methods: Firstly, he placed additional gauzes downstream and secondly, he added NO and N_2O to the feed. Neither NO or N_2O were decomposed in both cases.
- The gauze geometry and type can improve the selectivity toward NO and suppress the N_2O formation. At the same burner loading, a larger wire diameter and

fractional open area will increase the NO formation and decrease the N_2O selectivity [War2013, Nie2013, Kli2017a].

3.4. Catalyst

Although several noble and non-noble metals, as well as oxide catalyst, have been tested for ammonia combustion, the best catalytic performance show platinum gauzes. Today, the last is used almost exclusively. Only in some east Europe nitric acid plants exist metal oxide honeycomb catalysts, which are implemented as a secondary catalyst in the burner after several platinum gauzes [Van2006]. Co_3O_4 and Zr-Co-O are considered as an active component in such catalytic systems. The advantage of oxide catalyst is the low price, but the conversion of ammonia is lower comparing to platinum-based catalyst, and the vulnerability of poisoning is increased [Thi2000, Per2003].

The most used form of catalyst is woven or knitted gauzes. The wires diameter varies form 0.06 mm until 1 mm. Since the introduction of knitted gauzes with a complex 3-dimensional geometry, the woven gauzes have been almost completely vanished from the market. About 90 % of the platinum gauzes used for ammonia combustion today are knitted ones. The catalyst distributors claim improvements in the mechanical, as well as catalytic properties of this kind of gauzes. Nowadays, there are a large number of different types and gauzes geometries from a different manufacturer. The figure 3.4 shows some types of knitted and woven gauzes.

Furthermore, there exists a broad variety of the catalytic alloys for ammonia combustion. Most common are alloys of Platinum and Rhodium in a fraction of 90/10. With the addition of Rh, the mechanical stability as well as the melting point of the alloy increase, this leads to a lower platinum loss. Ruthenium and Palladium can be used as additional components as well. It is claimed that such alloys have better catalytic performance and mechanical durability compared to a common Pt/Rh catalysts [Handorth, Hay2018].

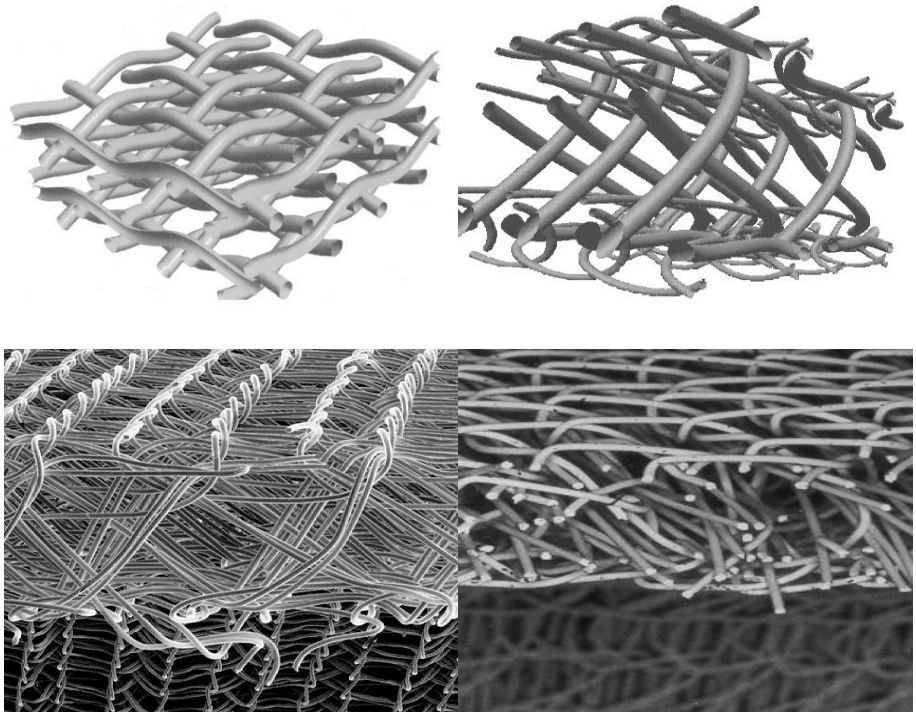

Figure 3.4: An example of woven gauze geometry; **top right**; a multinit geometry from Umicore; down **left and right**: microscope photography of multinit gauzes.

3.5. Reaction induced surface morphology restructuring

The morphology of the catalytic wire changes during the campaign. The restructuration occurs due to high temperature, pressure, and interaction with reactants. This process, called in the literature as “catalytic etching” is observed during other catalytic reactions such as oxidation of hydrogen, ethane, and propene as well. At the beginning, already after few hours, the formation of parallel facets on the surface of the catalyst is observed (by SEM, figure 3.5). This step is followed by a growing of so-called “cauliflower structures” on the wire surface, which leads to an increase of the catalysts surface area and enlargement of the wire diameter. Formation of such cauliflower structures is accompanied by a continuous loss of platinum in the form of volatile platinum oxide. Generally, the platinum loss is caused by abrasion and vaporization, whereas the latter is predominant. In case of a Pt-Rh catalytic wire, the platinum oxide is more volatile as rhodium oxide.

.

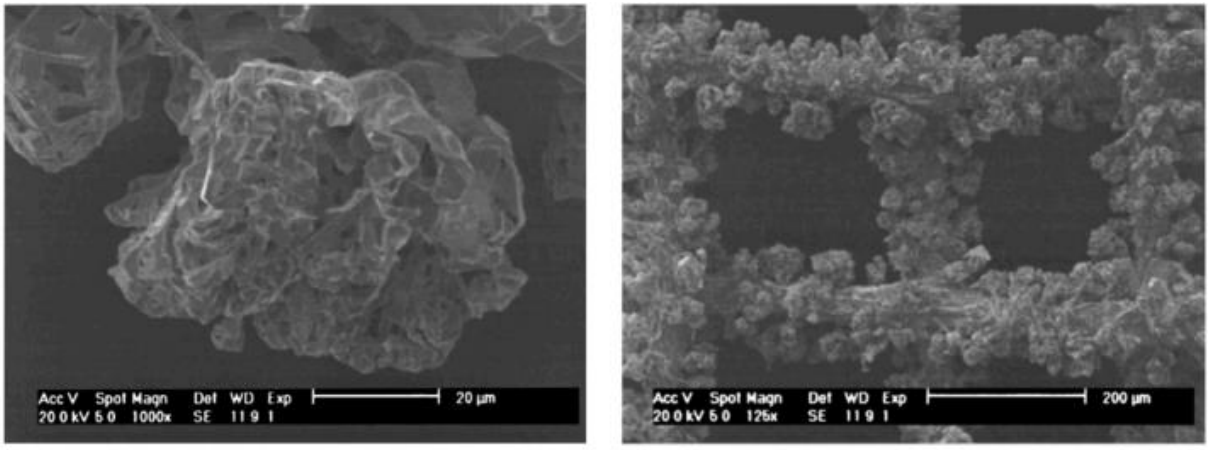

Figure 3.5: Reconstruction of platinum catalytic gauze by cauliflower grow. (a) Single cauliflower excrescent, (b) morphology change of the surface of several wires in the catalytic gauzes [Nil2001].

Consequently, the fraction of Rh increase with time and especially in the tips of cauliflowers. That leads to a change in the mechanical and catalytic properties of wires. Due to long-term mechanical degradation of the catalyst, the geometrical form of the gauze can collapse. Platinum gauzes have to be changed frequently each 6-12 months depending on the plant, operation condition, and catalyst form. So-called catchment gauzes made of palladium are installed downstream of Pt-Rh catalytic gauzes. Parts of the volatile precious metal (up to 60 %) can be captured and recovered by such gauzes.

3.6. Computational Fluid Dynamics

Computational fluid dynamics (CFD) is a field of fluid mechanics that uses numerical methods and algorithms to solve problems concerning the flow of a fluid by evaluating approximate solutions of the governing flow equations. CFD is based on numerical discretization methods such as finite volume method (FVM), finite element method (FEM) and finite difference method (FDM). Most CFD software uses finite volume method. Although finite element method is used to tackle fluid mechanical problems, nonetheless this method finds mostly application in numerical structural mechanics. One of the advantages of FVM is the guarantee for the conservation in every finite control volume, whereas the FEM provides continuity only for the whole problem area [Sch1990]. Concluding, simulations based on FVM cannot provide results with strong errors in mass conservation (mass accumulation or mass destruction), which is especially beneficial for CFD simulation including chemical reactions. Although modern CFD codes based on FEM (e.g., Comsol Multiphysics) can handle this problem using special algorithms.

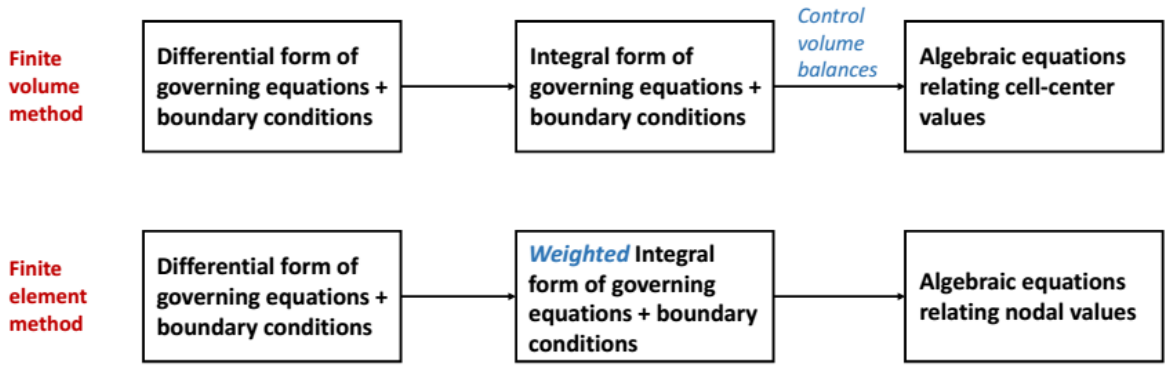

Figure 3.6: General differences in finite volume and finite element methods [Edx2015].

The development of powerful computers and fast algorithms allowed numerical solutions of very complex problems already in the 1960s. One of the most important areas, where CFD calculations promised a very big advantage was within aerospace engineering. There was a demand for extension of the classical aerodynamic experiments (e.g., wind tunnel), which were very expensive and difficult to perform, by numerical methods because of the prevalence of commercial aircraft transport and space programs. This situation, a need in the precise description of physical phenomena in fluid flow by numerical methods and the accessibility of computational power provided fast development in computational fluid dynamics methods and codes. Nowadays, CFD is used in nearly every domain of engineering, where the fluid flow is important. To mention a few examples: aerospace, automobile, naval engineering, chemical reaction engineering, biological and anatomical systems, meteorology and many more [Hen2012].

The following scheme (Fig. 3.6) summarizes the general approach of CFD simulations. In the first step, governing equations shall be defined, so the physical problem is expressed by mathematical equations. In the second step, the area (geometry) in which the mathematical problem shall be addressed is defined. This continuous area is discretized into a finite number of elements, which are used for the creation of nodes on edges or faces of these elements. In the next step, the differential equation system is transformed into an algebraic system. The following step is the numerical solution of the obtained algebraic system on the nodes of the geometry. To obtain values between the nodes interpolation of the functions values of those nodes can be performed.

Simplifying, the method can be described as following: instead of finding analytical solutions for functions describing continuously in space and time a certain quantity (velocity, pressure,

temperature), the CFD approach calculates approximate values of these quantities on a finite number of points within the space and on selected time points.

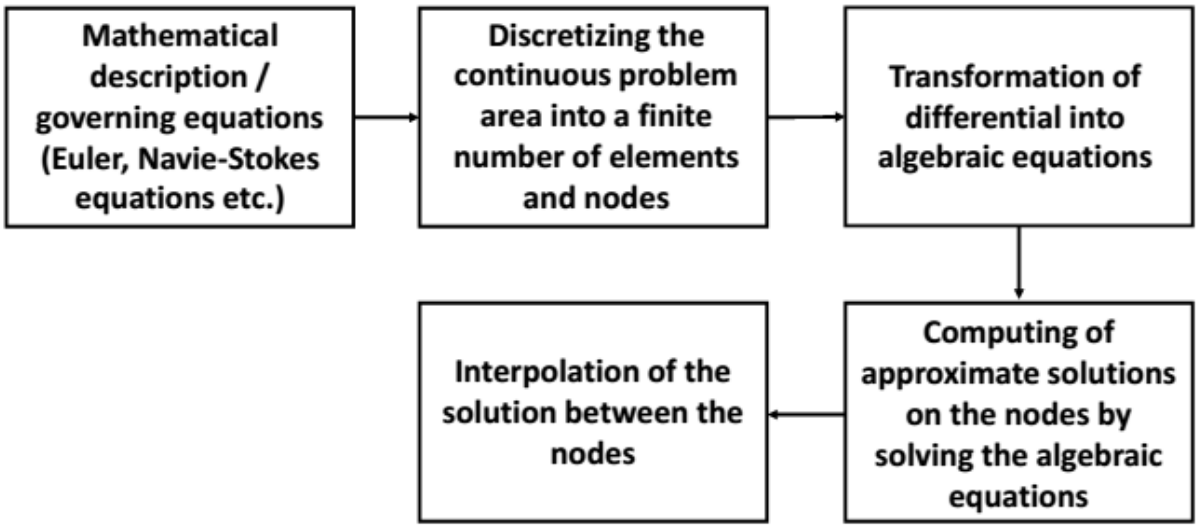

Figure 3.7: General scheme of a CFD method.

3.7. Governing equations

The Navier-Stokes equations are the governing equations in CFD to describe the viscous fluid's motion. Mathematicians and physicists Claude Louis Henri Navier and George Gabriel Stokes derived these equations in the 19th century independently. The equations describe the balance of momentum applying Newtons' second law to the motion of a fluid, concerning also its inner friction (viscosity). Depending on the addressed problem, Navier-Stokes equations can be simplified to minimize the computational effort for the solution. For example, neglecting of the fluid's inner friction (viscosity) leads to the Euler equation. Consideration of incompressibility and stationarity leads to Bernoulli's equation.

In differential non-conservative form Navier-Stokes equations describe the time rate of momentum change for a moving infinitesimal control volume as the sum over all forces that act on this control volume, i.e. pressure force, stress forces (shear and normal stresses) and external volume forces (gravity). In the three-dimensional coordinate system, the Navie-Stokes equations can be written as follows:

$$\rho \frac{Du_1}{Dt} = \rho \frac{\partial u_1}{\partial t} + \rho u_1 \frac{\partial u_1}{\partial x_1} + \rho u_2 \frac{\partial u_1}{\partial x_2} + \rho u_3 \frac{\partial u_1}{\partial x_3} = -\frac{\partial p}{\partial x_1} + \frac{\partial \tau_{11}}{\partial x_1} + \frac{\partial \tau_{21}}{\partial x_2} + \frac{\partial \tau_{31}}{\partial x_3} + \rho f_1 \quad \text{Eq. 3.2}$$

$$\rho \frac{Du_2}{Dt} = \rho \frac{\partial u_2}{\partial t} + \rho u_1 \frac{\partial u_2}{\partial x_1} + \rho u_2 \frac{\partial u_2}{\partial x_2} + \rho u_3 \frac{\partial u_2}{\partial x_3} = -\frac{\partial p}{\partial x_2} + \frac{\partial \tau_{12}}{\partial x_1} + \frac{\partial \tau_{22}}{\partial x_2} + \frac{\partial \tau_{32}}{\partial x_3} + \rho f_2 \quad \text{Eq. 3.3}$$

$$\rho \frac{Du_3}{Dt} = \rho \frac{\partial u_3}{\partial t} + \rho u_1 \frac{\partial u_3}{\partial x_1} + \rho u_2 \frac{\partial u_3}{\partial x_2} + \rho u_3 \frac{\partial u_3}{\partial x_3} = -\frac{\partial p}{\partial x_3} + \frac{\partial \tau_{13}}{\partial x_1} + \frac{\partial \tau_{23}}{\partial x_2} + \frac{\partial \tau_{33}}{\partial x_3} + \rho f_3 \quad \text{Eq. 3.4}$$

The velocity vector has components u_1, u_2, and u_3, p is the pressure, ρ is the density, τ_{ii} and τ_{ij} the normal and shear stresses and f_i the components of the volume force vector.

Stokes derived the following relationship for the normal and shear stresses for a Newtonian fluid (stress is proportional to the shear velocity):

$$\tau_{ii} = \left(\xi - \frac{2}{3}\eta\right) \nabla \vec{u} + 2\,\eta \frac{\partial u_i}{\partial x_i} \quad \text{Eq. 3.5}$$

$$\tau_{ij} = \tau_{ji} = \eta\left(\frac{\partial u_j}{\partial x_i} + \frac{\partial u_j}{\partial x_j}\right) \quad \text{Eq. 3.6}$$

∇ is the Nabla operator, η and ξ are the dynamic and the volume or bulk viscosity, where the latter accounts for the frictional losses due to expansion or compression of the fluid. For example, blood or honey are representative of non-newtonian fluids.

Combination of the equations 2.19 and 2.20 and the momentum balance yields the vector form of the Navier-Stokes equation, which can describe the motion of a viscous, compressible fluid:

$$\rho\left(\frac{\partial \vec{u}}{\partial t} + (\vec{u}\nabla)\vec{u}\right) = -\nabla \mathrm{p} + \eta \nabla \vec{u} + \left(\xi + \frac{1}{3}\eta\right) \nabla(\nabla \vec{u}) + \rho \vec{f} \quad \text{Eq. 3.7}$$

In CFD, the momentum equations are usually extended by balance equations of mass and energy.

The following equation 3.8 describes the mass balance (often referred to as continuity equation):

$$\frac{\partial \rho}{\partial t} + \nabla(\rho \vec{u}) = 0 \quad \text{Eq. 3.8}$$

The equation describes a fluid without any chemical reaction and concentration gradients. For chemical applications of CFD simulations, those two effects cannot be neglected. Therefore, it is necessary to look at the mass balance for each of the components of the fluid individually and extend the equation with terms accounting for the change of mass due to diffusion and reactions:

$$\frac{\partial \rho_i}{\partial t} + \nabla(\rho_i \vec{u}) = \nabla(D_i \nabla \rho_i) + s_i \qquad \text{Eq. 3.9}$$

Di is the diffusion coefficient of species i and s_i is the rate of change in mass of the ith species due to chemical reaction.

The energy equation can be expressed in differential non-conservative form as following:

$$\rho \frac{D}{Dt}\left(e + \frac{\overrightarrow{u^2}}{2}\right) = \rho\dot{q} + \frac{\partial}{\partial x_1}\left(k\frac{\partial T}{\partial x_1}\right) + \frac{\partial}{\partial x_2}\left(k\frac{\partial T}{\partial x_2}\right) + \frac{\partial}{\partial x_3}\left(k\frac{\partial T}{\partial x_3}\right) - \frac{\partial p}{\partial x_1} - \frac{\partial p}{\partial x_2} - \frac{\partial p}{\partial x_3} + \frac{\partial u_1\tau_{11}}{\partial x_1} + \frac{\partial u_1\tau_{21}}{\partial x_2} + \frac{\partial u_1\tau_{31}}{\partial x_3} + \frac{\partial u_2\tau_{12}}{\partial x_1} + \frac{\partial u_2\tau_{22}}{\partial x_2} + \frac{\partial u_2\tau_{32}}{\partial x_3} + \frac{\partial u_3\tau_{13}}{\partial x_1} + \frac{\partial u_3\tau_{23}}{\partial x_2} + \frac{\partial u_3\tau_{33}}{\partial x_3} \qquad \text{Eq. 3.10}$$

The rate of change of kinetic energy per volume and specific internal energy in a moving infinitesimal control volume is related to the following effects:

- the sum of a heat source term (radiation or heat of chemical reaction)
- heat conduction into the volume element (Fourier's second law, *k* is the thermal conductivity and *T* is the temperature of the fluid)
- pressure energies
- stress energies.

The equations system has six dependent variables (u_1, u_2, u_3, p, ρ, and T) and only five equations, due to that there is a need in an additional term for closing and solution of this system of equations. The equation of state is the last equation that can be added to this system. The equation of state describes the relationship between fluid's density, pressure, and temperature:

$$\rho = \rho(p, T) \qquad \text{Eq. 3.11}$$

In the simplest case, where an incompressible fluid is described, the density of the fluid does not depend on pressure and temperature, so the density is just constant.

$$\rho = const \qquad \text{Eq. 3.12}$$

For most of the liquids in a very broad range of conditions, a constant density is an appropriate approximation. Gases and gaseous systems cannot be treated in the same way. One of the possibilities for the description of the dependency of the density on pressure is the ideal gas law:

$$\rho = \frac{p\bar{\bar{M}}}{RT} \qquad \text{Eq. 3.13}$$

Here R is the universal gas constant and $\bar{M}$ is the mean molar mass of the gas. This simple equation 3.13 has only a limited validity and for more realistic description other more complex state equations should be used (Van-der-Waals, Peng-Robinson or Soave-Redlich-Kwong).

The previously mentioned six equations form a closed system of the coupled non-linear second-order partial differential equations system. Until now, an analytical solution has not been found for this equation system (one of the millennium problems). The modern software uses algorithms for the numerical solutions of the Navier-Stokes equations system.

3.8. Lookup Tabulation

The idea of lookup tabulation is to calculate and store the reaction rates in a pre-processing step for a wide range of reaction conditions instead of the solution of a complex equation system for chemical kinetics during the fluid flow simulation. The effective reaction rates can be obtained by interpolation in the lookup table, which contains the pre-calculated data. Using the lookup tabulation approach, it is possible to decouple the computation of fluid flow and the reaction kinetics, so the reaction rates can be calculated only once in a pre-processing step and can be retrieved for every CFD simulation containing the same chemical reaction mechanism. Usage of this approach for complex numerical simulations of reactive flows is widely spread in the field of gas-phase chemistry (e.g., CFD modeling of non-catalytic combustion). It was also successfully implemented for surface chemistry in case of methane oxidation on the platinum catalyst, resulting in three orders of magnitude faster simulations and a possibility of effective implementation of complex surface reaction kinetics into 3D reactor models [Vot2009].

The detailed description of the rate-mapping approach can be found elsewhere [Kli2017b, Vot2009]. Here only a short introduction will be given. The lookup tables containing the rate

data are calculated and built using the software Matlab. First, the input dimensions, which are influencing the source terms, should be defined. In case of ammonia oxidation, the dimensions are surface temperature and gas phase compositions of certain species. After that, a multidimensional, rectangular grid is created by dividing the input space by a certain number of breaks. In the next step, the source terms for each of the points in the grid are calculated. That data is used later during the CFD simulation as breakpoints for the spline interpolation. In this work, the method of cubic Hermite spline interpolation has been chosen. For this method, it is necessary to calculate the first partial derivatives of the source terms concerning all dimensions for every grid point. This is called “polynomial” representation of the rate data. The precomputed, corresponding spline functions are piecewise polynomials and representing the source terms. The coefficients (function values and derivatives) defining these functions are stored in the lookup tables. In this work, the logarithmic form of tabulated data has shown some advantages during the interpolation [Has2016].

The figure 3.8 shows a scheme for the routine, which is implemented for the compiling of CFD simulation with a lookup table interpolation.

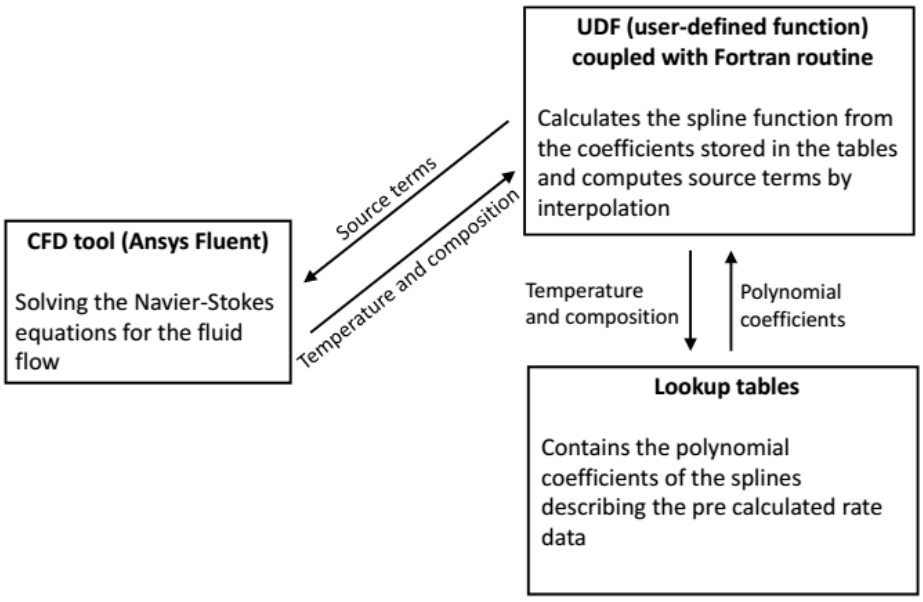

Figure 3.8: Scheme of the coupling of CFD simulation in Ansys Fluent with a lookup tabulation approach.

During CFD simulation, Ansys Fluent can interact with the lookup table using a user-defined function (UDF), which can be seen as an interface between Fluent and the interpolation routine. Fluent provides surface temperature and gas phase composition in every simulations step to UDF, which passes those data toward the Fortran routine. The Fortran routine can retrieve the polynomial coefficients from the stored grid points in the lookup table, construct the polynomials and perform the multidimensional spline interpolations. The source terms, which are the result of interpolation, are provided to Fluent. The advantage of Hermite splines in the above-described procedure is the use of only data on adjacent grid points for the interpolations and not data on the whole grid (that would be necessary in case of common spline interpolation).

The lookup tables in case of the simulations carried out in this work have four dimensions. Therefore, the interpolation procedure can be better described on an example with the 2D grid. In the figure 3.9, a simple 2D grid with four breakpoints in every dimension is shown. The grid consists of 16 nodes and nine elements. The function value and the first derivatives concerning all dimensions in that point are located on every node in the grid. The source terms on every grid element are described by a set of splines, defined by the coefficients stored on its surrounding nodes. Considering this fact, it is possible to use a successive one-dimensional interpolation along each direction, instead of a more computational expensive multivariate spline interpolation.

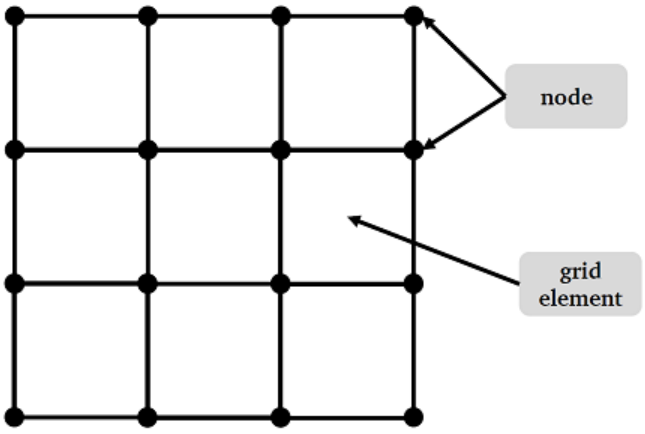

Figure 3.9: Example for a 2D rectangular grid with four breakpoints in each direction.

The interpolation scheme for a bivariate case can be described as following considering the figure 3.10:

For the interpolation of the data for the point P in a certain grid element, firstly, it is necessary to allocate the surrounding nodes (A, B, C, D). After that, the function value f at point E, between A and B, is evaluated using one dimensional cubic spline interpolation. Then the derivative df/dx^2 at point E is calculated using a simple linear interpolation of the derivatives. Point F between C and D can be found in the same way, evaluating functions value f and the derivative. The interpolation problem has been reduced to 1D with the calculation of points E and F. Now it is possible using the f and df/dx^2 from points E and F to perform another 1D cubic Hermite spline interpolation along EF to find the function value of P. The same procedure can be easily applied for more dimensional grids. The same algorithm should be repeated until the final function value can be found by using a single one-dimensional spline interpolation. [Kli2017b].

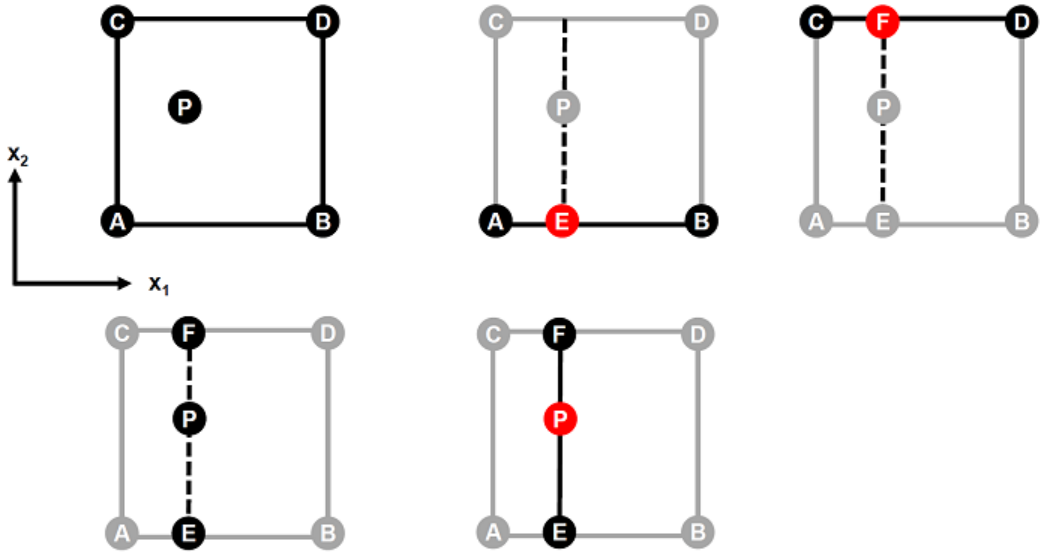

Figure 3.10: Procedure for the successive one-dimensional interpolation on a 2D rectangular grid element.

3.9. Computer Tomography

Micro-Computed tomography is a non-invasive X-ray based technique for 3D reconstruction of the opaque sample. The scanning object is placed between the X-ray source and the detector. By rotating the object, several images from different angels are recorded, corresponding to the projection of the linear attenuation coefficient. This coefficient is a measure for a fraction of photons absorbed or scattered per unit thickness of the absorber (scanning object). The modality employed in this activity, the difference between the linear attenuation coefficients of the different phases of the sample determines the contrast. Based on 2D projections, a 3D

volume can be reconstructed. Elemental digital units (voxels), which represent an intensity value of a signal in a 3D space, describe this volume. In case of two-phase samples (in our case this is platinum wire and surrounding atmosphere) the voxels can be distributed in solid and fluid elements by a segmentation process with a proper selected threshold value in the intensities histogram [Ran2014]. The results of the described procedure can be seen in the Figure 3.11.

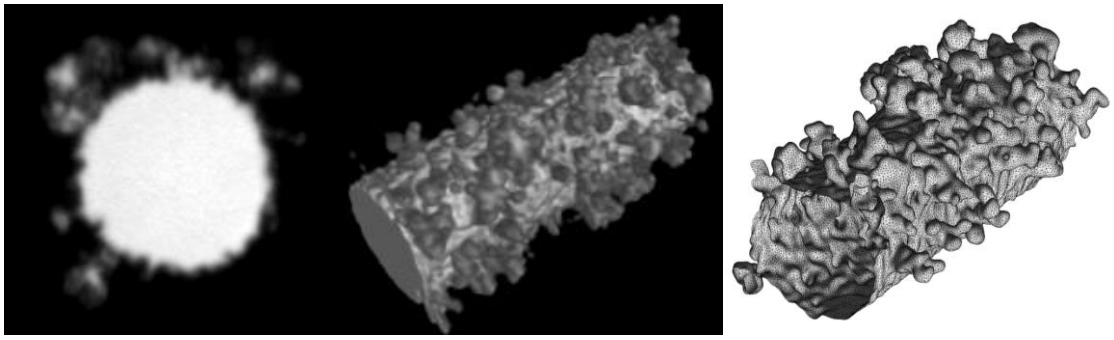

Figure 3.11: (a) a single CT image of the slice from restructured platinum wire (b) a reconstructed volume of the platinum wire (c) a computational grid (mesh) for CFD simulation.

It is possible to create a computational domain for CFD simulations based on the 3D reconstructed volume of the restructured wire produced by computer tomography. For this process Simpleware and ScanIP - special software for the handling of computer tomography images was used. ScanIP was also used for the creation of the computational grid (mesh) for CFD simulations in Ansys Fluent. The original 3D CT data were transferred to a stack of 2D pictures, which were produced by slicing the 3D data along the x-axis in a certain distance to each other as it can be seen in Figure 3.11 (a). The image stack was imported in Simpleware ScanIP and was stitched together resulting in a 3D CAD model. Sharp edges and islands of solid body were removed from the geometry by using implied filters within the software. The computational grid was created by ScanIP, resulting in a high-quality unstructured triangular mesh.

4. State of the art

In this chapter, the most relevant milestones in research of kinetics and mechanisms of ammonia oxidation reaction are given. A very comprehensive overview of investigation activities in this topic from the very beginning until the present is given in the Ph.D. thesis of Maximilian Warner from the University of Sydney [War2013]. Additionally, an overview is given about the last activities in the field of computer tomography and restructuring of platinum gauzes.

4.1. Heat and mass transfer

The ammonia oxidation reaction is controlled by mass transfer at industrial conditions (temperature above 600 °C). This fact has been proposed already in 1927 by Andrussov [And1927]. Surprisingly, this knowledge is neglected in a big number of mechanistic studies. Warner has pointed out, that a true mechanism can be achieved only by considering the interaction between a kinetic mechanism and mass transfer. There exists a range of methods for reaction modelling which can account for heat and mass transfer as well as the reaction kinetics. One of the most used approaches is the modelling of the heterogeneously catalysed reaction according to pseudo-homogeneous model. In such a model, the mass and heat transfer is described using the empirically determined coefficients.

Mass transfer is strongly dependant on the object geometry and to obtain a proper empirical data set the experimental studies have to be done for targeted geometries. In case of ammonia oxidation woven catalyst, which has a form of simple gauze, studies from Shah and Ahlström-Silversand can be used [Ahl1999, Sat1970, Sha1974, War2013]. But the aforementioned research cannot be transferred on cases of ammonia oxidation on complex knitted gauzes [And1927, And1927a]. Recently, the knitted gauzes, among others, were studied as well by Kolodziej, but the comparison of published data with other research shows relatively strong deviation.

Shah and Roberts propose the following relationship for the Chilton-Colburn j-factor ($j_{D,\gamma}$) and Reynolds number (Re_γ) for gauze screens [Sha1974]:

$$j_{D,\gamma} = 0.644 Re_\gamma^{-0.57} \quad 5 < Re_\gamma < 245 \qquad \text{Eq. 4.1}$$

The Chilton-Colburn j-factor represents the analogy between heat and mass transfer. Shah and Roberts have drawn the conclusion that the Reynolds number based on the wire diameter in a infinite wire model together with velocity are the best choice for the correlation of mass transfer data using Chilton-Colburn analogy. This analogy has been proved to be most accurate and was used in the work of Warner [War2013]. The correlation is valid for a wide range and gives a good agreement with the experimental data.

There exists another approach for the modelling of heat and mass transfer, which is getting more and more popular in today's science. It is computational fluid dynamics or CFD; this method treats the heat and mass transfer properly. Furthermore, using a CFD code, it is possible to couple heat and mass transfer as well as the detailed chemical kinetics in one model. It has already been done by Teng-Wang Nien [Nie2013] and Klingenberger [Kli2017b] for ammonia oxidation on simplified geometries (2D wires) and simply knitted gauzes. A CFD approach is more accurate as conventional models with empiric-based methods. But there is a need in the accurate model, which describes the binary diffusional coefficients of the components in the mixture. The binary diffusion coefficients can be calculated for each species using a kinetic gas theory [McG1991, Kee2003]:

$$D_{12} = \frac{3}{16 \cdot \pi \cdot P} \cdot \left(\frac{2 \cdot \pi \cdot k_B^3 \cdot T^3}{\mu_{12}} \right)^{1/2} \cdot \frac{1}{\sigma^2 \cdot \Omega_{12}^{(1,1)^*}} \qquad \text{Eq. 4.2}$$

This equation contains a collision integral ($\Omega_{12}^{(1,1)^*}$), k_B is the Bolzmann constant, μ_{12} is the reduced mass of two gas molecules and σ is the collision diameter. The collision integral for unipolar molecules is based on Lennard-Jones Potentials and on Stockmayer potential for polar ones. The derivation of these components for each pair of species in the mixture is quite challenging. For this purpose a semiempirical model from Fuller is widely used for the prediction of binary diffusional coefficients in the field of combustion CFD research, [Ful1966].

$$D_{12} = \frac{1 \cdot 10^{-8} \cdot T^{1,75}}{p \cdot \sqrt{\mu_{12}} \left[\left(\sum_1 v_i^{1/3} + \sum_2 v_i^{1/3} \right) \right]^2} \qquad \text{Eq. 4.3}$$

The model from Fuller is based on empiric diffusional volumes (v_i) and not on collision integrals. The diffusion volumes once calculated for a molecule can always be used in further calculations. But a waiver of temperature depended collision integrals leads to a quite narrow range of temperatures, where the Fuller model is valid. Therefore, binary diffusional coefficients in this work are calculated using the Chapman-Engskog theory. The coefficients

dependency of temperature has been compared with in the literature available experimental data [Mas1998, Mar1972, Zha2013, McG1991, Mar1972].

For the diffusion of a single species in a mixture ,the Steffan-Maxwell based equation is used [Mar1972]:

$$D_{i-mix} = \frac{1}{\sum_{\substack{j=1 \\ j \neq j}}^{N} \frac{X_j}{D_{ij}} \cdot \left(1 + \frac{X_i}{1 - X_i}\right)} \qquad \text{Eq. 4.4}$$

4.2. Kinetic models

The ammonia oxidation reaction is a subject of intensive research already since the beginning of XX century [And1926, And1928, And1928a]. In the early works from Andrussov, Bodenstein, and Raschig, some intermediates (nitroxyl, imides or hydroxylamines) have been proposed which are participating in the mechanism [And1926, And1926a, And1927, And1927a, And1928, And1928a, Bod1927, Bod1935, Bod1935a, Bod1941, Bod1942]. Since good spectroscopic methods are available, a number of studies in ultra-high vacuum have been done investigating the ammonia oxidation. Ammonia oxidation reaction has been carried out on single platinum crystals as well as on multi crystalline platinum foils and wires. The participation of the aforementioned intermediates has been disproved.

Modern surface science methods have been used for the investigation of the ammonia oxidation mechanism (Molecular Beam, SIMS, LEED, AES, TDS, EELS, (in-situ-)REM, XPS etc.). All those methods are used under low pressure (even UHV) conditions, which is a disadvantage because the production of N_2O under such conditions is not observable and can't be properly described by such kinetic mechanisms [Fog1964, Bra1995, Bra1997, Sch2003. Sch2003a, Sch2005, Sch2005a, Bae2005, Per2004, Per2004a, Per2005, Kon2005 Per2009, Ihm2007].

Studies based on density functional theory calculations provided additional information about the species participation in the reaction on various platinum planes [Bur2004, Bae2005, For2005, Imb2007, Nov2005, Nov2008, Raf2012, Wan2014].

The majority of the published kinetic mechanism of ammonia oxidation has not been tested on industrial conditions, where the reaction is mass transfer limited. High temperature, pressure, and flow rate, as well as an appearance of side products in a small amount, can be mentioned as reasons for this situation. CFD is a widespread tool for modeling combustion.

Although the coupling of detailed chemical kinetics and mass transfer is still a challenging approach, which has not been done, especially for ammonia oxidation, very often.

A very extensive list of published detailed mechanistic models for ammonia oxidation can be found in the theses of Warner. At this point, only a brief description of recent models is given. The special attention is given a model from Krähnert, which is used in most of the simulation in the present work.

4.2.1. Novell-Leruth

The model developed by Novell-Leruth et al. is based entirely on DFT calculation. The model consists of two versions. The first one is the full mechanism with 52 reactions, eight species, and 12 surface species. The second one is a reduced mechanism with 23 reactions, six species, and 11 surface species. The kinetic mechanism was calculated for Pt(1 0 0) phase [Nov2005, Nov2008].

4.2.2. Traversac

The proposed mechanism from Traversac et al. consists of 22 reversible reactions, seven gas species, and ten surface species (figure 4.1). The model was developed by using experiments in a platinum tube reactor at atmospheric pressure and in a temperature range of 200-1000 °C. A special point has to be mentioned; the mechanism is completely thermodynamic consistent because the reaction rates are calculated from the forward rates and thermodynamic properties of surface species. The backward rates are calculated using the van't Hoff equation. Furthermore, the model was tested in software packed CHEMKIN, where the gas phase reaction (using a kinetic model from Abo academy for gas phase combustion) is included. Overall, the provided model is a kind of puzzle consisting of different sub models, whose validity has not been proven independently. This might be a weak point in Traversac model. Although this model can be a very good base for optimizing the kinetic parameters to match experimental data because it is thermodynamically consistent and has all needed species [Tra2007].

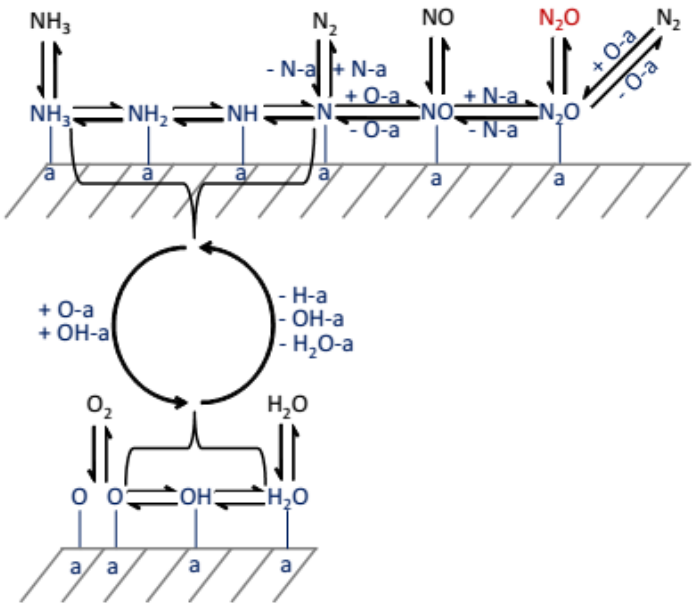

Figure 4.1: Kinetic mechanisms developed by Traversac [Tra2007, Image: Hey2018].

4.2.3. Scheibe

The reaction mechanism containing 12 reactions was developed for platinum faces Pt (5 3 3) and Pt (4 4 3), the experiments were carried out under ultra-high vacuum (Figure 4.2). The formation of N_2O was not detected experimentally and was not included in the kinetic mechanism, which is one of the biggest limitations of this model. Considering this fact, the mechanism cannot be used for the simulation of industrial ammonia oxidation [Sch2003, Sch2003a, Sch2005].

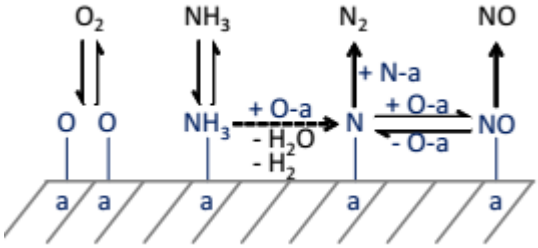

Figure 4.2: Kinetic mechanisms developed by Scheibe [Sch2005, Image: Hey2018].

4.2.4. Rafti

The mechanism from Rafti is a further development of the kinetic model proposed by Scheibe. The model considers Pt (5 3 3) phase and has 13 reactions including the formation of N_2O. The parameters were taken from DFT calculations and experiments upon 0.1 mbar pressure. This is higher than in the case of Scheibe model, but still, it is not the relevant pressure range for industrial ammonia oxidation. Although the included N_2O formation is a significant improvement of the Scheibe model, the modeling of this mechanism using a standard kinetic software might be very difficult. The reason for this is unconventional approaches for calculation of surface site in the mechanism. For example, some surface sites are predetermined only for adsorption of oxygen and coverage of nitrous oxide and oxygen are limited to certain thresholds [Kli2017b, Raf2012].

4.2.5. Rebrov

Rebrovs model contains 13 reactions and six surface species (Figure 4.3). The adsorption of educts takes place on two different platinum sites. The experimental validation was performed on the multi-crystalline platinum surface at atmospheric pressure and temperatures 523-673 K. The model developed by Rebrov is one of the first, where CFD models were used for estimation of the parameter for the kinetic mechanism. In the first step, a pseudo-homogeneous plug flow reactor model was used for the validation of experimental data. After that, a CFD simulation was used to find out, at which temperature the reaction becomes limited by mass transfer (573K). Then the relevant kinetic parameter was identified by sensitivity analysis and the CFD model was adapted to fit the experimental results [Kli2017b, Reb2001, Reb2002, Reb2003, Reb2003a].

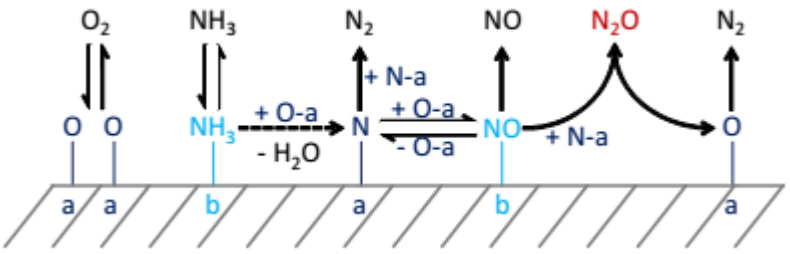

Figure 4.3: Kinetic mechanisms developed by Rebrov [Reb2002, Image: Hey2018]

4.2.6. Kraehnert

Kraehnert et al. developed a model for ammonia oxidation based on the Rebrov model (figure 4.4). The platinum phase Pt (1 1 1) (Rebrov Pt (1 0 0)) is considered in this model. Pt (1 1 1) is supposed to be thermodynamically most stable and is widely presented on metallic surfaces. Two adsorption sites are considered here. Ammonia molecules can adsorb on site “b” and all other species on site “a”. The experiments were performed in the temperature range of 286-385 °C and pressures between 1 and 6 bar in a micro-structured quartz reactor. The platinum foil was used as a catalyst. The model has ten reactions, six gas phase species, and six surface species. The parameters were fitted based on initial values from the literature. The production of NO doesn’t have a backward reaction because the decomposition of NO was not observed experimentally on Pt (1 1 1) phase. The striping of hydrogen atoms from adsorbed ammonia is described just by one reaction. Following this, hydrogen doesn’t appear as a surface- or gas-phase species [Kra2005].

Kraehnerts model can fit experimental values and describe the influence of feed composition on rates of product formation as well as the temperature effects. Only slight deviations for nitrogen production rates were observed.

The model from Kraehnert was later used in work from Scheuer et al. to describe the ammonia oxidation in an exhaust gas after-treatment system. Furthermore, the model was used by Nien et al. [Nie2013] for the modeling of ammonia combustion on platinum gauzes using CFD simulations. The detailed kinetic mechanism was coupled with CFD code with the help of Lookup tables. Klingenberger improved this approach. He used Kraehnerts kinetic mechanism as a benchmark in his work [Kli2017b].

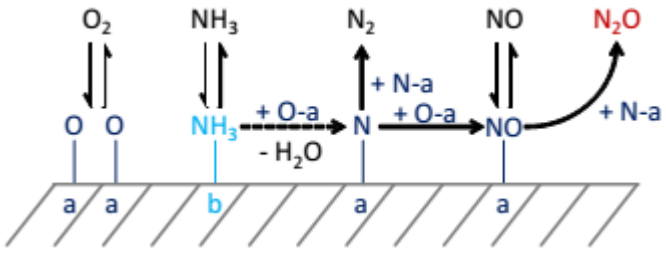

Figure 4.4: Mechanistic model from Kraehnert [Kra2005, image Hey2018].

4.3. CFD modeling of ammonia oxidation

Considering the fact, that the ammonia oxidation is limited by mass diffusion on industrial condition, there are surprisingly few published attempts to combine detailed reaction mechanism with sophisticated mass transfer model. As mentioned before, the CFD approach is perfectly suitable for such issues. Two works were published in the last two years where the ammonia oxidation is modelled using CFD code coupled with the detailed kinetic mechanism.

The first work is the Ph.D. thesis from Klingenberger; there the main point is the development of a toolbox for the computational interpolation of multivariate reduced Hermite splines. This toolbox was tested for the creation of tabulated data for the ammonia oxidation kinetic mechanism postulated by Novell-Leruth. The look-up tables were used for the calculation of surface source terms, which were linked to a CFD code. The model described a platinum wire gauze pack. Using this approach, it was possible to perform a complex calculation involving detailed kinetics and mass transfer model. The kinetic mechanism showed an unrealistic behavior by the accounting of mass transfer limitations. Very high N_2O formation, due to NO decomposition, was observed.

Furthermore, an extended degree of rate control and sensitivity analysis was performed for the determination of reaction steps, which were responsible for the product distribution under industrial (mass transfer limited) conditions. Resulted temperature and products profiles are shown in the figure 4.5. Then a parameter estimation was done and revealed that the activation energy of three of the four relevant reactions should be increased. It was then concluded that the Pt (1 0 0) surface is not a suited model for the industrial ammonia oxidation under realistic conditions. In conclusion, the work of Klingenberger demonstrated how the combination of detailed kinetic mechanism and CFD (including high sophisticated mass transfer model) could be used for the verification of postulated mechanisms under industrial conditions [Kli2016].

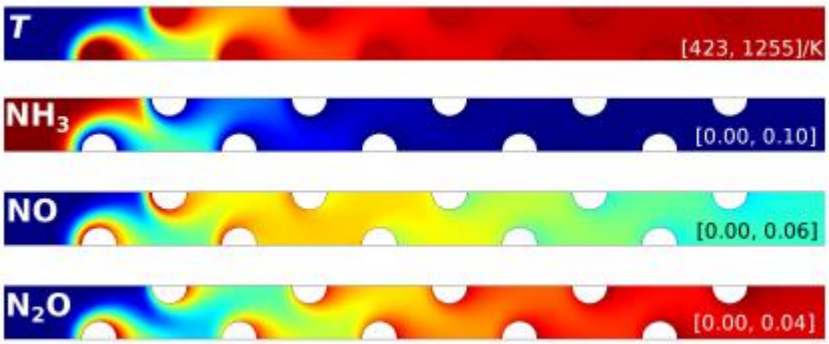

Figure 4.5: Temperature and mole fraction fields from a detailed CFD simulation with the implemented kinetic mechanism from Novell-Leruth [Kli2016].

The second remarkable work was done by Nien Teng-Wang at the University of Alberta in Edmonton in collaboration with Umicore. Nien developed a computational model for a gauze type ammonia oxidation reactor using the same approach as Klingenberger. The calculation of fluid dynamics and detailed reaction mechanism from literature (Kraehnert) were combined using look-up tabulation. A parametric study was done including the influence of wire diameter, the arrangement of wire in the computational domain as well as temperature effects. The simulations were performed on two and three-dimensional geometries. It was shown that the selectivity toward reaction products is strongly dependant on catalyst geometry. The selectivity toward undesired N_2O varies from wire to wire in a catalyst package as well as around the wire perimeter. It was found that N_2O selectivity on front areas of the wire is higher as in the rear areas (Figure 4.6). It was a very important step toward understanding how the gauze geometry influences the performance of the industrial ammonia oxidation. Therefore, the catalyst geometries used for simulations in work of Nien is simplified and differs very strongly from current industrially used woven gauzes.

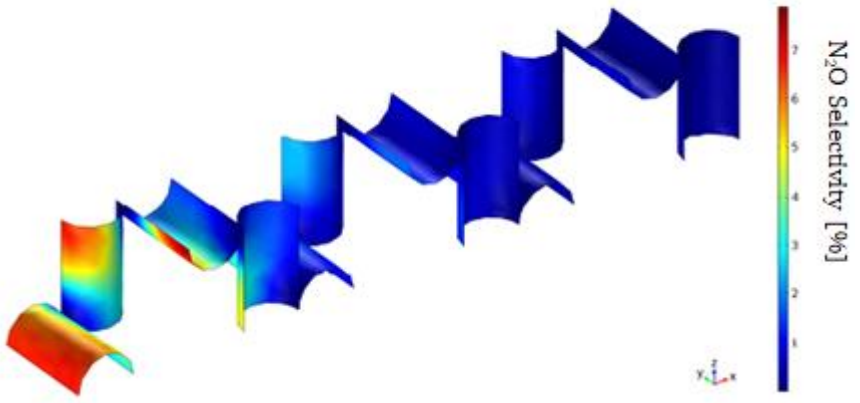

Figure 4.6: Contour plot of N_2O selectivity [%] along the catalytic wire in the 3D domain [Nie2013]

More recently, Heydt, in his Ph.D. thesis, investigated ammonia oxidation under industrial conditions experimentally using a bench-scale reactor. Furthermore, he supported his experimental work with CFD modeling. He compared experimental results from reactors with 10 and 30 mm diameter, where knitted platinum gauzes were used as a catalyst with CFD simulations. The computational domains of CFD simulations were very similar to geometries of lab scale reactors. CFD models were able to describe experimental trends in the reaction in a correct way. But absolute values from experiments and models differ from each other. There are several possible explanations for such deviation: simplification in the computational domain, an incorrect description of turbulence, used kinetic model, which has been validated only for low temperatures, etc. Furthermore, an attempt was done to perform experimentally a test on simplified geometries, which can be described computationally without such effort to compare models including gauzes packages. In this case, experiments and models showed significant deviations [Hey2018].

4.4. Surface restructuring of Pt-catalyst.

The smooth catalyst surface undergoes heavy reconstruction during the first hours of operation in the ammonia oxidation reactor. It was shown that this process starts on the grain boundaries and soon the entire surface is covered by “cauliflower”-like excrescences [Han2005]. This phenomenon leads to increase in wire diameter and surface area but is accompanied by mechanical degradation of catalyst and loss of expensive platinum.

The surface morphology changes were observed experimentally in two different ways: firstly, a change of the metal surface under harsh conditions (high temperature) but under inert atmosphere. This phenomenon is called “thermal etching”. Secondly, the surface reconstruction has been observed in a reacting medium (e.g., ammonia combustion).

The mechanism of surface reconstruction of platinum during ammonia combustion is not completely understood until now. There exist several models, which will be briefly described in the following. Figure 4.7 shows the typical surface reconstruction of the platinum wire already after several hours at industrial reaction conditions.

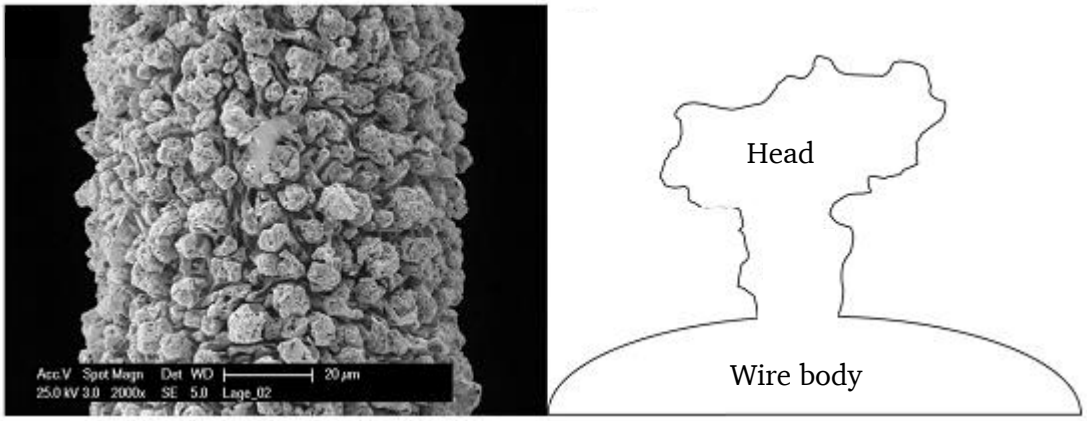

Figure 4.7: SEM image of a restructured wire during ammonia oxidation in the bench scale reactor from Heydt and schematic presentation of a single cauliflower excrescent [image Hey2018].

Philips et al. did research on platinum surface reconstruction during oxidation of ethylene with hydrogen. Platinum foil was used as a catalytic surface. A mechanism for cauliflower formation was postulated, which describes the appearance of C_2H_4 and O_2H radicals. The radicals react in the gas phase and form some clusters, which get to the catalyst surface and builds the excrescences [Wu1985, Wu1988, Hes1992, Dea1988].

McCabe et al. performed experiments where platinum wires were heated in the ammonia-air mixture. Scanning electron microscopy was used for the evaluation of etching on platinum surfaces. It has been found that the surface restructuring occurs in O_2-NH_3 mixture much more pronounced compared to pure oxygen or ammonia. McCabe et al. proposed a reconstruction mechanism, which includes surface reaction and the gas-phase boundary layer. Transport of volatile platinum oxide and surface diffusion appear to be responsible for the surface change. Furthermore, it has been observed that the growth of cauliflower structures starts at pits and defects on the surface [McC1973, McC1986].

Lyubovsky and Barelko have done interesting research, observing the formation of “metal wool” on a platinum surface. In their experimental set up, a part of the platinum surface was covered with gold and deactivated for the reaction. Two stages were observed. In the first stage, parallel facets were formed on the surface. In the second stage, the formation of microcrystals with perfect crystal faces was found. A vapor-liquid-solid mechanism was suggested for excrescences to grow. After the reaction starts, the rate of platinum sublimation from the surface increases. It leads to a much higher platinum concentration in the boundary layer compare to equilibrium concentration, and hence causes the platinum condensation on the surface directly out of the gas phase. Following parallel facets forms on the platinum surface. Then the facets become large enough; some liquid drops occur on the surface. The liquid drops absorb platinum vapor, that leads to a formation of cauliflower structures [Lyu1994].

Nilsen et al. investigated the catalyst surface reconstruction on industrial, electrical heated Pt/Rh wires. The appearance of Pt, PtO- and PtO_2 ions was approved in this work using mass spectroscopy. A mechanism for the cauliflower structures growth was postulated. The mechanism suggests that volatile PtO_2 is transported in the gas phase and is decomposed on areas with lower temperature. Furthermore, using WDX (Wavelength-dispersive X-ray spectroscopy) it was possible to show, that the concentration of Rh inbuilt excrescences is higher as in original wire. This effect can be explained by the lower vapor pressure of RhO_2 compare to PtO_2. PtO_2 can be easier transported away from the wire and out of the reactor, which leads to an irreversible platinum loss. Furthermore, it was reported that N_2O enhance the etching and the formation of cauliflower structures and water can inhibit this process [Nil2001].

Recently Nannevold et al. published his research about the reconstruction of Pt-Rh catalyst during ammonia oxidation. In this work, a bunch of analytical methods were used for the characterization of the catalyst surface, e.g., scanning electron microscopy, electron microprobe, X-ray powder diffraction, etc. It has been shown that the appearance and amount of reconstruction is a function of rhodium fraction in the alloy. The results of previous work from Nilsen has been confirmed: the concentration of Rh on excrescences is higher as in the wire body. A mechanism of platinum/rhodium transport has been suggested, which would characterize it as a vapor-transport reaction. A driving force for the transport is the local temperature gradients between hotspots and colder areas on the catalyst surface. After some time, equilibrium between the flux toward and outward the excrescent is established, and the shape of the cauliflower structure becomes unchanged.

Furthermore, a higher amount of rhodium in the catalyst has been shown as beneficial because Rh has better activity and selectivity toward NO compared to platinum [Han2005]. The distribution of the platinum and rhodium in the alloy is shown in Figure 4.8. The variation of activity and selectivity of the industrial campaign can be explained by the previously mentioned findings. At the start of the campaign, the selectivity toward NO rises because of increased concentration of Rh on the catalyst surface. After some time, the mechanical stability of the gauzes is influenced by restructuring processes, which leads to the drop of NO and rise of N_2O selectivity.

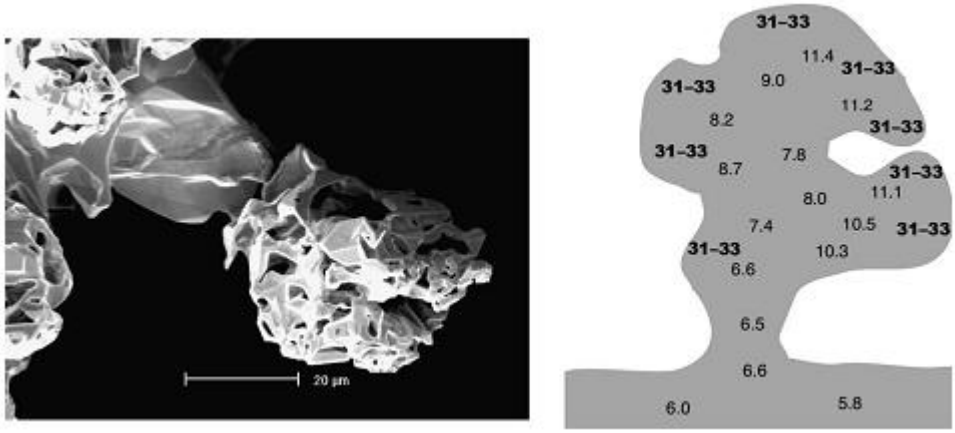

Figure 4.8: (left) cauliflower structure (right) scheme of cauliflower structure with a variation of Rh [wt. %] content in the alloy [Han2005].

More recently platinum wires after being in the ammonia burner for six months were examined by modern analyzing and visualizing techniques such as scanning electron microscopy (SEM), energy-dispersive X-ray spectroscopy (EDS) and micro X-ray computer tomography (μXCT). [Pur2013, Pur2015]. EDS makes it possible to analyze the content of Pt and Rh on the wire cross-section. By using the μXCT technique, the change in volume, surface area, and cross section shape can be investigated. It has been shown that the placement of the catalytic gauze has a strong impact on the reconstruction behavior. Surprisingly, it has been postulated that the cauliflower structures are less present in the first layer of catalyst. This cannot be approved by other studies and most industrial praxis. The common assumption is the stronger appearance of reconstruction processes on first gauzes in the industrial catalytic pack in the reactor. Nevertheless, a degradation process has been proposed. The process is schematically shown in the Figure 4.9. In the first stage, some small changes appear because of extreme conditions during the startup of the process. The next stage is the forming of

cauliflower excrescences. After that, the process comes to a kind of steady state condition, where some cauliflowers break out, and other new ones grow. The last section of the process is characterized by a strong concentration of Rh on the catalyst surface [Pur2016].

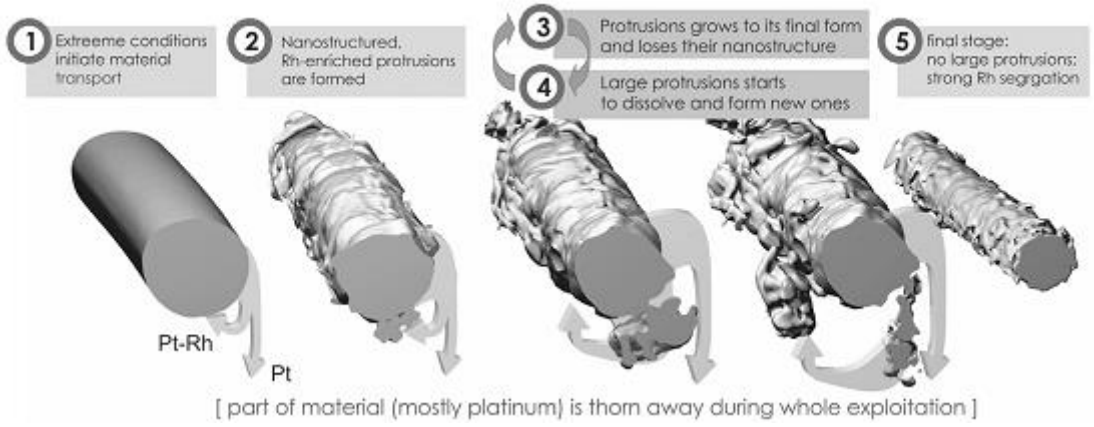

Figure 4.9: A mechanism of catalyst reconstruction and cauliflower growth during ammonia oxidation proposed by Pura [Pur2016, image Pur2016].

4.5. Experimental investigation of ammonia combustion on Pt gauzes

Ammonia combustion has a long history of experimental studies, beginning with Ostwald at the end of 19th century. Nonetheless, experiments under industrial conditions in a lab scale are challenging, and only a few works exist where industrial conditions and catalyst have been used for the investigations. A detailed description about experimental studies is given in works by Hyedt and Warner [Heydt2018, War2013]. The results of most of the studies cannot be compared and validated with each other because the conditions of the process, catalyst, analytics, and feed are in some cases very different. Therefore, published results are contrary to each other and sometimes contrary to industrial practice. It should be mentioned that this situation regarding experimental studies makes the validation of computational models very difficult. Despite the innumerable amount of experimental studies, there is still a need for more research in the field of ammonia oxidation under industrial conditions.

5. Methodology

5.1. Soft and Hardware

For the majority of CFD calculations and models, the commercial finite-volume element software Ansys Fluent was used. The model geometries were created in Ansys Workbench, and special software for processing tomography images called ScanIP has been used for models with restructured wire. Kinetics models and support calculations were done in software package MATLAB.

The following hardware was used for the calculations:

Machine 1:

Two processors Intel Xeon E5-2650 v4 with 12 cores

2.20 GHz

RAM 256 Gb

Microsoft Windows 10, 64 bit

Machine 2:

Intel Xeon Processor E5-2660 v3 with ten cores

2.60 GHz

RAM 128 Gb

Microsoft Windows 10, 64 bit

Machine 3:

Intel Xeon Processor E5-2660 v3 with ten cores

2.60 GHz

RAM 64 Gb

Linux, 64 bit

For more resource-consuming models, a university cluster computer (Lichtenberg cluster) was used, which consists of the following components:

8 Intel Xeon processors E7-8837 with eight core each

2.66 GHz

RAM 1028 Gb

5.2. Heat and mass transfer parameters

The precise determination of such quantities like viscosity, thermal conductivity and diffusion coefficients has a very large impact on the accurateness of computational models. Viscosity, thermal conductivity and diffusion coefficients for the reaction species in ammonia oxidation has been calculated based on Chapman Enskog theory and compared to the available experimental data. The polynomial functions, which has been used for CFD models, are given in the appendix.

6. Role of radiation in ammonia oxidation

Every object emits electromagnetic waves because of its temperature and absorbs thermal radiation from its surroundings. If the temperature of the object is hotter than the surroundings, it emits more radiation than it absorbs, and the object gets cool. At low temperatures, most of the radiation is in the infrared part of the spectrum and is invisible to the human eye. If the temperature is increased (in the case of ammonia oxidation when the catalyst temperature reaches over 900 °C), radiation increases and becomes visible (red glow).

The radiated power of a body is described by Stefan-Boltzmann law:

$$\dot{Q} = \varepsilon_s \cdot \sigma \cdot A \cdot T^4 \qquad \text{Eq. 6.1}$$

σ is the Stefan-Boltzmann constant, 5.67e-8 W m^{-2} K^{-4}, ε is the emissivity of the surface and A is the surface area. The emissivity is defined as the ratio of the actual heat flow to the heat flow of a black body (ε=1). The value of ε ranges from 0.05 for polished metal surfaces to more than 0.7 for ice, corroded iron and rubber.

In case of platinum/rhodium wires, which are used as catalyst in the ammonia oxidation process, the emissivity amounts 0.17 at 900 °C, according to the work from Bradley et al [Bra1997]. The work group from Bradley did measurements of emissivity of Pt/Rh wire at temperature in the range from 600-1450 °C in vacuum. The theoretical calculation based on the electrical resistance approves the experimental results. The Table 6.1 represents the results from Bradley [Bra1997].

Table 6.1: Theoretical and experimentally messured emissivity of platinum/rhodium wires.

Temp / °C	**600**	**700**	**800**	**900**	**1000**	**1100**	**1200**
ε, theoretical	0.1276	0.1444	0.1597	0.1723	0.1837	0.1937	0.2032
ε, experiment	0.1287	0.1450	0.1599	0.1723	0.1837	0.1937	0.2032

6.1. CFD Model

The CFD simulations has been carried out in the commercial software Ansys Fluent. The model contains 12 wires. The diameter of the single wire is 0.1 mm, and the axial length is 0.15 mm. The boundary conditions of the geometry are set as inlet (red), outlet (green), and symmetry (turquoise for fluid and orange for solid). The symmetry conditions are also valid for the radiation (DO-radiation model). The radiation reflects from the boundaries.

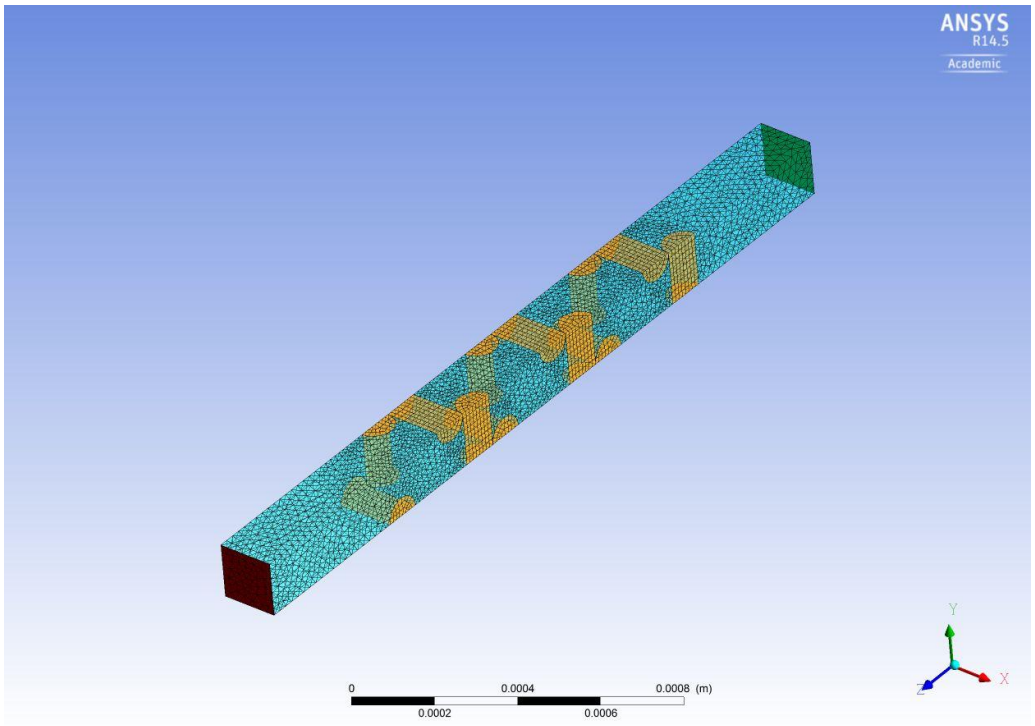

Figure 6.1: 3D geometry for the CFD simulation including 12 wires (orange).

The mesh contains 106210 faces (figure 6.1). For the calculation of chemical mechanism look-up tables are used, which imply the model C from Kraehnert. The inlet conditions are following:

$$x\_NH_3 = 0.0632$$

$$x\_O_2 = 0.2$$

$$T_{in} = 150\ °C$$

$$V_{in} = 0.75\ m/s$$

6.2. First estimation

In the first turn, we can make some simplified calculation to gain an overview of the heat transport and particular about radiative heat transport in the ammonia oxidation process. For this simplified estimation, we take into account only the first wire because the difference in the temperature of the first wire and the inlet gas temperature is the largest one. Hence the radiative heat flux on the first wire is the largest one too.

The heat transfer by convection can be express by the equations 6.2-6.4:

$$\dot{Q}_c = \alpha_w \cdot A \cdot (T_w - T_g) \qquad \text{Eq. 6.2}$$

$$A = \pi \cdot d_w \cdot L_w \qquad \text{Eq. 6.3}$$

$$\alpha_w = \frac{Nu \cdot \lambda}{d_w} \qquad \text{Eq. 6.4}$$

The Equation 6.1 is the convection heat from the single wire. In this estimation, only the first wire will be contemplated. A is the surface area of the wire, and α is heat transfer coefficient, Nu is the Nusselt number, d_w is the diameter of the wire and λ is the thermal conductivity.

The radiative heat can be estimated by the Equation 6.5 in analogy to Equation 6.4:

$$\dot{Q}_r = \varepsilon_{Pt/Rh} \cdot A \cdot \sigma \cdot (T_w^4 - T_g^4) \qquad \text{Eq. 6.5}$$

To calculate the heat by convection, it is necessary to know α and to calculate a Nusselt number is required. There is a semi-empirical equation, which can approximate the Nu [Jes2013]:

$$Nu = 0.3 + \frac{0.62 \cdot \mathrm{Re}^{0.5} \cdot \mathrm{Pr}^{0.333}}{\left[1 + \left(\frac{0.4}{\mathrm{Pr}}\right)^{0.666}\right]^{0.25}} \cdot \left[1 + \left(\frac{\mathrm{Re}}{282000}\right)^{0.625}\right]^{0.8} \qquad \text{Eq. 6.6}$$

Reynold number can be calculated by the equation 6.7:

$$\mathrm{Re} = \frac{\rho \cdot v_g \cdot d_w}{\eta} \qquad \text{Eq. 6.7}$$

Here is ρ the density of the reaction mixture, v is the gas velocity, d is wire diameter, and η is the molar viscosity.

The Equation 6.8 applies to the Prandtl number:

$$\mathrm{Pr} = \frac{\eta \cdot c_p}{\lambda} \qquad \text{Eq. 6.8}$$

η is the molar viscosity; c_p is the specific heat of the mixture and λ is the thermal conductivity.

The results of the calculation are presented in the Table 6.2:

Table 6.2: Values for the dimensionless number Pr, Re and Nu and heat transfer coefficient α.

Pr	**0.755**
Re	3.3
Nu	2.2
α	1529.7 [W/m^2]

According to the data from the table 6.2 and using equation 6.2 and 6.5, it is possible to calculate Q_c and Q_r for the first wire. The following chart shows that the radiative heat of the first wire contains only 1.7 % (9.091e-4 W) and heat produced by convection is 98.3 % (0.055 W), as it can be seen in the diagram (figure 6.2).

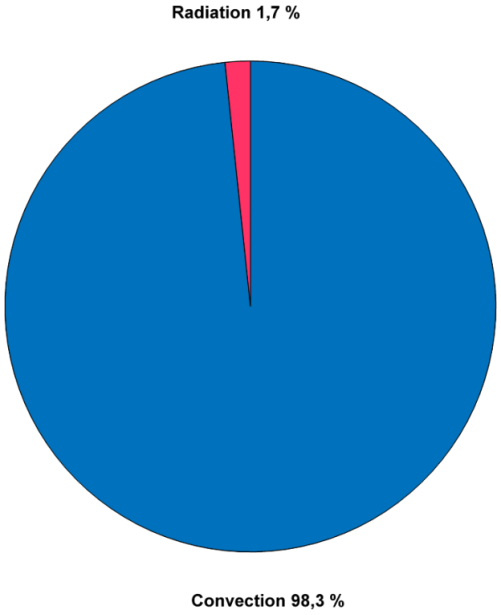

Figure 6.2: Fraction of heat from convection and radiation.

6.3. CFD Simulation

The discrete ordinate (DO) model is used to illustrate the radiation in the model. The radiation transport Equation 6.9 (RTE) of DO model is implemented in Fluent in the following form:

$$\nabla[I(r,\mathrm{s})\cdot\mathrm{s}]+(\mathrm{a}+\sigma_s)I(r,\mathrm{s})=\alpha\,\mathrm{n}^2\frac{\sigma T^4}{\pi}+\frac{\sigma}{4\pi}\int_0^{4\pi}I(r,s')\Phi(s\cdot s')d\Omega' \qquad \text{Eq. 6.9}$$

The RTE is solved for a finite number of discrete solid angles (or directions). The radiation intensity is calculated as a function of absorption, scattering, reflection, and emission. Numerical treatment of radiation heat transport is similar to the flow and energy equations. The DO model allows consideration of heat transfer caused by radiation between solid objects (wires in the catalytic gauze and reactor wall) as well as fluid domain.

The simulations are done in Ansys Fluent using previously described model. The calculation time amounts about 20 min without radiation and 1 hour with radiation. The Figure 6.3 presents the temperature distribution in the model:

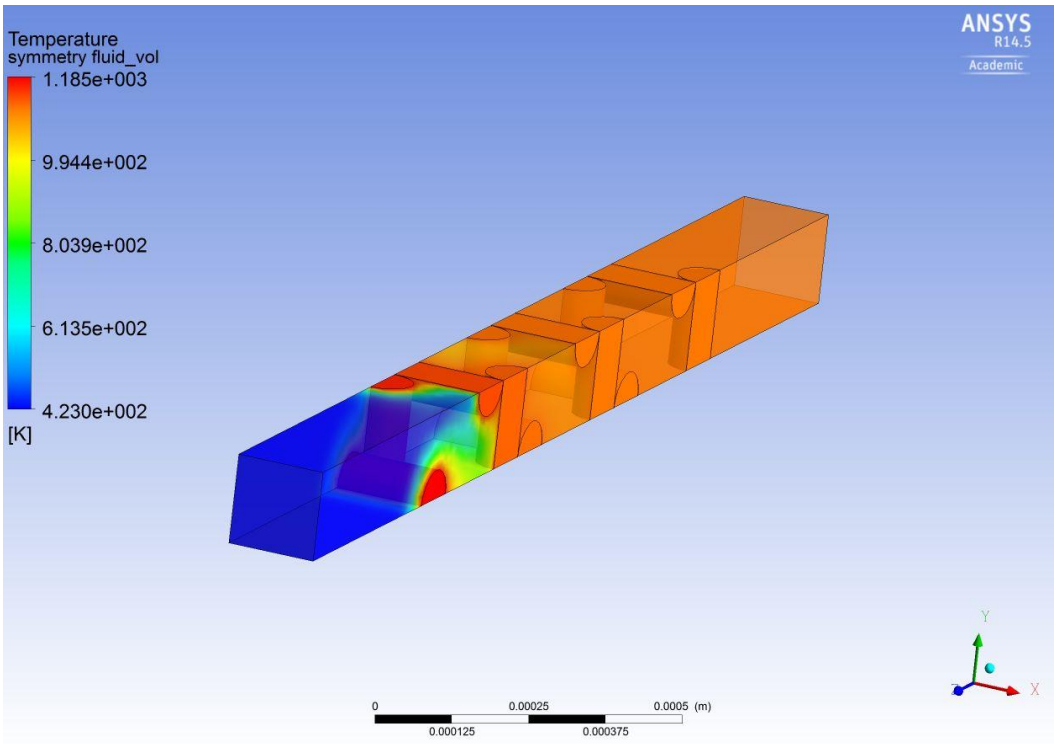

Figure 6.3: Temperature distribution in the CFD model after the converge calculation.

Furthermore the heat fluxes on the wires are shown in the Aigures 6.4:

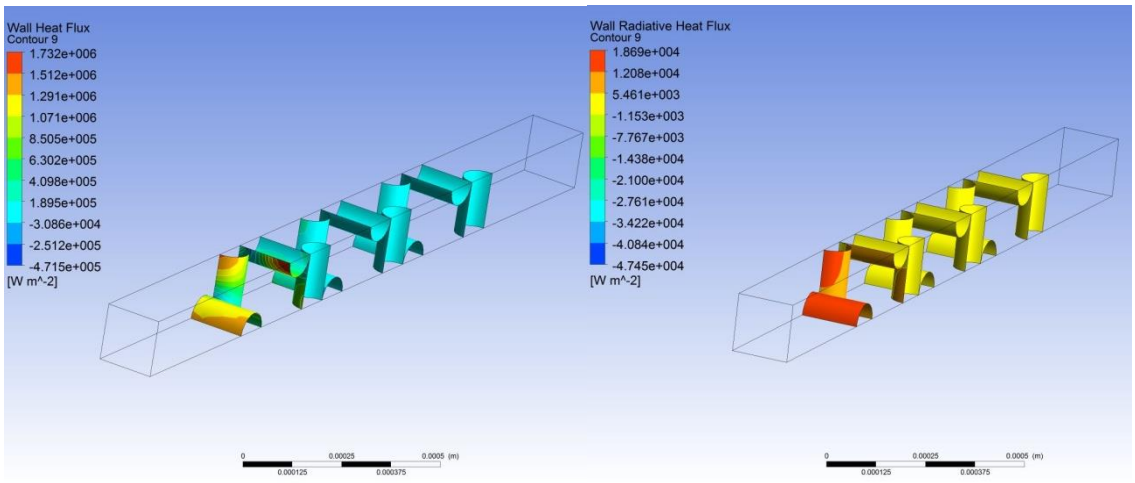

Figure 6.4: (left) The overall heat flux on the wires (right) radiative heat flux on the wires.

According to the presented images, it is perceptible that the first four wires have significant radiative heat flux and especially the first wire. The reason for that is the temperature difference between the wire and the gas. In the case of the first wire, the discrepancy is highest because the radiative heat flux from this wire is the largest one. Nonetheless, the percentage value of the radiative heat flux compared to convection is only 1.5 %. This calculation conforms to the previous estimation done by the aid of dimensionless numbers.

The CFD simulation and simplified numerical estimation have shown that the radiative heat flux is more or less negligible compared to convection heat flux. But the most important aspect in the ammonia oxidation is the wire temperature and the selectivity to NO, N_2O, and N_2, which are highly dependent on it. The Figure 6.5 shows the temperature of wires from simulations, with and without radiation included.

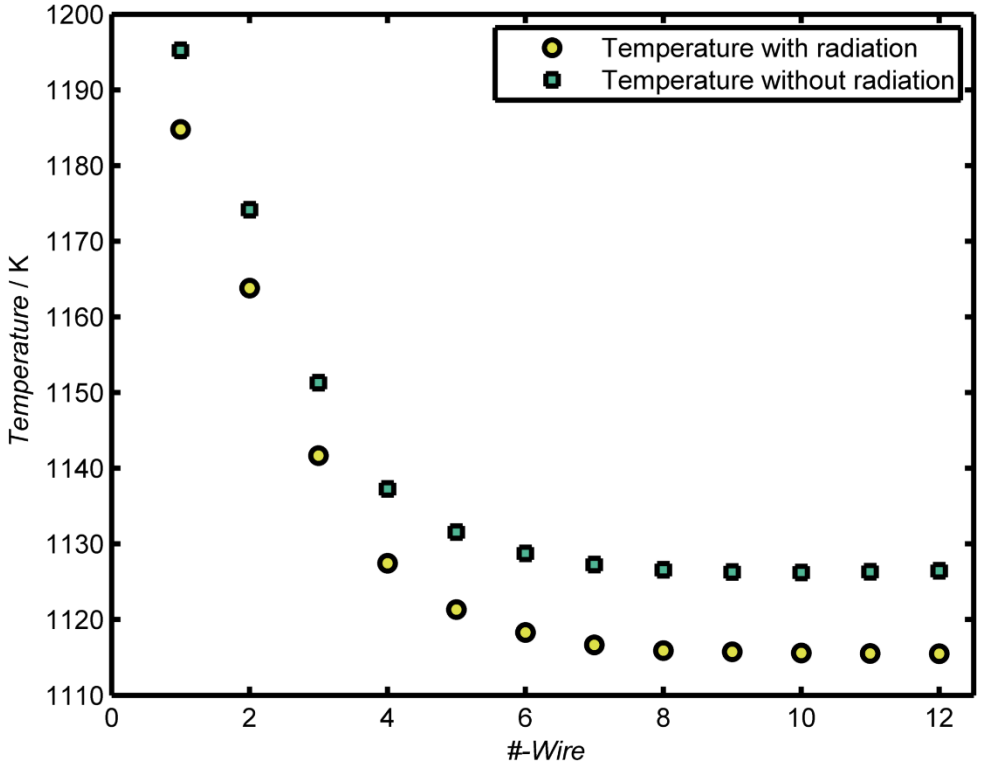

Figure 6.5: Temperature of the wires form simulations including with radiation and without radiation.

The temperature decreases with the pitch from the inlet. The wire temperature from simulations including radiation is about 10-12 K low, as the temperature from simulation without radiation. It is noticeable that the temperature differs even by last wires. This observation can be explained by adiabatic temperature. The higher temperature of the first wires influences (increases) the adiabatic temperature and the last wires adopt the adiabatic temperature, so the difference form 10-12 K is observable by all wires.

In the Figure 6.6, there is a comparison between selectivity, which has been calculated with the model including radiation and the model without radiation.

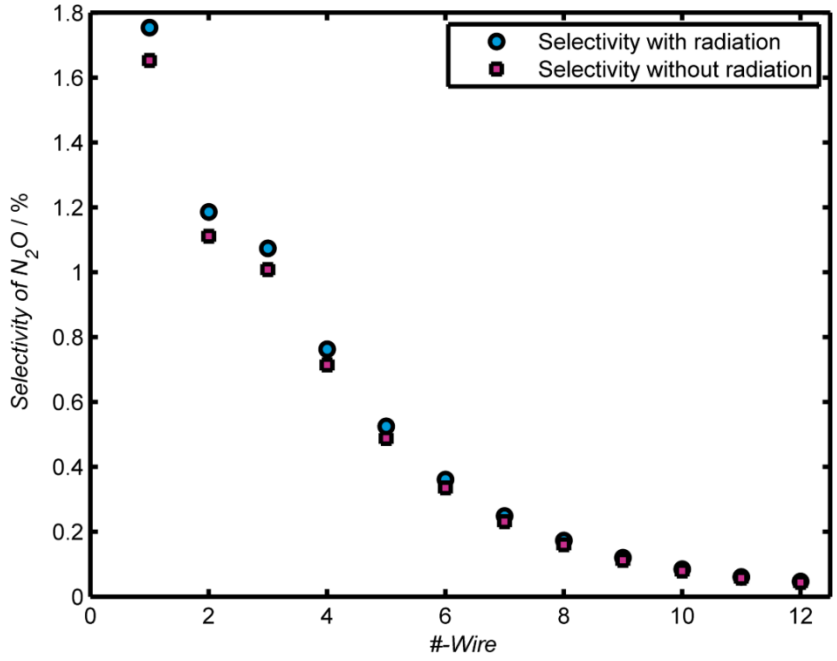

Figure 6.6: Average differential selectivity on the catalytic wire, calculated from the model with and without radiation.

The difference in the selectivity on the first wire is largest and amounts to 0.1 % (with radiation 1.754 and without radiation 1.653). It is noticeable that the selectivity of N_2O from the model with radiation is higher and the temperature of the wire is lower than from the model without radiation. This behavior can ascribe to characteristics of the used mechanisms for the ammonia oxidation (Model C form Krähnert).

In summary, it can be said that the radiation has only a negligible influence on the ammonia oxidation process, in heat fluxes as well as in selectivity. That can be shown by estimation using the dimensionless numbers and by complicated CFD simulations. Therefore, it is significant by CFD simulations of ammonia oxidation to illustrate the N_2O Selectivity with high accuracy ,and discrepancy from 0.1-0.2 % in the Selectivity can be relevant. But the bad calculation time – performance ratio (triple calculations time VS. 0.1 % improvement) should be taken into account. The models without radiation save calculation time and can describe the process with good approximation. For that reason, the radiation calculation can be used for fine-tuning from already existing CFD models.

7. Wire orientation in the flow domain

Two different types of model were developed. The first model includes only one wire and the second model contains four parallel wires. The wires are rotated 35, 45, 55 and 70 degrees around the middle point of the upper face of the geometry (Fig. 7.1). By rotating the domain like in Figure 7.1, the “active” surface of a single wire increases, which causes the elevation of the conversion. The conversion of the models with just one wire is between 40-80 %, and the change of nitrous oxide selectivity can’t be decisively related to the attacking angle or the conversion’s change. On account of this, models are required, which produce nearly full conversion. It was realized through increasing the wire’s number in the model. The conversion in the models with four wires is in the range of 95-97 % and the difference between models is very small. Therefore, the conversion’s influence on the N_2O selectivity can be eliminated.

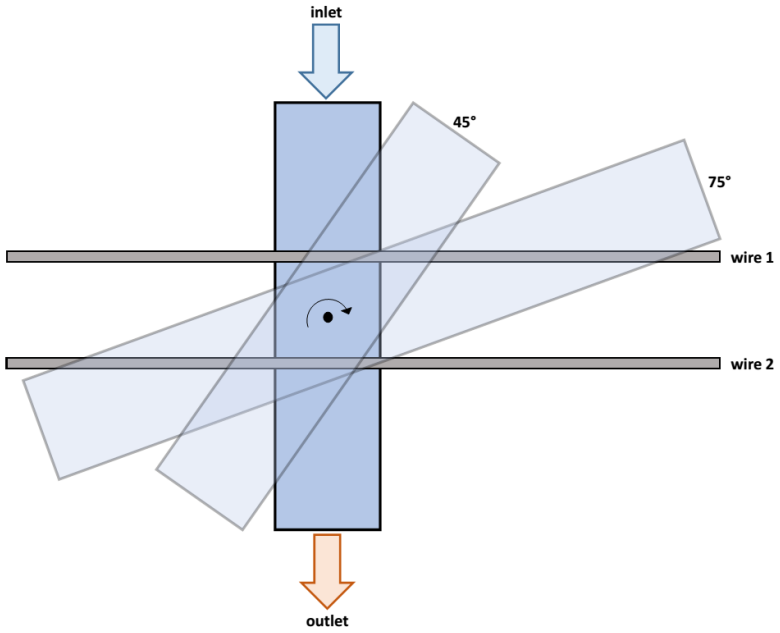

Figure 7.1: Schematic representation of the simulated model with a rotated domain.

To compare the models with different attack angels, it is important to recognize that the shape of the wire and the pitch from wire to wire changes with the rotation angel. This change has a significant effect on the dynamic of the flow, which influences the conversion and selectivity. The Figure 7.2 shows the change of the wire surface, which is sliced by the domain edge, and the position of the wire in the domain.

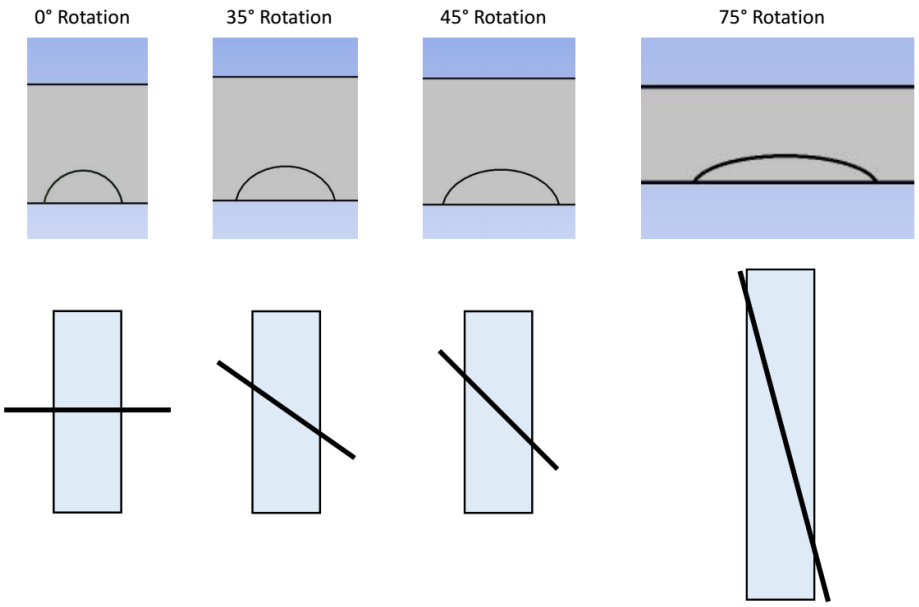

Figure 7.2 *(top):* The shape of the wire's surface, which is sliced by domain edge. *(bottom):* The position of the wire in the domain.

To get more convenient results, the models are created in three dimensions. The boundary conditions from wires and fluid on the upper and lower geometry's faces (Fig. 7.3 red) are set as symmetry. The left and right faces (Fig. 7.3 green) are set as periodic.

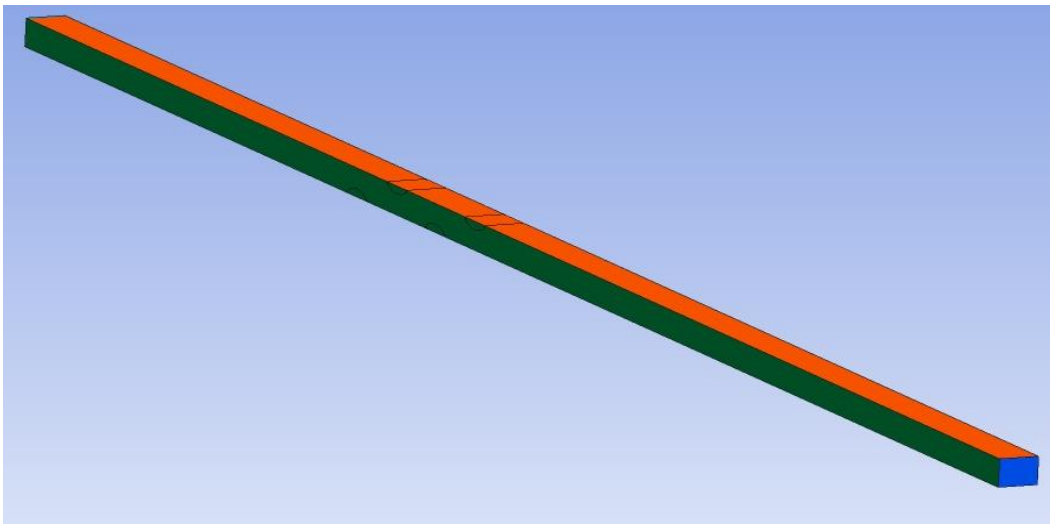

Figure 7.3: The boundary conditions of the four wire model. The wires are 35° rotated.

The oblique wires redirect the flow distribution. Hence, it is significant to reproduce the redirected flow along the rotated wires. That can be realized by use of the periodic boundary condition. The left and right faces should contain the same number of mesh elements. Then such pairs of faces act as a tunnel. Each outgoing term (mass or energy) of a face is equal to the incoming term of the corresponding face on the model's other side. In case of oblique wire

simulation the periodic boundary condition is needed because of the flow pattern which can occur due to the influence of the oblique wires on the flow direction.

The inlet conditions for both models are the following:

- $x\_NH_3 = 0.0632$
- $x\_O_2 = 0.2$
- $v_{in} = 0.75$ m/s
- $T_{in} = 150$ °C

The operating pressure is 5 bar. Look up tables were used to implement the chemistry of the ammonia oxidation in the models. The look-up tables include the mechanism from Krähnert (Model C).

7.1. Variation of Rotational Angle

The figure 7.4 shows the selectivity and the conversion depend on the rotation angle of the wire. It is recognizable that the selectivity to nitrous oxide descends and the conversion arises by increasing the rotation angle of the wire.

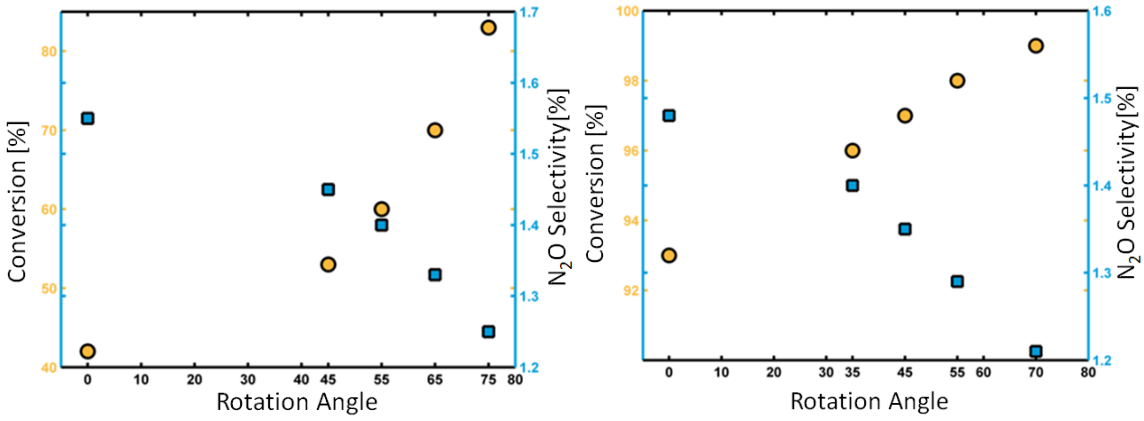

Figure 7.4: Selectivity and Conversion of single wire models *(left)* and 4-wire models *(right)* with different rotation angles.

In the case of increasing conversion, the explanation is simple. The wire rotation leads to the extension of the catalytic surface (the dimensions of the considered domain remain the same), where the reaction can take place. The difference in conversions between models was eliminated by including several wires in the model. But the fact remains, the conversion of the first wire is the largest one in the model with the biggest rotation angels. Because both

models (single wire and four wires) show the same trends, the following discussion will be carried out on the model, which includes four wires.

Computation fluid dynamics simulations give the possibility to the very detailed investigation of temperature, velocity, composition and other properties of the fluid in the wire-region. By reasonable comparison of the results, it is possible to acquire new knowledge about interdependences of factors, which can reduce the production of nitrous oxide.

The selectivity to N_2O on the wires is shown in the figure 7.5. The results are predictable. Production of nitrous oxide on the first wire is the largest and drops from wire to wire. This finding is explainable with the fact that the highest amount of ammonia is burned on the first wire. The distribution of the NH_3 concentration in the model confirms this.

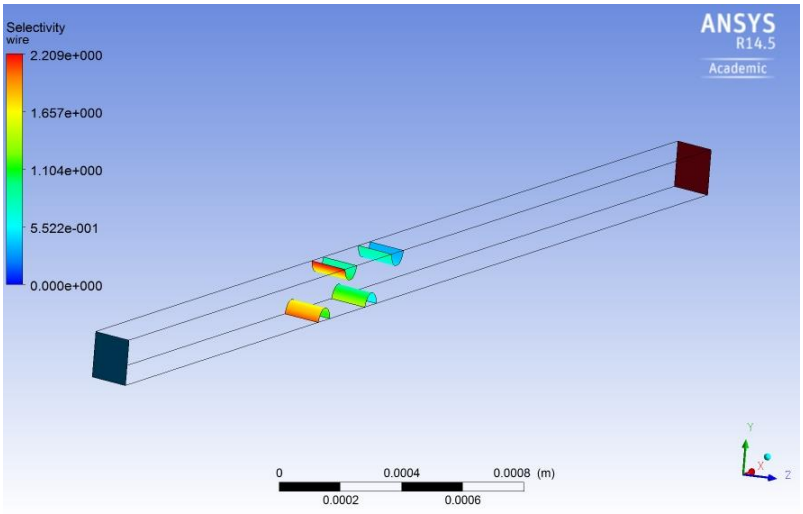

Figure 7.5: Selectivity distribution of the wires. The inlet (blue) and the outlet (red) are marked on the picture.

The next interesting point is the distribution of the differential selectivity along the wires and their comparison. Figure 7.7 presents a comparison of differential selectivity along the wires by different rotation angels. On graphs, x-aches are coordinates in the X-dimension of the model. The selectivity values were taken from the lines, which cross the wire as in the figure 7.6. Due to the wire rotation, the length of the lines is different. For the better view of results, coordinates were normalized. So 1 is the first point of the front side of the wire.

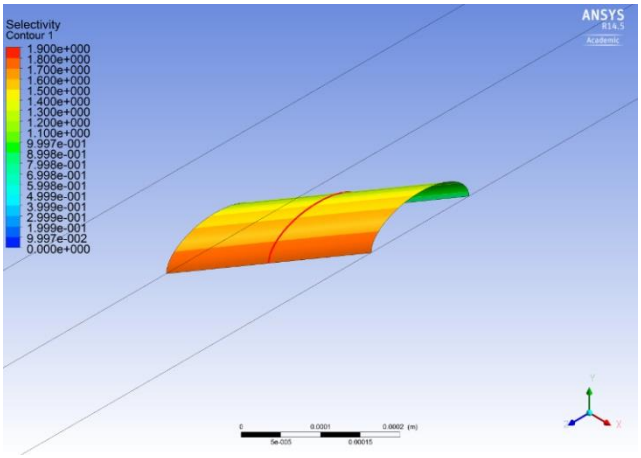

Figure 7.6: The differential selectivity is taken from the red line, which crosses the wire in the X-direction.

It is remarkable that the selectivity on the front side of the first wire is almost identical by all models. Hence it can be concluded, the conditions on the front side of all wires, independent of the rotation, are more or less equal. This result is logical because the inlet conditions are for all models the same, and the flow isn't perturbed before it makes contact with the first wire.

The distribution of the selectivity along the single wire is understandable; the amount of ammonia is low in the rear part of the wire because the conversion and selectivity to nitrous oxide decrease there.

The next significant observation is the difference in the selectivity of the following wires. Generally, the selectivity drops from wire to wire because of the same reason it drops along a single wire. Furthermore, there exist differences between models with a varied rotation angle of wires. The selectivity to N_2O decreases with a rising of rotation angle, so the selectivity of 35° rotated wires is greatest, and 70° rotated wires has the lowest laughing gas selectivity.

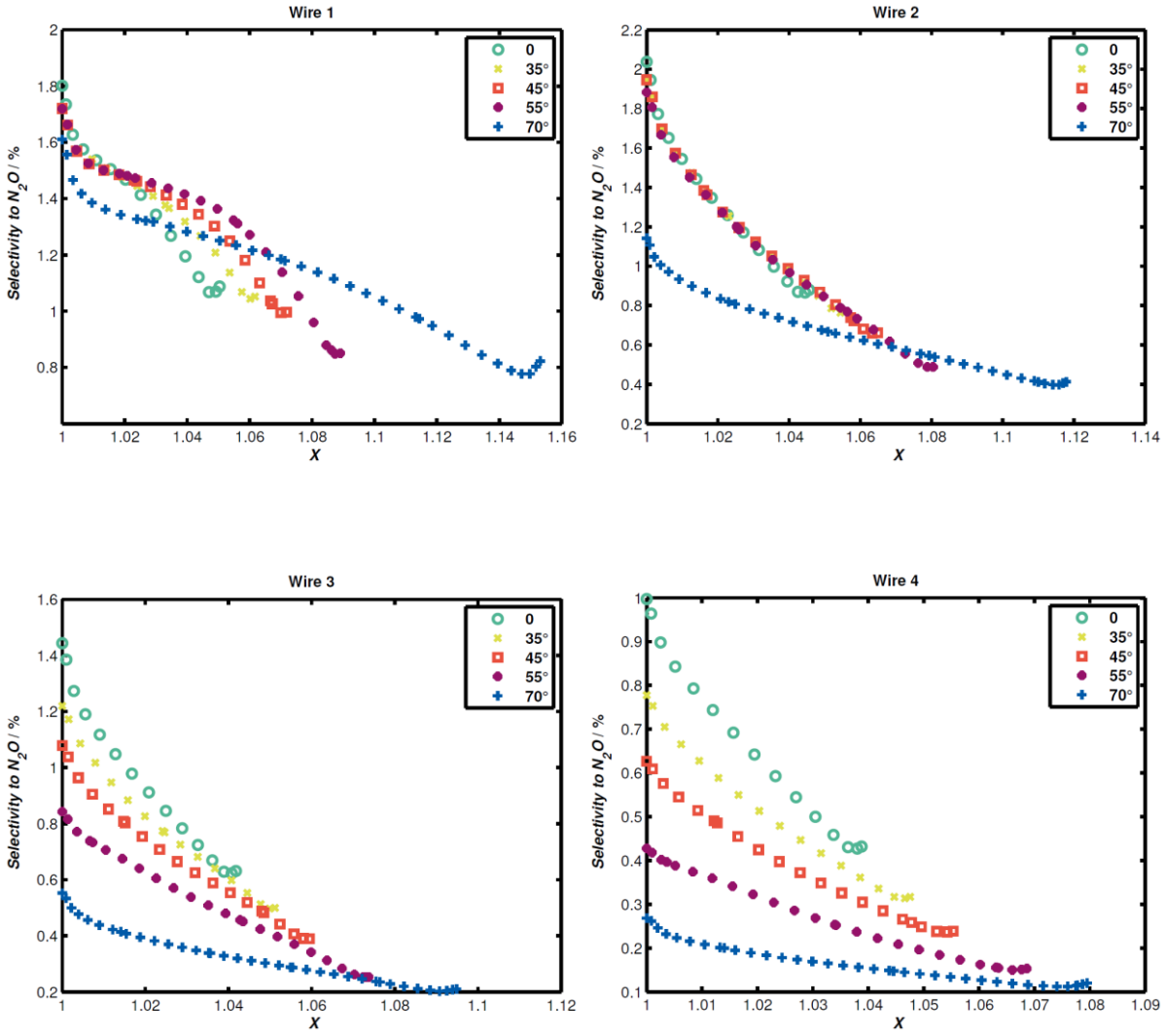

Figure 7.7: The differential selectivity along wires in models with different rotation angles of wires.

A large number of factors can influence the selectivity and conversion of ammonia oxidation on a platinum wire. A change of any condition leads to changing of other conditions and results. In the corresponding case, the different flow distribution, due to different rotation angles of catalytic wires, affects the temperature, conversion, and selectivity.

When regarding flow velocity profiles of models with different rotation angles of wires, it becomes clear that the velocity distribution is more homogeneous in the case with 70° rotated wires. In this case, the velocity between the wires is very close to the inlet velocity. The large rotation angle (toward the flow direction) of wires leads to a smooth velocity field, without high accelerated zones (high velocities), compared to the model, where the wires are not rotated (Fig. 7.8).

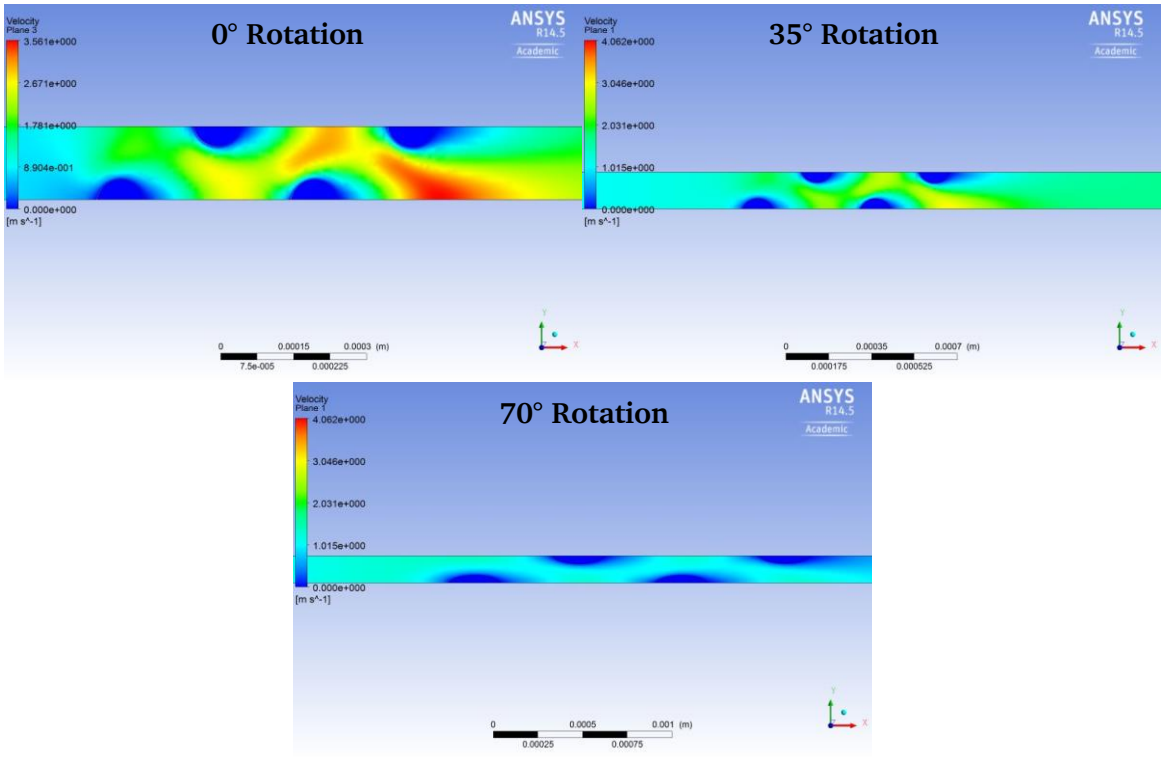

Figure 7.8: Velocity profiles of models with different wire rotation angles.

Furthermore, the flow patterns are influenced because of the oblique position of the wires to the flow direction. The flow becomes more parallel to the wires, as it can be seen in the figure 7.9, which leads to a decrease in N_2O selectivity as well.

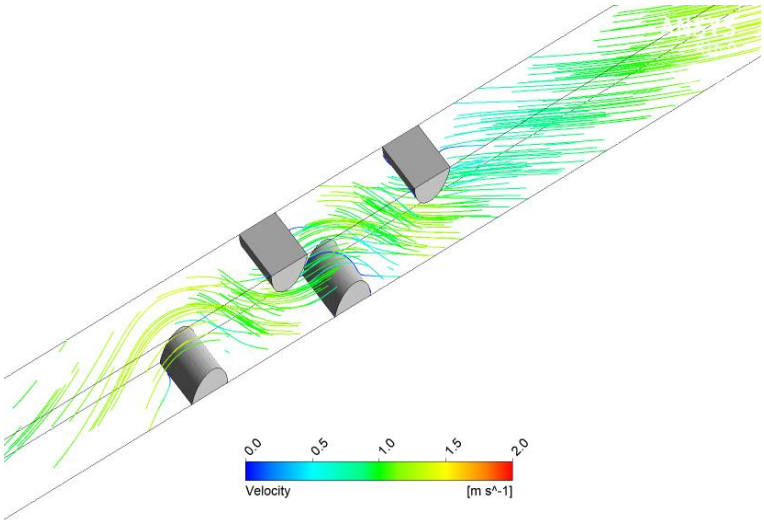

Figure 7.9: Flow stream lines in the computation of the model with 70 degree rotated wires.

It can be assumed, that the acceleration of velocity in the model leads to the decreasing of the nitrous oxide selectivity. One of the ways to influence the velocity in the desired region is to

optimize the gauze geometry. By the creation of gauzes, it can be suggested to increase the number of elements which are parallel or almost parallel to the flow direction. Such wire elements do not perturb the flow distribution and do not increase the velocity. Due to this aspect, the production of nitrous oxide may be reduced.

A certain predication for factors, which decrease the N_2O selectivity, is very challenging, due to the complex kinetic mechanism of ammonia oxidation and flow distribution as well as interdependences of many of other factors like pressure, velocity, temperature, composition, etc. Nonetheless, CFD simulations can throw new light on the tendencies, which can be used by the development of new gauze geometries.

8.1.1. State of the art

At the beginning of 1990s, Johnson Matthey published an experimental work where it was found that gauzes manufactured with knitted technology were superior to old woven ones. The catalytic performances, as well as manufacturing criteria, were improved [Hor1991, Hor1993]. The precious metal inventory in case of woven gauzes was significantly reduced as well as the production time. The knitting machine required only 5 kg of precious metal wire compared to 50-100 kg for the weaving loom [Hor1993]. Since then, the production of almost all gauzes manufactured has been switched to knitted gauzes. The amount of knitted gauzes in ammonia oxidation burners is reported to be over 90 % [Per2003]. The different possible schemes for knitting allowed the production of very different geometries (figure 8.1). Recently, pack tailoring has been offered to the nitric acid manufacturer as an additional service by catalyst manufactures. The catalyst gauze pack is then specially designed for the ammonia reactor that the customer owns and is adapted for the customer needs. But until now, there have been no academic studies which would explain or rationalize the design of knitted gauzes.

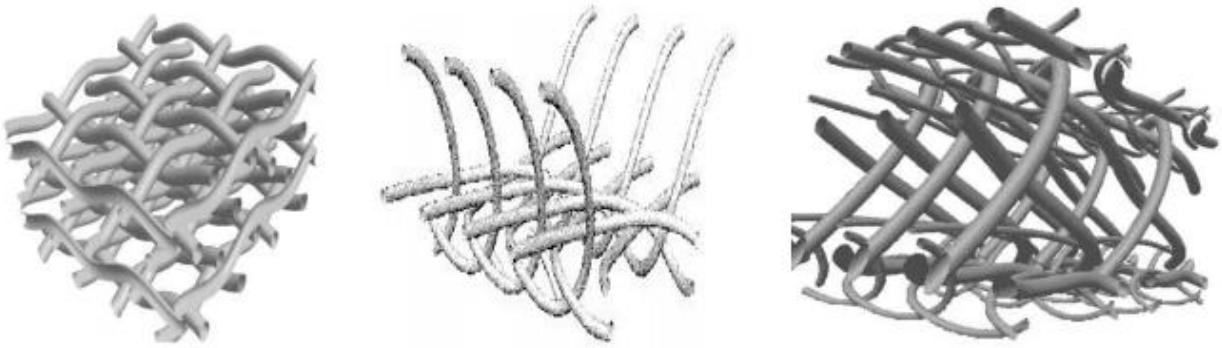

Figure 8.1: Examples of knitted (left) and woven Platinit (middle) and Multinit (right) gauzes [Umi2006].

Furthermore, the production of nitrous oxide (N_2O) during the nitric acid process becomes a crucial discussion topic in the last years. N_2O is a very strong greenhouse gas, its green house potential is almost 300 times stronger as that of carbon dioxide [Per2003]. Because the gauze geometry can beneficially influence the catalyst performance, the optimization of the geometry design becomes an important way to reduce N_2O selectivity and make the nitric acid process more environmentally friendly.

Since the reaction is known to be strongly heat- and mass transfer controlled, simulations which combine the surface chemistry, flow, diffusion and heat conduction are the key to the better understanding of the process and developing of new catalyst. In the last three decades, the advent of the fast computers combined with the development of accurate numerical algorithms for solving physical and chemical problems give us a possibility to perform computational fluid dynamics (CFD) simulations on complex industrial catalytic gauzes with included detailed surface kinetics.

First studies have been done by Nien et. al., in this work a CFD model for an ammonia oxidation gauze type reactor was developed. The model included a detailed kinetics, which was based on the Krähnert reaction mechanism [Kra2008]. Simulations have been done for some simplified two and three-dimensional geometries. It was shown that the selectivity of the desired product (NO) and undesired byproducts (N_2O and N_2) depend not only on the reaction condition, such as temperature and pressure but are also strongly influenced by the geometry of the catalytic wire. The differential selectivity on the catalyst surface varies around the perimeter of each wire and also from wire to wire (Figure 8.2). The parametric studies including the wide range of variations of inlet velocity, wire diameter and wire distance to each other have been done in this work [Nie2013].

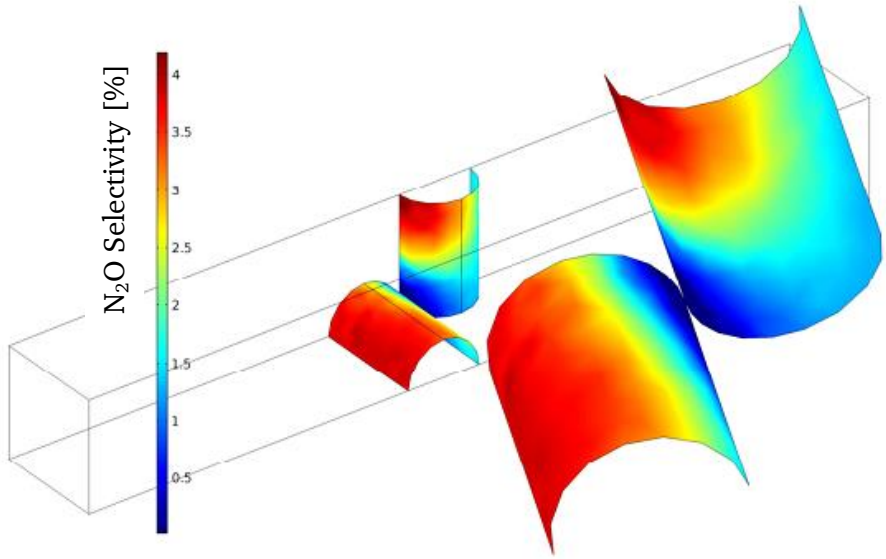

Figure 8.2: Color contours are representing the selectivity of N_2O [%] on the surface of catalytic wires.

The main aim of this work was the investigation of the influence of catalyst geometric parameters such as the wire diameter and the distance between two wires in the catalytic

package on the conversion and selectivity. The explanation of the selectivity variation phenomena (variation of the N_2O selectivity on the surface of the same catalytic wire) was not addressed in this study.

Klingenberger showed in his work the importance of the inclusion of mass transfer in the ammonia oxidation models. The relationship between the mass transfer coefficient of single species and the production rates of them has been explained in his research using CFD modeling and degree of rate control approach [Kli2016]. To illustrate the influence of mass transfer, a simulation without mass transfer limitation has been performed. The CFD simulations in Klingenberg research were performed only with simplified two-dimensional geometries, which can completely satisfy the aim of validation and optimization of the kinetic mechanism from literature but can be hardly used for the comparison with industrial used catalysts.

The results (Figure 8.3) of such simulation show an entirely different selectivity ration of the reaction products (NO, N_2 and N_2O). It is interesting to highlight that in both cases (with and without mass transfer limitation) the ammonia conversion reaches almost 99 %, but in the case with included mass transfer it happens ten times slower [Kli2016].

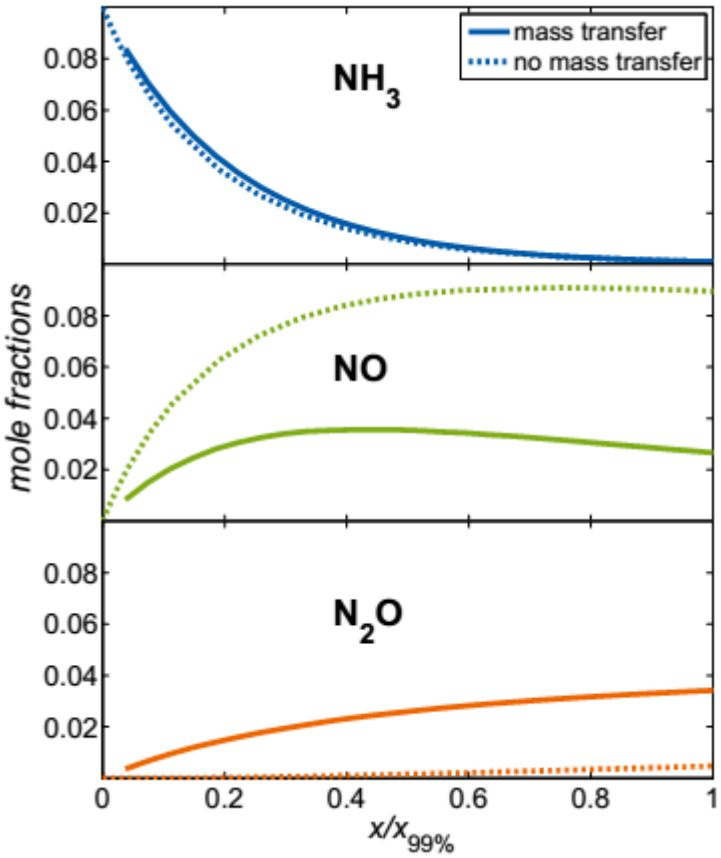

Figure 8.3: Axial mole fraction profiles from simulations with and without the inclusion of mass transfer limitation. The x-axis is the normalized position coordinates [Kli2016].

Furthermore, Klingenberger extended the calculation of the degree of rate control [Cam1994] for the mass transfer coefficients as well and has shown the quantified influence of mass transfer coefficients on species formation rates. The diffusion of ammonia toward the catalyst surface is the rate determining step for the NO formation. Faster transport of NO promotes its formation as well. Slower transport of oxygen increases the production of byproducts (N_2O and N_2). Faster transport of N_2O increases its formation. The following Figure 8.4 illustrates the degree of rate control of mass transfer and elementary reaction steps. The Novell-Leruth was implemented in simulations performed by Klingenberger [Kli2016].

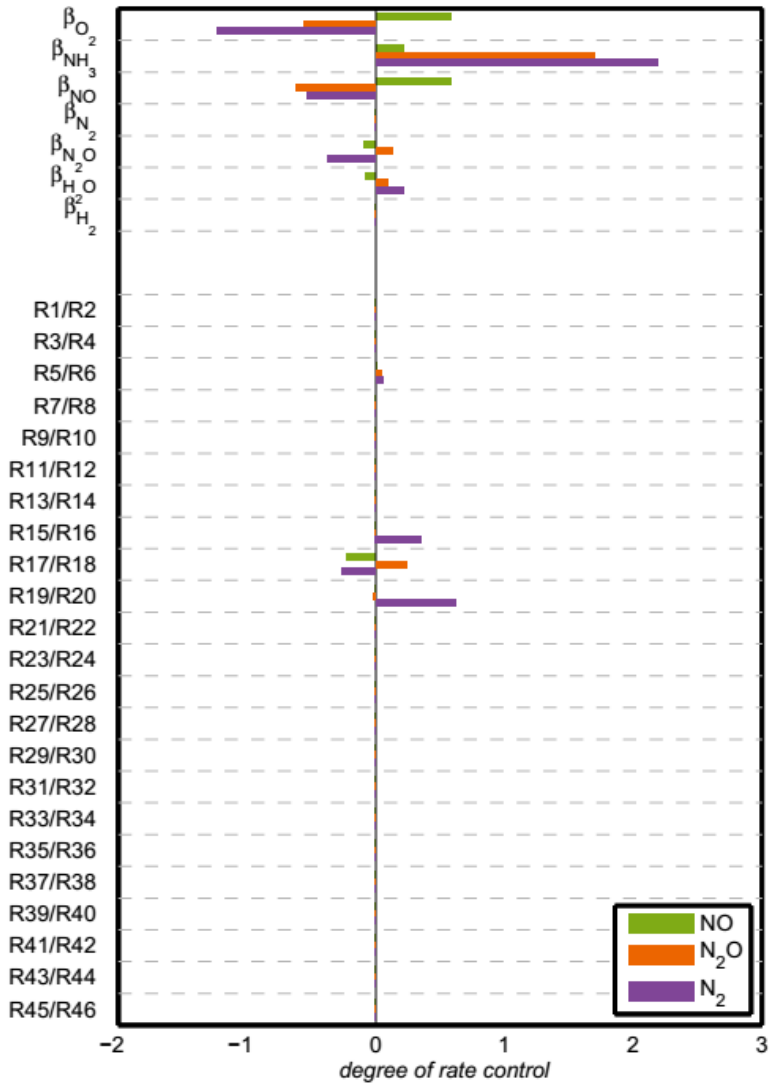

Figure 8.4: Degrees of rate control of mass transfer and reaction steps for the products. Novell-Leruth kinetics was used in this case [Kli2016].

Because mass transfer coefficients (β) are the function of flow pattern and also with an overview of the results of research from Nien and Klingenberger, a conclusion can be drawn that the product selectivity is a function of the local mass transfer coefficient. This observation provides us ground for further development of complex CFD models, which can describe the industrial catalyst geometries. Furthermore, the comparison of different industrial geometries can provide a hint for the explanation for the superior performance of some geometry over others.

8.1.2. Validation against pilot plant experiments

In this work, complex industrial gauze geometries were used for CFD simulations. The numerical discretization of the computational domain reached ten millions cells in some cases. Some simulations were performed on the Lichtenberg cluster computer due to the large size of the models.

Such complex models are prone to different kinds of errors. Considering that fact, a validation of a CFD model with some practical test is very important. Few of the industrial catalytic gauzes were tested on pilot plant, and results for these geometries were provided by Umicore for the validation of CFD models. The following case is an example for the comparison of catalyst performance, which was shown during the experiment in the pilot plant and calculated in CFD simulation.

The geometry type can be seen in the following Figure 8.5. A representative part of the whole gauze was chosen due to symmetry pattern. This model was created by scanning real catalytic gauze. The scan has been transferred into a suitable format for CFD modeling in the software package Ansys Fluent.

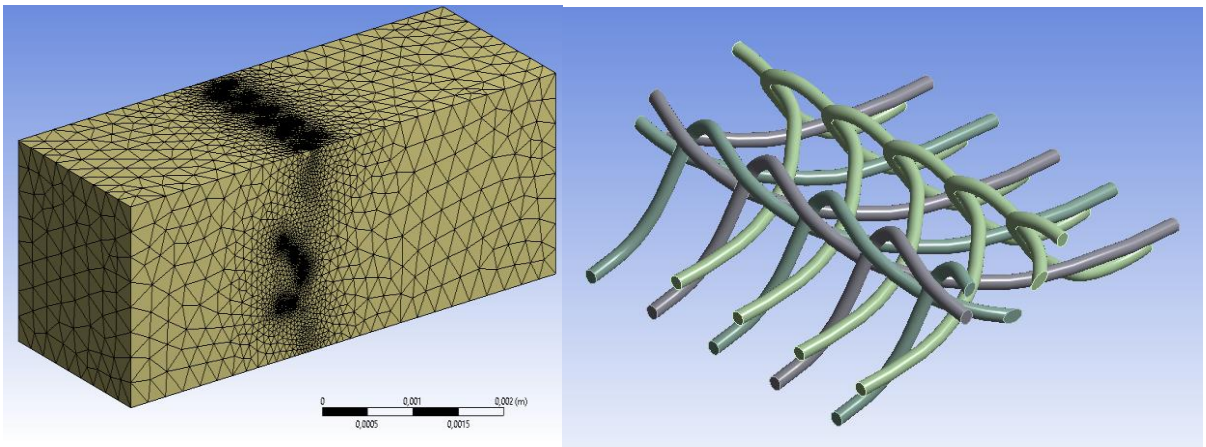

Figure 8.5 (left) discretized computational domain for one layer catalyst layer. (Right) the catalytic gauze geometry which has been tested in the pilot plant.

The number of single gauzes was 6 in a row to achieve the almost complete conversion of ammonia similar to the experiment in the pilot plant.

A variation of the inlet velocity has been done in the experiment and the simulation as well. Three values were chosen for variation: 0.5, 0.75 and 1 m/s. All that gas velocities are representative in the industrial practice for ammonia burner.

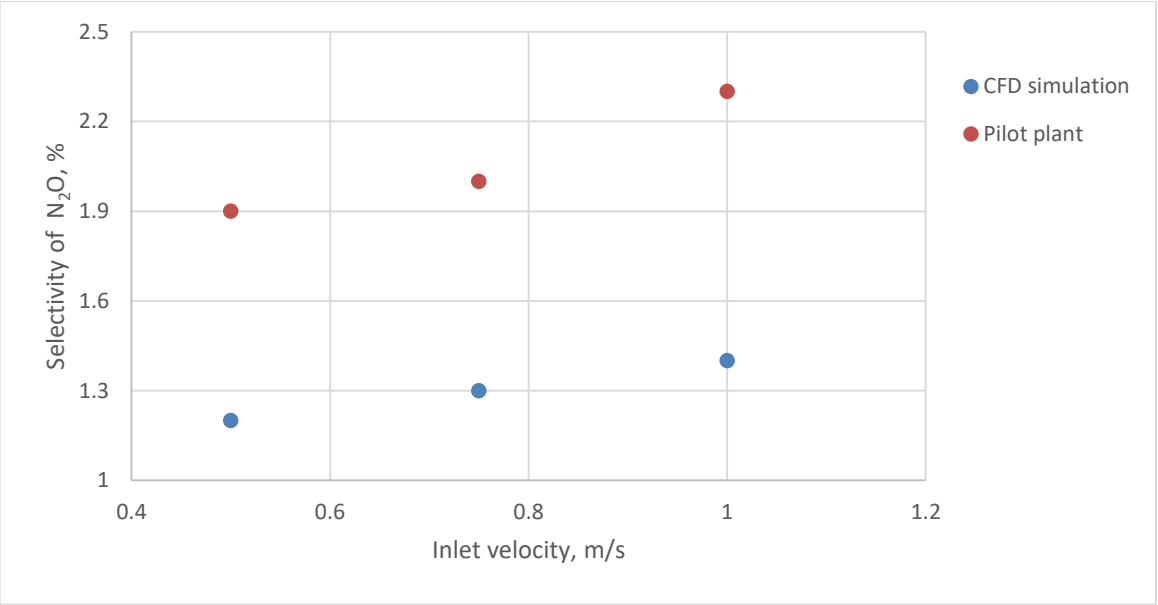

Figure 8.6: Dependency of N_2O selectivity on linear velocity in the domain during experiments in the pilot plant and results from the CFD simulation.

Figure 8.6 shows the experimental and simulation results. Selectivity for nitrous oxide was chosen as a benchmark on purpose because this quantity is the most sensitive one. It can be seen that the absolute discrepancy for N_2O selectivity between the model and pilot plant is about 30 %. This deviation can be explained by the fact that the real experimental parameter and conditions cannot be exactly repeated by the computational model. Such factors as catalyst heat loss by radiation and convection toward cold reactor wall, and a not perfectly parallel arrangement of the single gauzes in the catalyst pack, etc. cannot be taken into account in the computational model.

Nevertheless 30 % deviation is a very good result for such a kind of comparison.

Furthermore, the increase of N_2O selectivity with the inlet velocity can be captured by the simulation very well. More generally, the simulation results (conversion and product selectivity) are in good agreement with industrial practice as well. Moreover, the wire and gas temperature can be reproduced by the simulation very well compared to industrial and pilot plant reactors.

Summarizing the validation of a chosen catalyst CFD model with pilot plant experiments and industrial practice, a conclusion can be drawn that the CFD models provide realistic results and can describe the general trends of ammonia combustion on the industrial catalyst. Nevertheless, a more detailed validation including more comparable laboratory and pilot plant experiments is desirable.

8.1.3. Influence of Temperature, Pressure and Linear Velocity

For further investigation of the influence of temperature, pressure and velocity on the catalytic performance of the ammonia oxidation reaction, the industrially used gauze geometry has been chosen. This type of gauze is distributed by Umicore and has a tradename “Platinit”. The computational domain is presented in the following Figure 8.7. The domain consists of approximately six millions polyhedral elements. The reaction conditions are the same as in the case above.

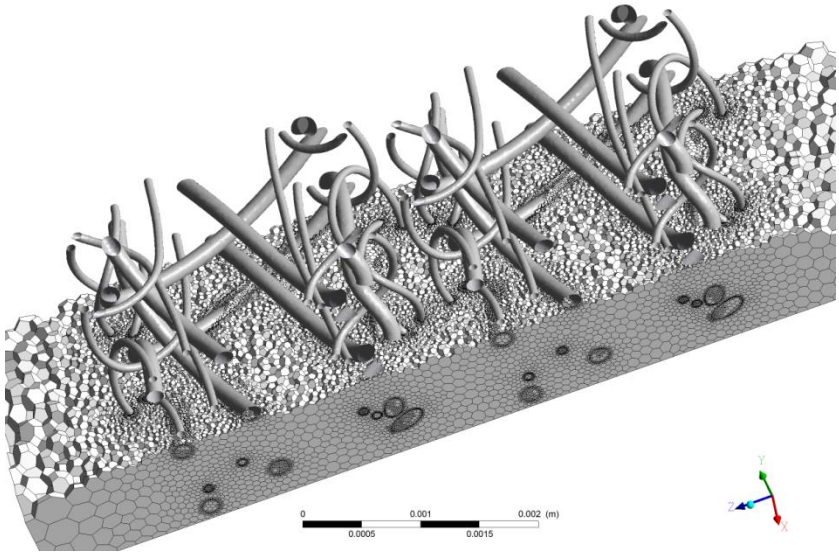

Figure 8.7: Discretized computational domain of "Platinit" catalytic gauze.

Furthermore, the temperature is slightly decreasing along the catalyst pack. The first catalytic layer has the highest temperature due to a very high ammonia conversion rate in that area. The temperature of the rear catalyst layers decreases until it reaches the adiabatic temperature. Those phenomena were already found and calculated in the work of Klingenberger [Kli2016] and a textbook of Wasserscheid and Jess [Jes2013]. In this research, the described temperature phenomena have also been found. The following Table 8.1 shows

the surface wire temperature in the knitted gauze model. After the wire number 5, the temperature becomes constant.

Table 8.1: Surface temperature of the catalytic wires. The number 1 is the first wire of the domain in the flow direction.

Wire #	**1**	**2**	**3**	**4**	**5**
T_{wire} / K	1165	1144	1135	1129	1127

A similar observation can be made from the following figures 8.8 and 8.9. The temperature profile of the reaction mixture is shown in the computational domain. It can be seen that the hottest area is around the first catalytic wires. The temperature of the gas phase increases and reaches the temperature of the mixture in the last third of the domain. The temperature of the mixture and catalyst is the same in this region, and it is called adiabatic temperature. The adiabatic temperature rise can be calculated according to Eq. 8.1:

$$\Delta T_{ad} = \frac{c_{NH3}(-\Delta_R H)}{c_p\ \rho_{mol}} = \gamma_{NH3,g}\frac{(-\Delta_R H)}{c_p} \qquad \text{Eq. 8.1}$$

where c_p is the heat capacity of the mixture, $\Delta_R H$ is the reaction enthalpy and c_{NH3} is the inlet concentration of ammonia in the gas mixture. The result provided by CFD simulation when calculated using the previously mentioned equation is about 757 K.

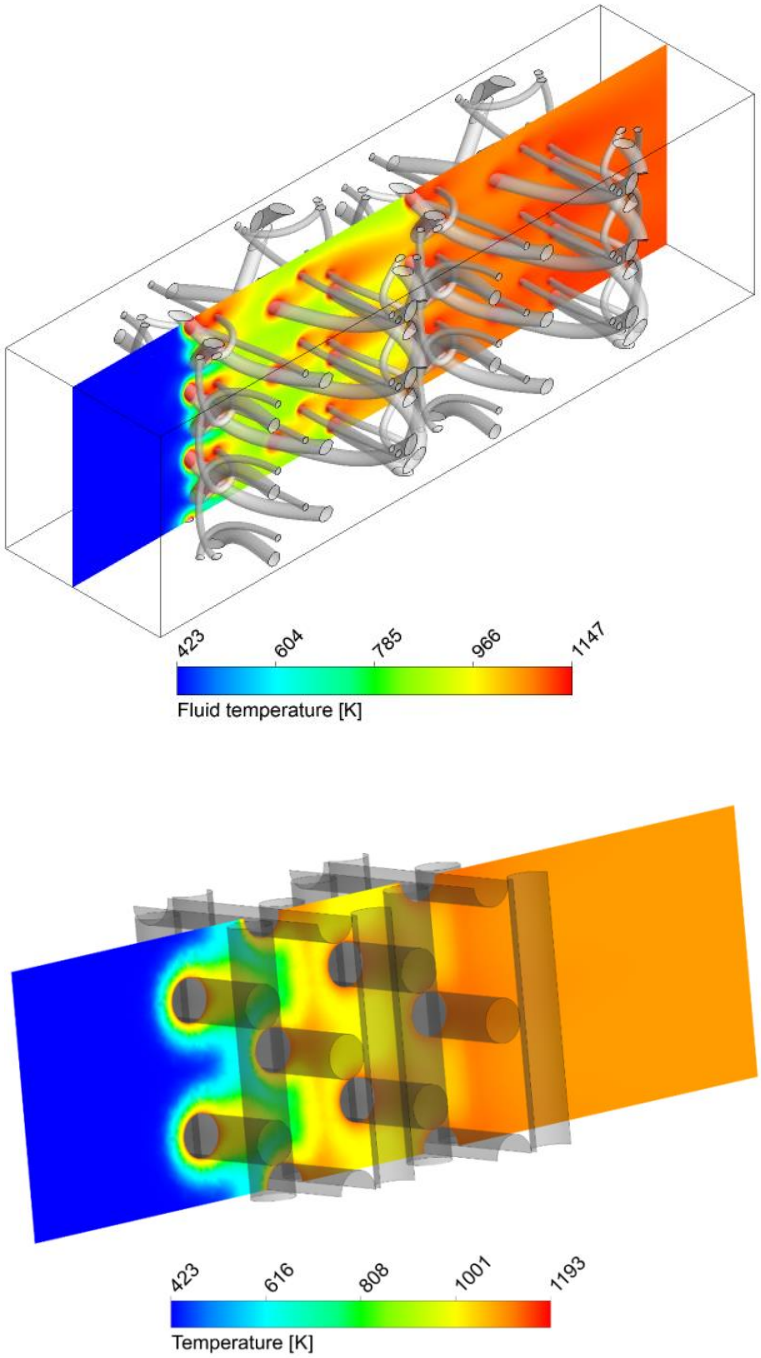

Figure 8.8: Temperature profile in the computational domain of the woven (above) and knitted (below) gauzes.

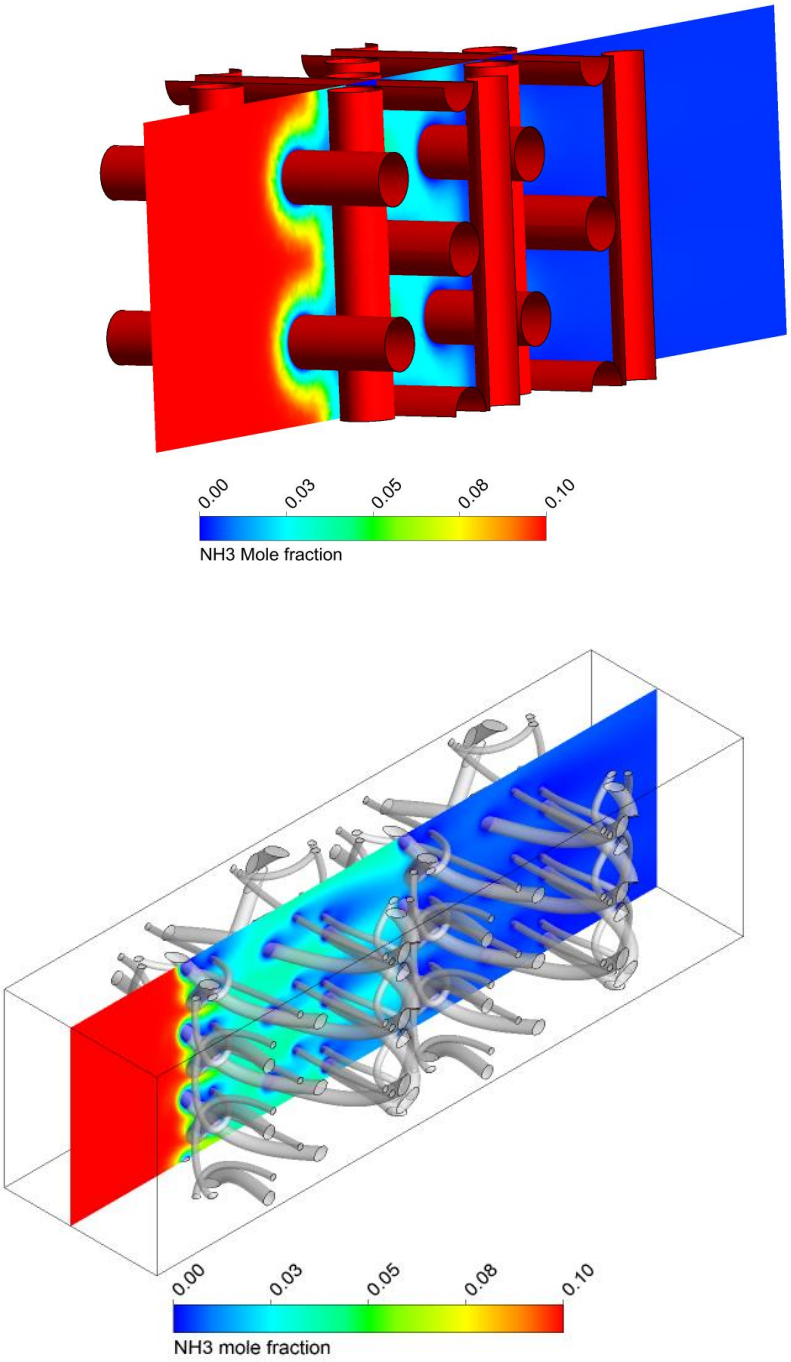

Figure 8.9: Ammonia mole fraction in the simulations computational domain.

The temperature calculated by both models is in good agreement with those reported for industrial ammonia burner (850-950 °C).

The adiabatic temperature increases proportional with the increasing gas inlet temperature. The temperature of the first gauze is always higher than the adiabatic temperature and is high enough to ensure that the reaction rate is controlled by external mass transfer. Therefore, the conversion of ammonia increases only very slightly with the increase of gas inlet temperature because the external mass transfer does not depend strongly on temperature. Furthermore, it can be observed that the increase in the temperature of the first gauze is accompanied by a decrease of ammonia conversion and also decreasing gas outlet temperature, which is quite astonishing. Nonetheless, the difference between gas mixture temperature and the surface temperature of the gauze is mainly driven by the interaction of mass and heat transfer effects. The change in concentration of the gas phase mixture (bulk) does not play a major role. Similar results have also been observed by Jess et al. [Jes2013]. Figure 8.10 shows the surface temperature profile of the catalytic gauze during the ammonia oxidation. The calculation has been done by CFD simulation at typical reaction conditions for a middle-pressure ammonia burner. The effect above is observable; the first gauze layer has higher temperature as rear part of the gauze.

The conversion dependency on pressure is significant. A pressure increase leads to a drop in the conversion. This observation is a result of the dependency of external mass transfer on total pressure. The mass transfer coefficient is inversely proportional to the total pressure. Also, the number of gauzes needed for full conversion is increasing with the total pressure. This is also the industrial experience; a high-pressure ammonia burner can have up to 50 catalytic gauzes.

The influence of linear flow velocity in the inlet of the reactor has also been investigated. The increase of the velocity leads to an increase of the side products, such as N_2O. Furthermore, the temperature of the first gauze rises with increasing velocity. The overall dependency on the velocity is significant because the reaction under industrial conditions is determined by external mass transport.

Noteworthy is the effect of velocity on the product selectivity. High linear velocities lead to an increase in N_2O production, which is also observed in industrial plants. This effect can be explained by the above mentioned relationship between mass transfer coefficient β and production rates.

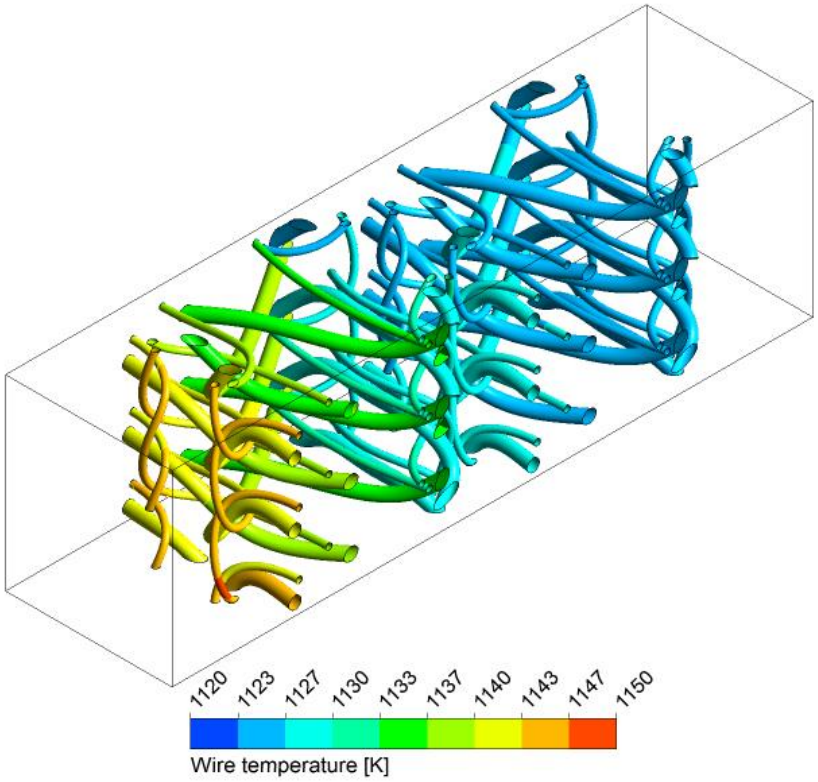

Figure 8.10: Temperature profile of the woven gauze. The results are taken from a CFD simulation with reaction conditions typical for a middle-pressure ammonia plant.

8.1.4. Woven vs. Knitted Gauzes

Nowadays there exists a large variety of different geometries for catalytic gauzes for ammonia oxidation, ranging from relatively simple flat geometries to very complex three-dimensional gauzes with different wire diameters. There are only very few rational or scientific explanations about how the catalyst geometry influences the reaction performance. The selectivity dependency on gauze geometry is reported frequently by catalyst suppliers and nitric acid producers. First attempts to explain and validate the influence of catalyst geometry on the ammonia oxidation process have already been made in the literature mentioned before [Nie2013, Kli2016]. Nonetheless, a direct science-based comparison between woven and knitted gauzes has never been made. The woven gauzes are usually reported to perform better in the industrial reactors. But the reasons for such behavior cannot be explained.

Taking into account the findings from Klingenberger and Nien, the next step in the understanding of the ammonia oxidation behavior under the industrial condition is the development and comparison of models with industrial knitted and woven gauzes geometries.

Two models were developed for this study: knitted gauze geometry with simple cross pattern and a model for woven gauze with a complex three-dimensional geometry. The models were designed in the way that the conversion of ammonia reaches almost 100 %, and the selectivity toward the products is comparable in both cases. The reaction conditions are a typical example of middle-pressure ammonia oxidation reactors with the pressure of 5 bar, the inlet temperature of 150 °C and inlet velocity of 1 m/s. The amount of cells in the computational domain is approx. 1e6. For the knitted gauze and 6x1e6 for the woven gauze.

The catalytic performance in both simulations can be evaluated by comparison of integral and differential selectivity. Thereby the most sensitive is the selectivity toward N_2O. Also, that side product is the most undesired one because of its greenhouse effect. The integral selectivity is calculated commonly and is the ration between produced product and converted ammonia.

Using the CFD approach, there is a unique possibility to calculate the local NO and N_2O selectivity on the catalyst surface and compare it with the local mass transfer coefficient.

The differential products selectivity can be calculated using the following equation 8.2-8.4, from the steady-state source terms of according species and taking into account the stoichiometry:

$$D_{S_{NO}} = \frac{\dot{S_{NO}}}{-\dot{S_{NH_3}}} \qquad \text{Eq. 8.2}$$

$$D_{S_{N_2O}} = \frac{2\dot{S_{N_2O}}}{-\dot{S_{NH_3}}} \qquad \text{Eq. 8.3}$$

$$D_{S_{N_2O}} = \frac{2\dot{S}_{N_2}}{-\dot{S_{NH_3}}} \qquad \text{Eq. 8.4}$$

The local mass transfer coefficient β (m/s) can be calculated by the following equation 8.5:

$$\beta = \dot{F} \cdot (c_{NH3,bulk} - c_{NH3,surf}) \qquad \text{Eq. 8.5}$$

$\dot{F}$ is the flow toward the wire surface, $c_{NH3,bulk}$ is the concentration of ammonia in the gas phase and $c_{NH3,surf}$ is the concentration of ammonia close to the catalyst surface.

The ammonia mole fraction profile of both models is shown in the Figure 8.11. It is remarkable that the ammonia is almost completely converted in the first two to three layers of catalyst. This is common behavior for both models. Therefore, the first catalyst gauze or layer

experiences the highest load, and the impact of the first catalyst gauze is the most significant on the overall process.

Using the source terms of reaction products calculated in the steady-state simulation, it is possible to calculate the differential selectivity directly on the surface of the catalyst. The following figure 8.11 show the differential N_2O selectivity on the catalyst surface in case of the knitted gauze model.

It is recognizable that the selectivity profile is consistent with the local mass transfer coefficient. Areas with high local N_2O selectivity correspond to areas with increased local mass transfer coefficient. We can make up three general trends:

- The mass transfer and the N_2O selectivity on the frontal part of the single catalyst wire are increased compared to the rear part.
- N_2O is mostly produced on the first gauzes in the catalyst package.
- N_2O selectivity and mass transfer "hot spots" on the catalyst surface are matching to each other.

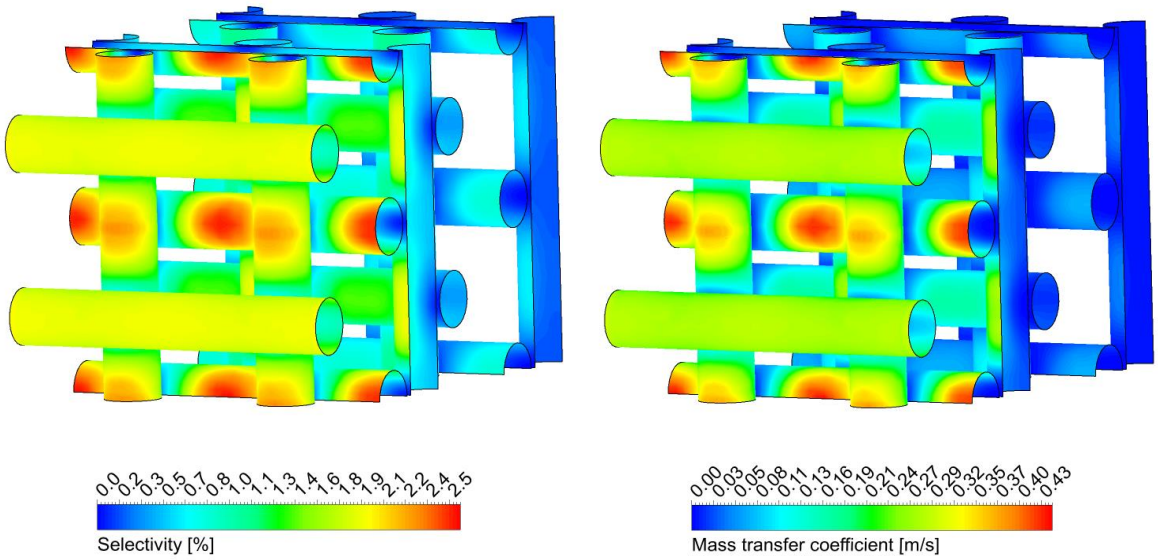

Figure 8.11: Local surface profile of N_2O selectivity and mass transfer coefficient on knitted gauze.

The general relationship between product selectivity and the mass transfer can be explained by "degree of rate control" calculations. According to the reaction mechanism and considering the mass controlled regime, an increased mass transfer coefficient causes an increase in the N_2O production rate, which can also be seen in the simulation's results.

Furthermore, the produced N_2O cannot be reabsorbed, and the reabsorption rate of NO is very low compared to the desorption rate according to the reaction mechanism by Krähnert. Consequently, after converting all ammonia, which happens as already mentioned on the first three to four catalytic layers, there is no more nitrogen source to produce any N_2O. Due to this behavior of the kinetic mechanism, the production rate of nitrous oxide (as well as the differential selectivity) becomes negligible in the rear part of the gauze package.

One of the possible reasons why the local N_2O selectivity on the gauze surface is not uniform could be the temperature gradient. The comparison of catalyst surface temperature and the selectivity pattern shows that this is not the case because the temperature varies from wire to wire but is uniform throughout the entire surface of one wire. This is easily explainable by the high thermal conductivity of platinum and platinum alloys, which makes a gradient along a single wire very unlikely.

An increase of N_2O production correlating with the increased mass transfer is observable in certain areas on the catalyst surface. The difference in nitrous oxide selectivity varies between 1 and 2.5 % on the frontal parts of the first three catalyst layers. Especially in the middle part of the third gauze, the N_2O selectivity reaches the highest value. The increase in this area can be explained by the acceleration of the linear flow velocity in this region.

General trends observed in the case of simple knitted catalyst geometries are present in woven gauze models too. N_2O differential selectivity profiles and local mass transfer coefficient profiles of a woven gauze model are shown in the Figure 8.12. It can be seen that the distribution of the selectivity is not uniform as well. Although the absolute maxima of N_2O selectivity reaches a higher number as in case of knitted gauze (woven maximal 3 % vs. knitted 2.5 %) the “hot spots” are smaller and “smoother.” The correlation with the local mass transfer coefficient is visible in this case too.

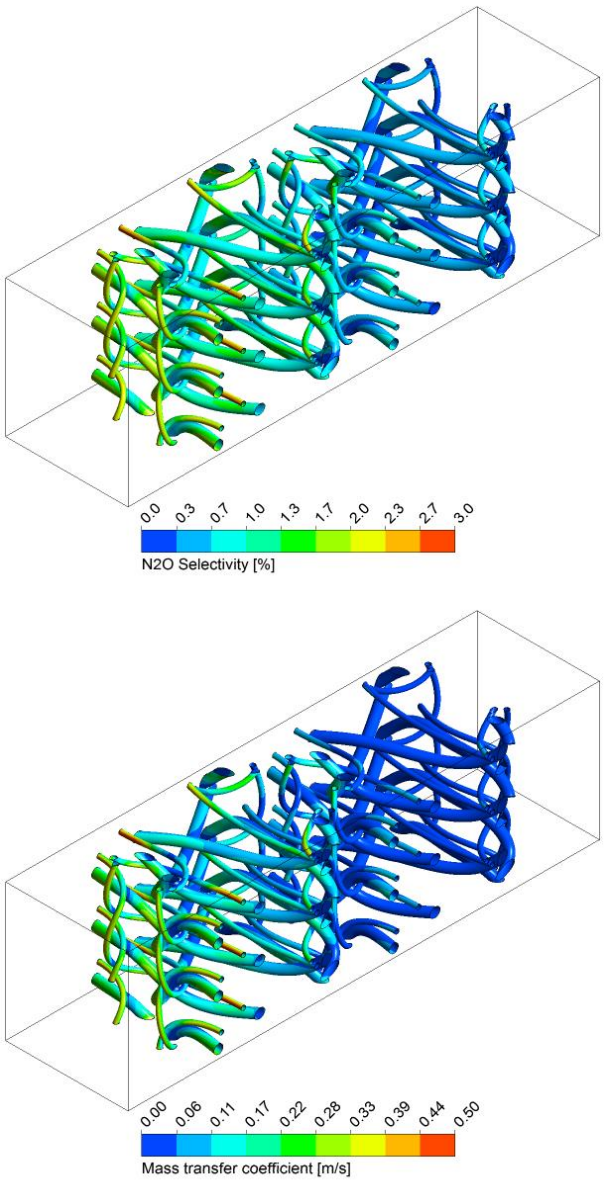

Figure 8.12: Local surface profile of N_2O selectivity and mass transfer coefficient on woven gauze.

The overall integral nitrous oxide selectivity on the domain outlet is 1.4 % in case of woven gauze and 1.7 % in case of simple knitted catalyst geometry. The better performance of the woven gauze can be attributed to a better N_2O “hot spot” distribution on the catalyst surface, which is generally caused by lower local mass transfer coefficients. The beneficial influence of the use of woven gauzes in industrial reactors can be explained by the influence of local mass transfer coefficients on the production rate of N_2O. Woven gauzes have more regions with a lower mass transfer coefficient, which causes a lower N_2O production.

8.2. Summarizing remarks

A computational fluid dynamics model combined with detailed kinetics for complex industrial used catalyst geometries has been developed in the presented work. The general trends of ammonia oxidation under industrial condition can be reproduced by the computational model. Moreover, a comparison of CFD simulation with pilot plant experiments provides satisfactory correlation. The influence of inlet temperature, linear velocity and operating pressure on reaction performance has been investigated using modeling. The general behavior of ammonia oxidation under industrial conditions is well described by the developed model.

The temperature profile in the catalytic package has been investigated. The simulation results correspond to the calculation of adiabatic temperature rise and other calculations based on dimensionless numbers.

The beneficial effect on catalyst performance of complex woven geometries has been shown by simulations. The scientific explanation based on local differences of mass transfer coefficients has been provided for this effect. Although the modeling results has not been experimentally validated until now.

Furthermore, the described approach can be used for a better, more optimal design of catalytic gauzes for ammonia oxidation. Combined knowledge from researches of Klingenberger, Teng-Wang and the present work lead to a science-based geometry design. There is no more need for expensive tests of several prototypes. The first test can be done using the presented techniques combining CFD and detailed kinetic modeling. Only the best performing model should be built as a prototype and tested in a pilot plant. It will significantly reduce the number of required experiments and the overall time for developing and commercializing of new catalyst types.

9. CFD Simulations based on Tomography images

Nowadays, computational fluid dynamics (CFD) has become a standard tool for flow simulations in different research fields due to the advent of fast computers combined with the development of accurate numerical algorithms for solving physical and chemical problems. However, CFD simulations of irregular structures or large models are still challenging because of the computational time and hardware required. Nonetheless, a combination of microtomography (μ-CT) based images, which can capture and reproduce structures with a resolution of several micrometers, and CFD flow simulations can reveal a better understanding of several processes in different research fields. Such models are much more detailed and accurate for the predicting of physical and chemical properties of different materials compared to common simplified approximation approaches. A combination of μ-CT and CFD was recently successfully applied in such research fields like blood flow in human vessels [Owe2016, Ray2013] and flow through porous media and foams [Del2014, Fan2016, Ran2014, Zer2014]. Computer tomography has already been used for the visualizing of catalyst surfaces for ammonia oxidation [Pur2013, Pur2015]. A CFD study based on such CT images for ammonia oxidation catalyst has not been applied until now.

Heterogeneously catalyzed ammonia oxidation is the first step of nitric acid production (Ostwald Process). The reaction of ammonia (10-12 vol. % NH_3) with air oxygen occurs on platinum-rhodium or platinum-rhodium-palladium knitted or woven gauzes at a high temperature (800-900 °C) and pressure from 1 to 16 bar. The catalyst package in the industrial burner consists typically of 1 to 50 gauzes, depending on operating pressure. At industrial operating conditions, ammonia oxidation is a typical example of limited diffusion reaction, where the surface reaction is very fast (time scale of 10^{-11} s) compared to the transport of species to the catalyst surface. This aspect makes the investigation of the kinetic mechanism and determination of intermediate species under industrial operating condition very challenging or even impossible. There exist a significant number of studies which introduce the kinetic mechanism for ammonia oxidation [Sch2005, Raf2012, Reb2002, Kra2008], but most of the mechanism has not been tested in the mass transfer limited regime [War2013]. The approach described in the current contribution gives the opportunity to investigate this system by effective coupling of surface reaction using the rate mapping method [Vot2009] and flow dynamic simulation. The kinetic mechanism provided by Kreahnert [Kra2008] and adapted by Scheuer [Sch2009] is used in this work.

The originally smooth catalyst surface undergoes heavy reconstruction during the first hours of operation in the burner. It was shown that this process starts on the grain boundaries and soon the entire surface is covered by “cauliflower”-like excrescences [Han2005]. This phenomenon leads to an increase in wire diameter and surface area but is accompanied by mechanical degradation of catalyst and loss of expensive platinum. The surface reconstruction is most extensive on the front sites of the first two or three gauzes in the ammonia combustor. The increase in the surface area of the first gauze is reported to be ten times the area of a new gauze [Ber1996, And1988]. Under the industrial condition of ammonia combustion, Pt (and Rh) is drained from the catalyst surface by forming a volatile metal oxide (PtO_2). Platinum oxide acts as a transporting molecule and this process is driven by local temperature gradients on the catalyst surface. Part of PtO_2 quickly decomposes on the surface forming the characteristic cauliflower excrescences. One part decomposes on the catchment gauzes and the other part exits the burner and cannot be recycled anymore [Pur2015].

More recently, platinum wires, after being in the ammonia burner for six months, were examined by modern analyzing and visualizing techniques like scanning electron microscopy (SEM), energy-dispersive X-ray spectroscopy (EDS) and micro X-ray computer tomography (μXCT) [Pur2013, Pur2015]. EDS makes it possible to analyze the content of Pt and Rh on the wire cross-section. By using the μXCT technique, the change in volume, surface area, and cross section shape can be investigated.

In this work, μ-CT is used to generate geometry for fluid dynamics simulations with the preserved structure of the wire surface, which has been in an ammonia combustion process for several hours. By using ScanIP software, volumetric CT data is transformed to a 2D image stack, that is processed into a 3D CAD model. The CAD geometry is meshed and exported in relevant file formats for numerical simulation in commercial software Ansys Fluent. The CFD simulations are performed for two cases considering heat and mass transfer, as well as the detailed kinetic mechanism under industrial conditions. In the first case, the geometry is based on CT data and takes into account the restructured wire surface. The geometry in the second case consists of a smooth catalytic wire. Regardless, with all of the improvements in the computational technologies, it is still impossible to perform simulations of a large section of catalytic wire while taking into account the restructuring process. The current contribution examines how the cauliflower excrescences influence the general flow pattern around the catalytic wire and validate the assumption of simulation, which doesn’t take into account the restructuring process.

9.1. Methodology

9.1.1. Image processing and mesh generation

The tomography images have been made in a high resolution industrial computer tomography scanner. The original 3D CT data was transferred to a stack of 2D pictures, which were produced by slicing the 3D data along the x-axis in a certain distance to each other. The image stack was imported in SIMPLEWARE software ScanIP and was stitched together resulting in a 3D CAD model. Sharp edges and islands were removed from the geometry by using implied filters within the software.

The computational grid was created by ScanIP, resulting in a high-quality triangular mesh. The whole computational domain contains 3.7 million cells. The tomography image and the computational mesh are shown in the figure 9.1

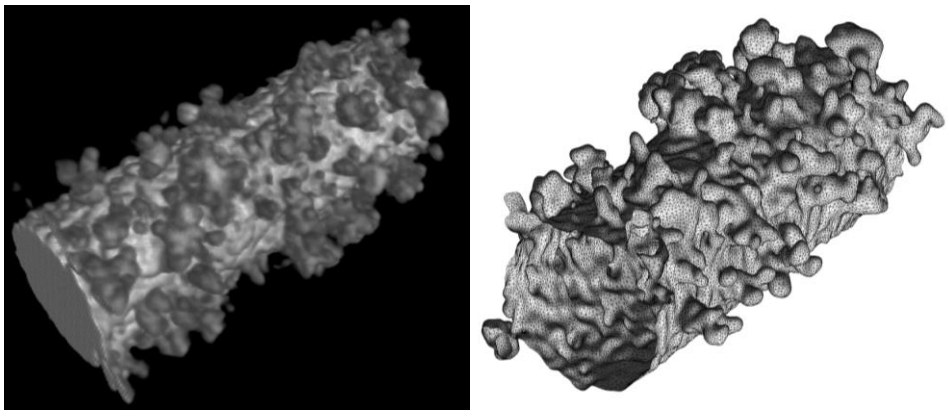

Figure 9.1 (left): CT image of Pt wire after several days in ammonia burner; (right): FEM model used for the CFD simulations.

The fluid flow along the catalytic gauze was calculated using Ansys Fluent (v. 16.2). Due to a low Reynolds number (1-40 depending on inlet velocity) the flow is considered to be laminar. The governing equations solved for the mathematical model are continuity equation, Navier-Stokes equations (conservation of momentum) and conservation of energy for an incompressible fluid. All other model parameters and species properties are the same as in all other models presented in this work.

The detailed surface kinetic mechanism provided by Kreahnert is implemented in simulations using the spline mapping approach [Vot2009]. Tables contain the steady state surface source terms of key species (NH_3, N_2, and N_2O) as a function of the relevant scaled dimensions (1/T, $\ln(xNH_3)$, $\ln(xNO)$, $\ln(xO_2)$). The details of the rate mapping approach for ammonia

oxidation are described elsewhere [Vot2009, Kli2017b]. This method allows the decoupling of numerical treatment of the process on the catalytic surface and the flow calculation because the CFD simulations become faster and more stable. The calculation is proceeded until the system is in a steady state and the residuals are lower than 10^{-5}. All numerical calculations were performed on HHLR Lichtenberg cluster.

The computational domain contains 3.7e6 triangular elements with appropriate quality. The length of the domain is 0.773 mm, the height is 0.437 mm and the width is 0.336 mm. The boundaries conditions for top and bottom as well as left and right surfaces of the domain are set as symmetrical. For the comparison of smooth and restructured surface models, the temperature of the wire is set to 1100 K in all cases.

The boundary conditions for the CFD simulations are set as follows: At the outlet, the boundary condition is set as pressure outlet; a velocity inlet boundary condition is employed at the inlet; the inlet temperature is 150 °C; the mixture contains 0.1 mol fraction ammonia, 0.2 mol fraction oxygen and the rest is nitrogen. The inlet velocity is 1 m/s. Left, right, upper and lower boundary conditions are set as symmetrical. The operating pressure is 5 bar, which is a typical condition for middle-pressure industrial plants. Two types of simulations with restructured wire were performed. In the first case, the temperature of the wire was set artificially to 1100 K. And in the second case, the temperature was set free and reached a steady-state temperature due to the unleashed heat of the reaction.

9.2. Results and discussion

9.2.1. Flow field around a restructured wire

The streamlines around the restructured wire, as well as the computational domain used in all of the simulations, are shown in the following figure 9.2. As can be expected, the flow has a stagnation point in the front of the wire. The velocity around the wire is increasing, and a fully developed vortex can be observed in the rear part of the catalytic wire. The velocity range is between 0.75 and 2 m/s. The flow around a cylinder can be assumed as completely laminar due to very low Reynolds numbers (Re 2-7).

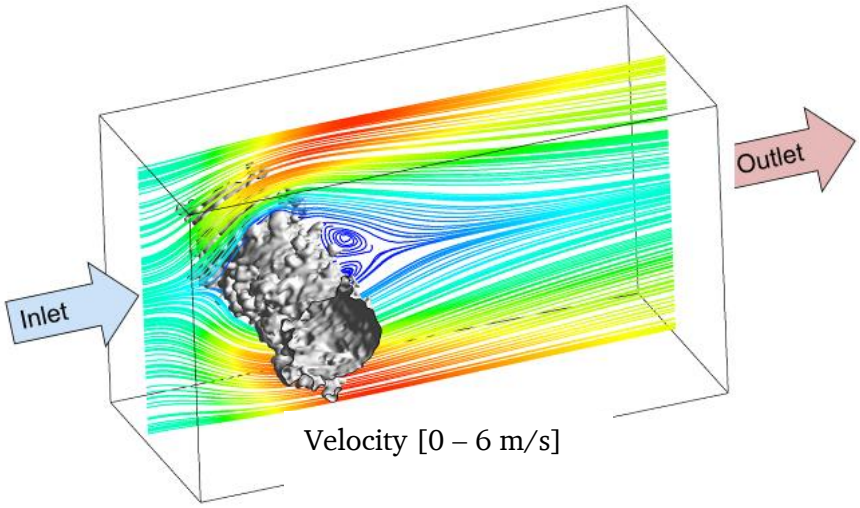

Figure 9.2: Computational domain of reconstructed wire with velocity streamlines.

The reconstruction and the growth of cauliflower structures on the surface increase the diameter of the wire as well as the surface area, which leads to a rise in the conversion. The experimental measurements (physical adsorption of Kr) shows an increase of the wire surface area of about one order of magnitude [Ber1996, And1988]. The influence of this factor in the case of simulations with the smooth surface can be adjusted with a numerical factor, which multiplies the Arrhenius factors in the kinetic mechanism by 10. Using this parameter, performed simulations show an increase in the conversion of ammonia and values for the selectivity of nitrous oxide, which can be observed in the industrial ammonia combustion (Tab 1). Such behavior is in agreement with industrial practice. The increased N_2O amount can be observed at the beginning of the industrial campaigns too. After several operating hours, the gauze's surface get restructured, the diameter of single wires rises, and the N_2O

selectivity drops to an average value between 1 and 2 %. The effect of surface enlargement leads to the rise of the available active site on the catalyst.

Nevertheless, the process is limited by mass transfer. The concentration of ammonia close to the wire surface decreases, which leads to the change of kinetic rate. With higher ammonia concentration, the production of species with two nitrogen atoms is more favorable. Considering this fact, a drop in ammonia concentration close to the wire surface is followed by a drop in production of nitrous oxide. The model based on CT-images offers a more realistic picture of the wire surface whereby even high-resolution CT scans cannot reveal all details of the cauliflower surface. Due to this, there is a need to apply a numerical surface factor for restructured wire simulation as well. In this case, the surface enlargement by cauliflowers is taken into account. The numerical factor is smaller as in case of smooth wire and is set to 4.4 considering the difference in the wire surface between smooth and restructured wire, which is 1.16 e-07 m^2 and 2.59 e-07 m^2 respectively.

Table 9.1 Conversion, NO selectivity and N_2O selectivity provided by CFD simulations of smooth 0.1 mm wire with and without the surface area factor.

	0.1 mm smooth wire with surface area factor of 10	Restructured wire with surface area factor of 4.4
Conversion [%]	22	26
NO Selectivity [%]	96	94
N_2O Selectivity [%]	1.7	3.3

9.2.2. Influence of restructured surface on N_2O Selectivity

After the equalization of the catalytic surface by numerical factor and the same boundary conditions, the expected catalytic performance (N_2O selectivity) for the smooth and restructured wires should lie in the same range. Nevertheless, an increased nitrous oxide production is observable in the case of restructured wire. Furthermore, there is a strong variation in the distribution of local differential N_2O selectivity on the catalyst surface of the restructured and smooth wires. As can be seen in the following picture (Figure 9.3), the selectivity toward nitrous oxide variesbetween approximately zero and 7 % in case of restructured wire and between approximately zero and 2.1 % by a model with the smooth

surface. Also, it is observable that the tips of cauliflower structures have the highest N_2O selectivity which is caused by high ammonia concentration in those regions.

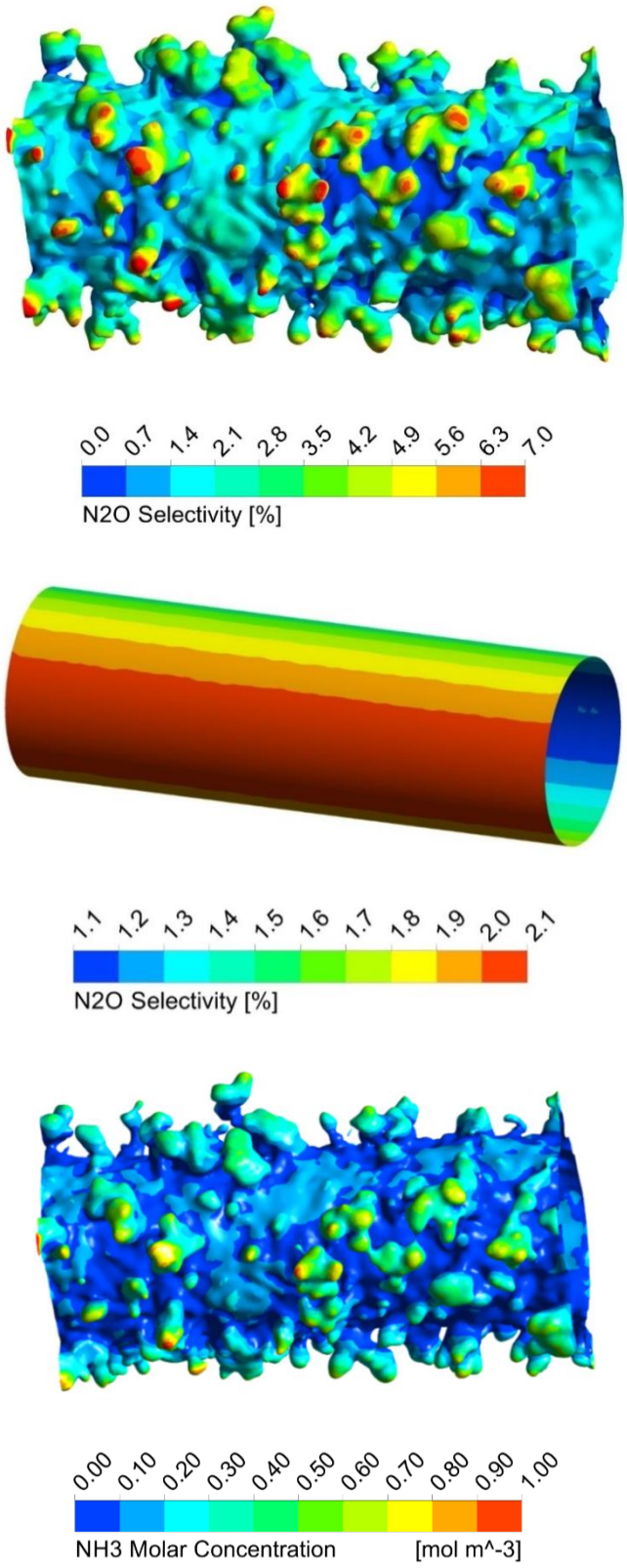

Figure 9.3 (a): The N_2O selectivity surface profile of the restructured wire. (b): The N_2O selectivity surface profile of the smooth wire. (c) Surface concentration of ammonia on the restructured wire.

It is noteworthy that the average of differential selectivity on the wire surface cannot be correctly computed by a simple numerical median. Such an attempt results in much lower N_2O selectivity as it is at the outlet of the domain (integral selectivity). To understand such behavior, the following plot should be considered (Fig 9.4).

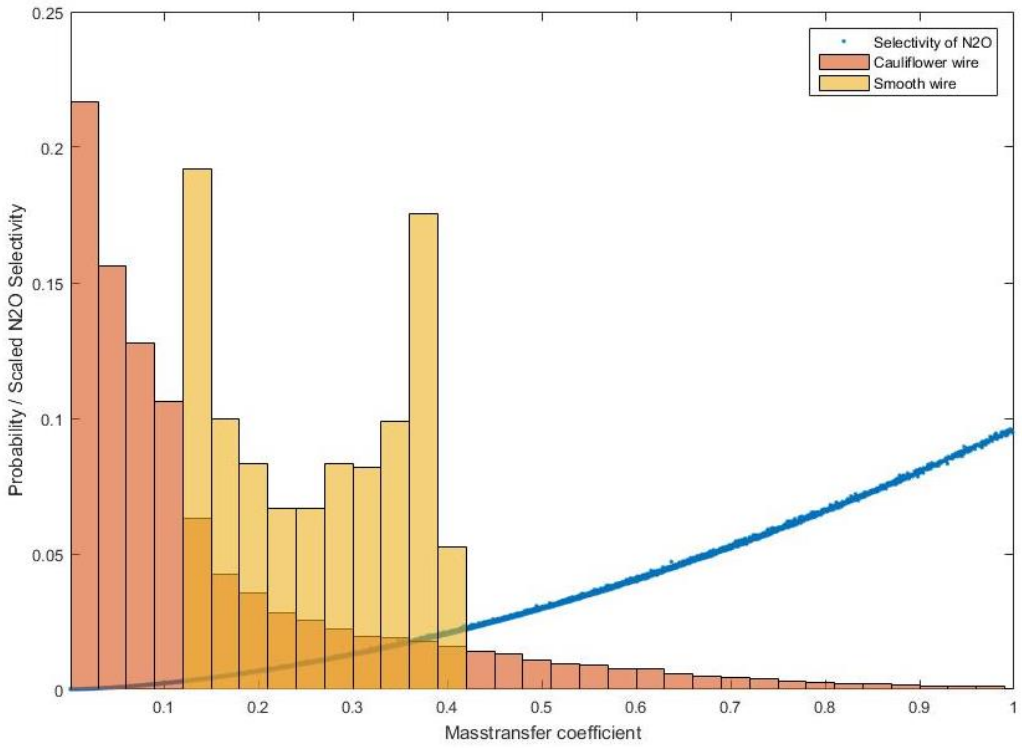

Figure 9.4: Distribution of N_2O selectivity and mass transfer coefficient on the surface of cauliflower and smooth wires.

Fig. 9.4 shows the distribution probability of domain elements and the corresponding mass transfer coefficient. Furthermore, associated N_2O selectivity is shown in the same plot. The relationship between the rise of selectivity and mass transfer coefficient is nonlinear, and by increased coefficients the increased nitrous oxide production is observable. The tips of cauliflower structures participate much more on the reaction because they are much more in contact with the reacting mixture containing a high amount of ammonia. The regions located on the wire body participate in the reaction on the lesser grade. As a result, it can be concluded that the tips of cauliflower structures participate more in the reaction and produce more nitrous oxide with higher selectivity. Thus, the calculation of average differential N_2O selectivity should be done with ammonia concentration weighted selectivity. The resulting differential selectivity on the catalyst surface matches the integral selectivity on the domain outlet.

Considering the nonlinear influence of cauliflower structures on the nitrous oxide formation the surface adjustment only by numerical factor is not appropriate in this case. In contrast to the restructured model, wire with a smooth surface does not have an ammonia concentration gradient in the radial direction, and all the elements of the catalytic surface with the same x coordinate in the model are participating equally in the reaction. In case of restructured wire, there is a strong variation in the ammonia concentration profile on the wire surface, and due to that, a strong variation in N_2O selectivity. Therefore, tips of cauliflower structures, where the N_2O selectivity is highest, participate most in the reaction and consume a significant part of ammonia. For a better comparison of both models, a surface enlargement factor of 10 is implemented in simulations with the restructured catalytic surface as well. This practice leads to a similar result in both cases. It can be explained by the fact that the predominant amount of ammonia is burned on the tips of cauliflower structures where the ammonia concentration (in case of surface factor 10) lies in the same region, as in the case of smooth wire.

9.2.3. Influence of the wire diameter and velocity on N_2O selectivity

The increase of the wire diameter leads to the decrease of the space between two wires in the gauze, which causes the acceleration of the velocity in the domain. Simulation with different wire diameter and flow velocity were performed to evaluate the dependencies of those factors on the conversion (Fig 9.5). By doubling the wire diameter and the equal inlet velocity of 0.75 m/s, the conversion rises from 24 % for 0.1 mm to 38 % for 0.2 mm. By increasing the inlet velocity from 0.75 m/s to 1.5 m/s, the conversion drops down toward 15 % for 0.1 mm wire and to 24 % in case of 0.2 mm wire diameter. An increase in the velocity causes a drop in the conversion, which can be explained by shorter residence time of reactants on the catalytic surface. On the other hand, the increase of the wire diameter is followed by conversion gain. The explanation for this behavior is the increase of the active catalytic area.

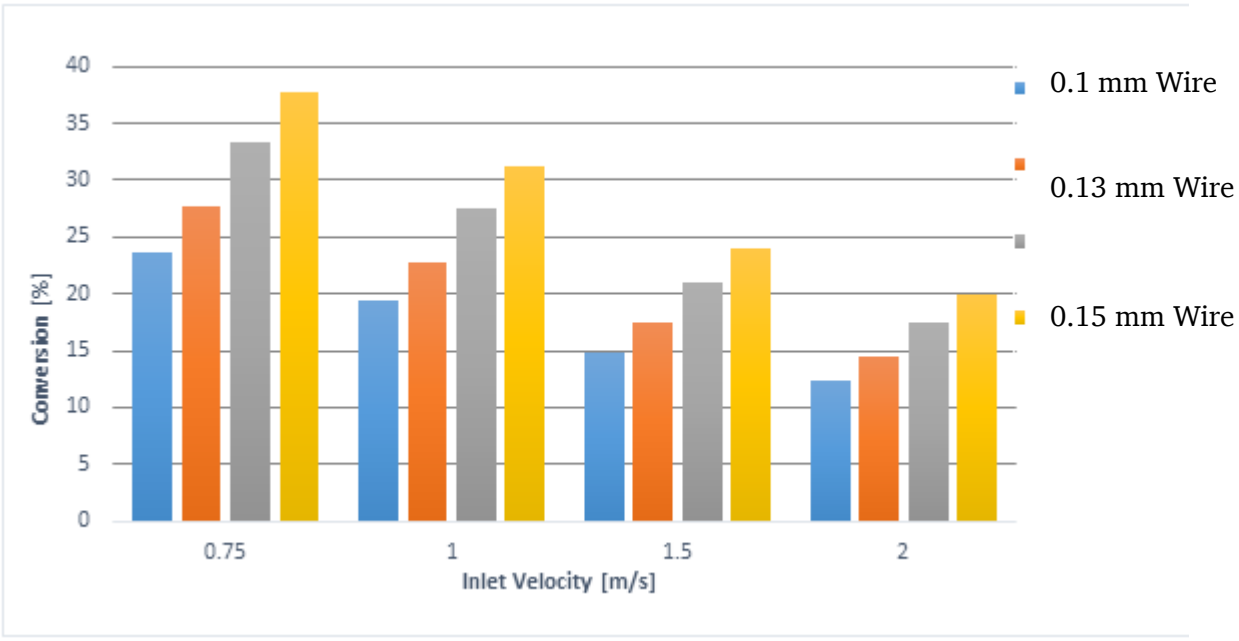

Figure 9.5: Resulted conversion from CFD simulation of geometries with different wire (0.1, 0.13, 0.15 and 0.2 mm) diameter and variating inlet velocity.

Taking into account the dependencies of inlet velocity and wire diameter it is crucial to choose a similar velocity profile around the wire for the correct comparison of the model with smooth and restructured wire surface. For this purpose, a median diameter of restructured wire has been determined. The distance between different opposite points on the restructured wire surface has been measured. And an average value has been calculated, being in the range of 0.15-0.16 mm (Fig 9.6).

Figure 9.6: Black is the cross-section of the cauliflower wire, the diameter (0.15 mm) of the smooth wire is red.

The flow velocity profile in the computational domain is illustrated in Figure 9.7. Regarding the dependency of NH_3 conversion from velocity, it is crucial for the correct comparison of both models to ensure the same velocity profile. It is observable that the general flow pattern is not disturbed by the cauliflower excrescences. The outstanding structures are too small relative to the wire diameter to introduce any significant changes in the flow. In both cases,

the velocity is enhanced to a maximal value of approximately 2.2 m/s by inlet velocity of 0.75 m/s (Fig 6). The velocity near the wire surface becomes zero due to the chosen no-slip wall boundary condition.

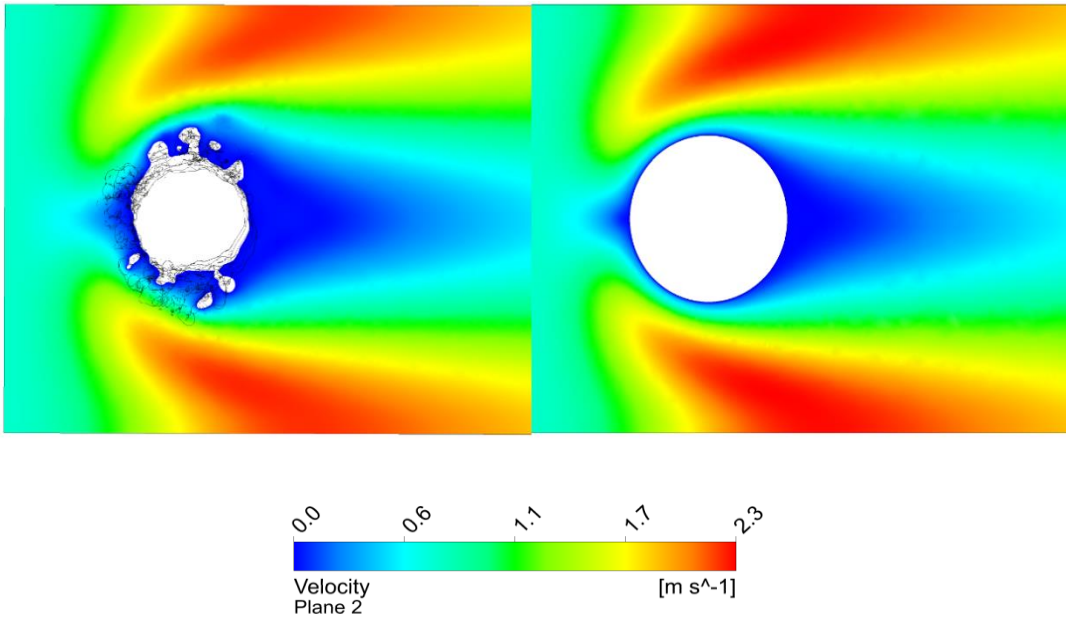

Figure 9.7: Velocity profile in the model domains with restructured wire (left) and smooth wire (right).

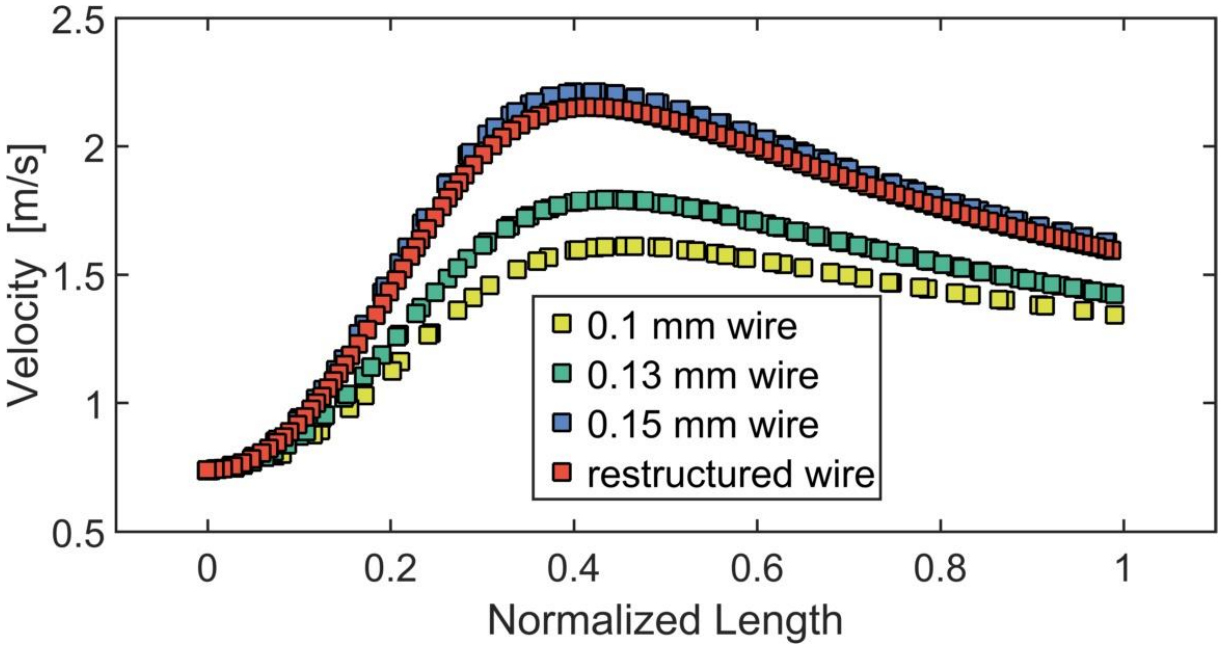

Figure 9.8: Flow velocity in the computational domain along the upper boundary by different wire diameters.

The NH_3 mole fraction profile in the computational domain is shown in Figure 9.9. The gradient and decrease in the amount of ammonia near the wire are a result of combustion reaction, which is limited by mass transfer. Near the wire surface, the mole fraction of

ammonia is close to zero. In this case, the general pattern of ammonia distribution in the domain is very similar in both cases. The surface area of the restructured wire is twice as large as the surface area of the smooth wire.

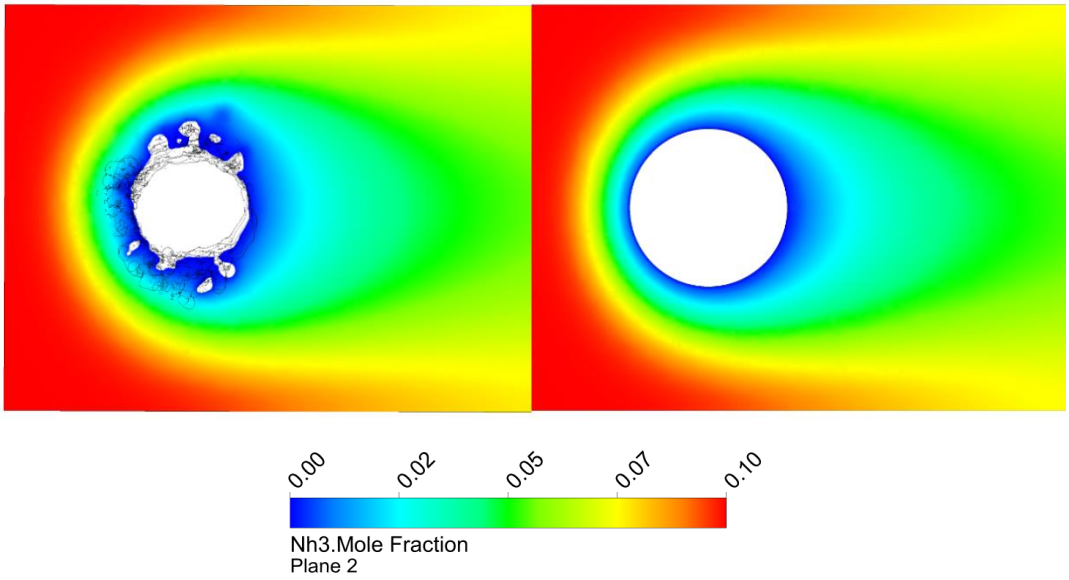

Figure 9.9: NH_3 mole fraction profile in the model domains with restructured wire (left) and smooth wire (right).

The following table 9.2 represents the simulations results with the same surface area factor. Despite the same surface factor and approximately equal diameter, the N_2O selectivity differs in both models. It can be explained by the irregular distribution of N_2O selectivity on the surface of restructured wire. It should be mentioned, that the tips of the cauliflower structures produce the majority of N_2O. In addition, the ammonia oxidation reaction is taking part overwhelmingly on the excrescences. As a result of such behavior, the N_2O selectivity is still different in both cases, despite the same surface area factor.

Table 9.2: Catalytic performance calculated by the model with restructured and smooth wires

	0.15 mm smooth wire with surface area factor of 10	Restructured wire with surface area factor of 10
Conversion [%]	25	26
NO Selectivity [%]	95,5	96
N_2O Selectivity [%]	1.34	1.64

The surface area factor is applied for the whole surface. In the case of uniform reaction distribution by simulations of smooth wires, it is a good assumption. But in the case of a cauliflower model, the situation is more complex.

To make a comparison between two models and to depict the N_2O selectivity with a more simple smooth wire model, the surface area factor should be adjusted. The variation of this parameter shows the best fit in N_2O selectivity between two models in case of the surface area factor of 7.3 for the smooth wire model. Furthermore, when the surface factor employed by smooth wire represent the same factor as the physical surface enlargement, a drop in N_2O selectivity by about 50 % (net selectivity of 0.82 %) has been predicted by such model. The following Table 9.3 presents the achieved results.

Table 9.3 Catalytic performance calculated by the model with restructured and smooth wires

	0.15 mm smooth wire with surface area factor of 7.3	Restructured wire with surface area factor of 10
Conversion [%]	25	26
NO Selectivity [%]	95,5	96
N_2O Selectivity [%]	1.64	1.64

9.2.4. Variation of Inlet conditions for smooth and restructured wires

The variation of inlet conditions in the models with restructured smooth wire has been made for the validation of the assumption made in the previous chapter. The variation parameters are the inlet velocity and the inlet temperature. The results are represented in Figure 9.10. It can be seen that the deviation of the models is low and amounts only 1%.

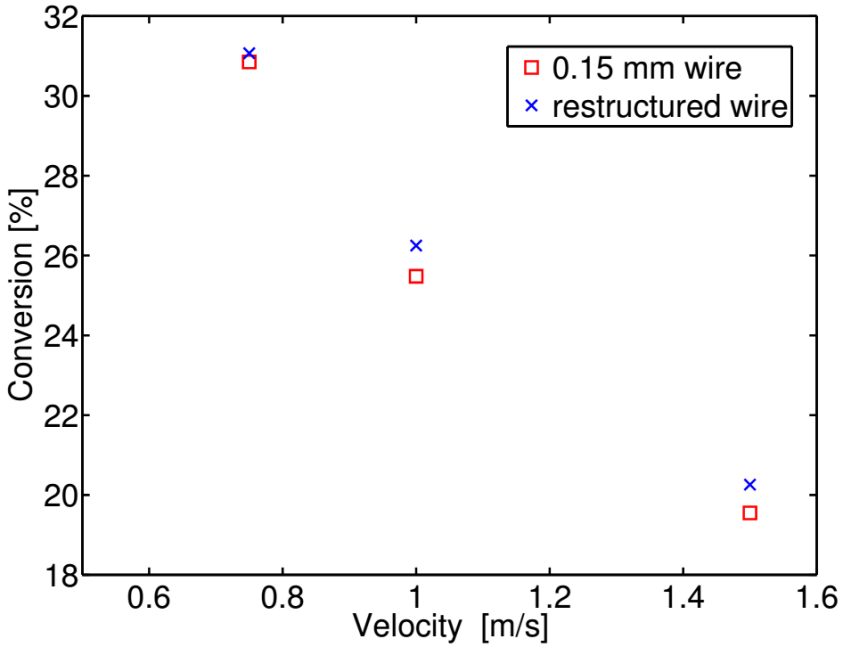

Figure 9.10. Comparison of conversion in restructured and smooth wire (d. 0.15 mm) models by different inlet velocities.

Furthermore, the variation of inlet velocity and temperature influence the N_2O selectivity, which is a very sensitive parameter in those models. The following Figures 9.11 and 9.12 show a very good fit for smooth wire model applying a surface area factor of 7.3 with the restructured model.

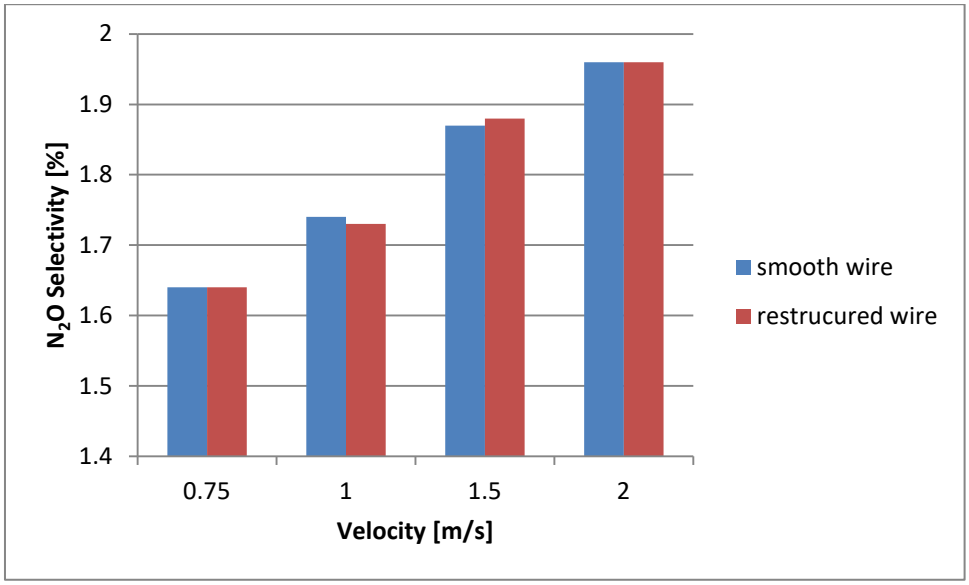

Figure 9.11: Variation of inlet velocity and resulted N_2O selectivity for the restructured wire model and the smooth wire model with 0.15 mm wire diameter and surface factor of 7.3.

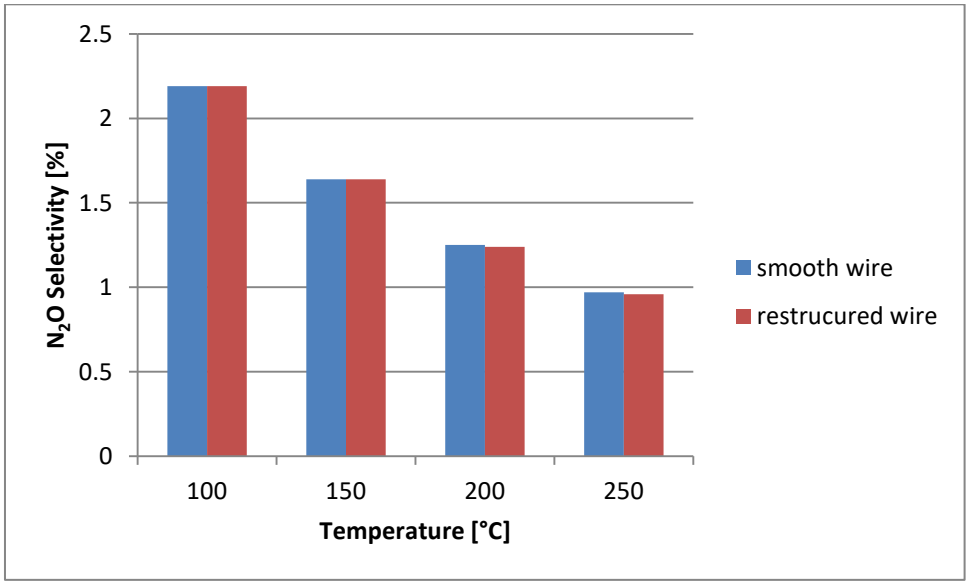

Figure 9.12 Variation of inlet temperature and resulted N_2O selectivity for the restructured wire model and the smooth wire model with 0.15 mm wire diameter and surface factor of 7.3.

Considering the negligible deviation between both models, it follows that the correction of the wire diameter and the use of the adjusted surface factor lead to very similar results. Using this knowledge, it is possible to perform simulations with simplified smooth wire and adjust the surface area factor to reproduce the results of more complex models based on computational tomography.

9.3. Summarizing remarks

We have developed a CFD model based on micro-CT images for platinum catalyzed ammonia combustion under industrial conditions. The surface structure of the platinum wire after several hours in process was well represented in the realistic 3D model and transferred into a CAD model by high-resolution computer tomography images. The model's geometry was accurately discretized (meshed) using the software ScanIP and CFD simulations were performed in a commercial tool Ansys Fluent for the evaluation of the influence of surface structures on the fluid flow characteristics, heat transfer and reactive behavior of platinum catalyst. The results of this simulation were compared with CFD simulations of models which contain idealized wire geometry with a smooth surface.

The CFD simulations of smooth wire revealed that there is a need to implement an artificial numerical factor for the surface area to take into account an enlargement of the wire surface during the ammonia oxidation. The restructuring process leads to an increase in the wire diameter, which can crucially influence the flow pattern in the domain and enforce flow velocity acceleration. The variation of the velocity and wire diameter shows that the catalytic performances of ammonia conversion is dependent on these factors. With fast flow velocities and small wire diameter, the conversion drops due to faster contact time with catalyst and fewer available catalytic surfaces. Furthermore, the N_2O selectivity increases with increasing flow velocity and decreasing wire diameter.

The CFD simulations of catalytic restructured wire provide interesting results. The differential N_2O selectivity on the wire surface varies locally. This behavior is caused by different local mass transfer coefficients. In regions with an increased mass transfer, the production of N_2O is increased.

In the first simulations, the surface enlargement factor of cauliflower wire has been adopted to reproduce the overall surface area of the catalyst. Considering such adjustment, both models (smooth and restructured models) should have the same catalytic performance. Surprisingly, it was not the case. The detailed analysis of the results from the restructured model revealed that the combustion of ammonia happens predominantly on the tips of the cauliflower structures. These catalyst regions have the highest mass transfer coefficients and, because of this, the highest N_2O selectivity. The catalyst part under the cauliflower structures is obstructed by those structures and participates in the reaction only slightly. Considering this observation, the surface enlargement factor cannot be scaled only due to the comparison of the physical areas of both models. Much more important is the comparability of the catalytic

performance and surface factors in the areas where the reaction is overwhelmingly taking place. The smooth wire model is able to reproduce the results of the more complex model with restructured catalysts surface if the surface factor has been adjusted correctly. The same behavior can be seen by variation of the inlet condition such as temperature and velocity.

Furthermore, for the correct comparison of simulations with restructured and smooth wire surface, the diameter of the smooth wire was adjusted to the average diameter of the cauliflower wire. The simulations revealed that the cauliflower structures did not influence the general flow pattern in the computational domain due to their small size.

One of the important results of this study is the combination of detailed CT based models with computational fluid dynamics simulations considering the catalytic surface reaction. Furthermore, it was shown that the simplification of the wire geometry by considering only a smooth catalytic surface and implementation of the surface enlargement factor could describe a real behavior of ammonia oxidation with sufficient accuracy. Nonetheless, the CFD models of restructured wire surface can provide ideas of the formation mechanism of cauliflower structure and loss of platinum during the ammonia oxidation.

10. Laboratory scale reactor model

It exist a significant scale gap between laboratory scale reactors with few centimeters diameter and industrial burners, which have a diameter of some meters. The mass and heat transfer phenomena are different considering such a big scale up and can take significant impact on comparableness of the results produced by the laboratory scale plant with data from industrial ammonia converter. Due to neglecting of that fact the validation of provided kinetic mechanisms with experimental data from laboratory scale reactor and the transfer of those to industrial level become difficult. In the last three decades the advent of the fast computers combined with the development of accurate numerical algorithms for solving physical and chemical problems allows us the performing of computational fluid dynamics (CFD) simulations of ammonia oxidation process by industrial conditions with included detailed surface kinetics. The modelling of the laboratory scale reactor aims to investigate the ammonia oxidation in the small scaled reactor using CFD simulation combined with detailed surface kinetic mechanism. The possible thermal end-effects in the catalytic gauze and their impact on overall results of small scaled reactor are particularly from interest. The current study should scrutinize the comparability of data provided from laboratory reactor and industrial burners.

10.1. Simulation model development

Kinetic model

The kinetic model (model C) previously published by Kraehnert and Baerns was chosen for the implementation in a CFD simulation, because it provided the best correlation between experimental and computed rates of product formation in the Kraehnert work [Kra2008]. Reactions that might be possible in the gas phase are neglected in this work. There is no agreement in the research about the role of gas phase reactions during ammonia combustion.

That mechanism is a further advancement based on the kinetic model on Pt/Al_2O_3 near atmospheric pressure from Rebrov et al. [Reb2002]. In the mechanism, the polycrystalline Pt-surface of the catalytic gauze is assumed to be similar to Pt (1 1 1) surface. The energetic data for adsorption of species on a Pt surface, provided by DFT calculation from Offermans et al. was used in the model [Off2006]. The stepwise activation of ammonia (hydrogen stripping by oxygen atoms [Nov2005, Off2006]) is simplified in one stoichiometric reaction with the assumption that the first step (NH_3 + O) is rate determining. The production of water is also

included in that step. [Gla1978] The mechanism includes two different adsorption sites on Pt surface: sites “a” for O, N, and NO and sites “b” for NH_3. Due to the same adsorption site for oxygen and nitric oxide there exist a competition between them. That fact is also proved by spectroscopic evidence [Goh1986, Gla1980].

The mechanistic surface kinetic model was implemented in a CFD simulation using the rate mapping approach previously published by Votsmeier. The purpose of the rate mapping procedure is to provide source terms for the gas species by interpolation of a spline function between a certain number of points in a rectangular grid. The spline function represents a functional relationship between the input parameters and the gas phase source terms. The grid points are computed in a preprocessing step and saved in so-called “look-up tables.” During the simulation, the software interacts with look-up tables to get the source terms for the gas species by interpolation of the spline function between the grid points. That approach decouples the calculation of the fluid flow and the numerical treatment of the surface kinetic and provides a faster convergence of the solution in the CFD model requiring less computational time.

CFD model

The CFD simulations are carried out in the commercial finite-volume software Ansys Fluent. A pressure-based, pseudo-transient solver was used for the calculations. The computing of the surface mechanism is performed by use of the aforementioned rate mapping approach. The numerical model contains three dimensional Navier-Stokes equation, mass, and energy conservation, as well as source terms for each gas species, participated in the kinetic mechanism. Temperature depended polynomial functions for viscosity, heat capacity and thermal conductivity of each species are taken from literature [Yaw2010]. Because the reaction is mass transfer controlled, the right choice of diffusion model is extremely important for the prediction of feasible results by the simulations. The Fuller semi-empirically model, kinetic theory model as well as assessable experimental data from literature was compared with each other [Mat1998, Zha2013]. The best match with experimental data was obtained by the model based on kinetic theory [Ful1966, Kee2003].

A pipe reactor with a catalytic gauze inside is chosen as a most obvious form for a bench scale reactor prototype. To hold the conceivable model simple and for the reduction of computational cost, only one catalytic gauze is implemented in the model. Furthermore, the model with just one gauze is better for the investigation and understanding of some fundamental phenomena of ammonia combustion, such as the production of nitrous oxide

and the impact of radiation and turbulence in the reactor. The computational domain contains a steel reactor wall, conventional woven Pt catalytic gauze, and a fluid phase (figure 10.1). To reduce the processing time the computational model was divided into half of the whole reactor based on a symmetry plane.

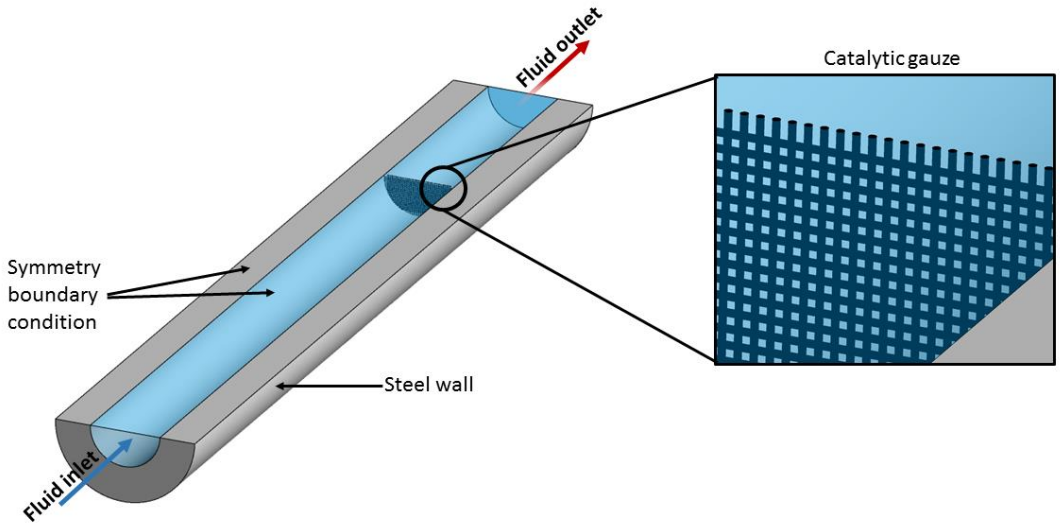

Figure 10.1: The computational domain for the CFD Simulations.

The diameter of the reactor is 10 mm, the reactor length is 150 mm, and the thickness of the steel wall is 5 mm. A second model has also been created with the reactor diameter of 30 mm. Furthermore, a model with symmetry boundary conditions on all wire ends (endless gauze) is used to illustrate the case that approximately occurred in the industrial burner. For that purpose, the geometry is assumed as a square with an edge length equal to reactor diameter (10 mm).

The inlet conditions for the simulations were selected based on typical industrial plant operating parameters. The inlet temperature for the ammonia mixture is 150 °C. A velocity inlet with a uniform velocity profile and velocity magnitude of 0.75 m/s is specified at the reactor entrance. The thermal boundary condition for the outer surface of the steel wall is set to a constant temperature. It is approximately the case as if the wall of a real laboratory scale reactor is heated by the external heat source. The temperature of the steel wall was varied to investigate the thermal wall influence on the catalytically behavior of the gauze. The operating pressure is set to 5 bar, which is a common value for middle-pressure industrial plants. The inlet mixture contains 10-mole fraction oxygen and 20-mole fraction ammonia;

nitrogen is set as ballast medium. All simulations have been carried out without including turbulence or radiation. Except the case where the influence of radiation and turbulence (10 mm reactor and 632 K wall temperature) were examined. For the simulation of turbulence in the fluid flow, k-epsilon model is used with model constants provided by Ansys Fluent. Discrete ordinates model is applied to depict the heat radiation in the catalytic gauze. The emissivity of Pt wires (ε) is 0.17 at 900 °C [Bra1961].

For the discretization of the computational domain non-uniform, the polyhedral mesh is used with an increased resolution in the catalytically active gauze region to provide sufficient results for the surface kinetic calculation. The number of elements amounts seven millions for the model with 10 mm reactor diameter and 21 mi. for the 30 mm. The convergence of the simulations is achieved when residuals of all governing equations are steady state. All results reported in this work are retained from simulations where the convergence criteria for all residuals are smaller than 10^{-5}.

10.2. Results and discussion

To improve the understanding of ammonia oxidation in a small scale laboratory reactor, CFD simulations have been carried out. Figure 10.2 displays the temperature distribution in the reactor domain. Ammonia oxidation is a highly exothermal reaction, which is demonstrated by the temperature rise in the catalytically active gauze region. The catalyst is glowing at the temperature of 1150 K. A similar temperature region for ammonia combustion is observed in the industrial plants as well as reported in several publications [Jes2013, Thi200].

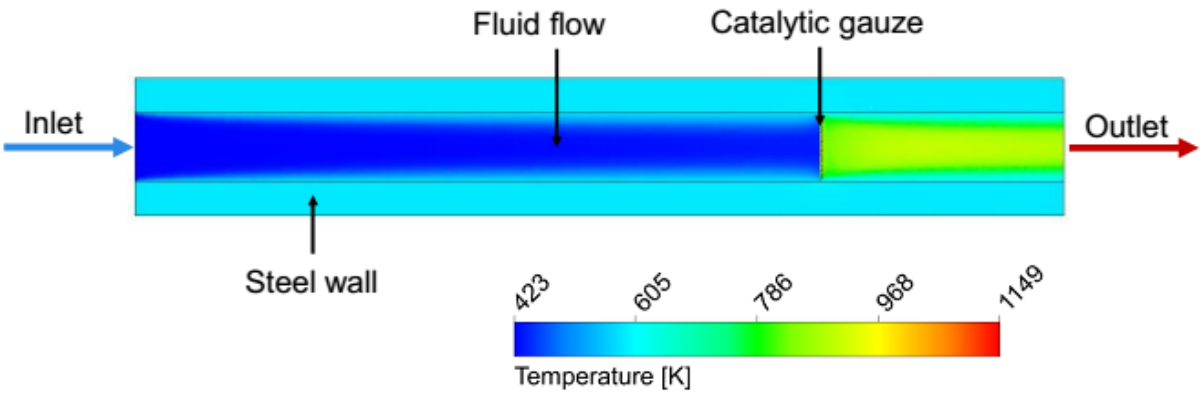

Figure 10.2: Temperature profile of the computational reactor domain during the ammonia combustion. The temperature rises from 423 K (inlet temperature) to 1150 K. The wall temperature is fixed to 623 K.

The N_2O selectivity in the ammonia combustion is highly temperature sensitive. The absolute amount of produced N_2O is small (~ 0.3 %) but the change in the selectivity toward nitrous oxide is well accessible by examining the integral selectivity on outlet or differential selectivity directly on wires. Therefore, the amount of nitrous oxide is a good indicator to investigate the influence of wall effects on gauzes' catalytical behavior.

The NH_3 conversion on outlet amounts to 80 % with an N_2O selectivity of 8.0 % at a steel wall temperature of 623 K. The nitrous oxide selectivity in industrial reactors is reported with 1-2 % dependent on operating pressure.

The use of CFD simulations in that study gives us the possibility of a fast evaluation of the role of turbulence and thermal radiation in the ammonia oxidation process performed in a laboratory scale plant. The temperature distribution along a first wire perimeter (red line in Figure 10.3a) is presented in the Figure 10.3b. The values are taken from four different simulations: with included thermal radiation model (DO-model), with included turbulence model (k-epsilon-model), without consideration of them and from the model with symmetry boundary conditions (endless gauze).

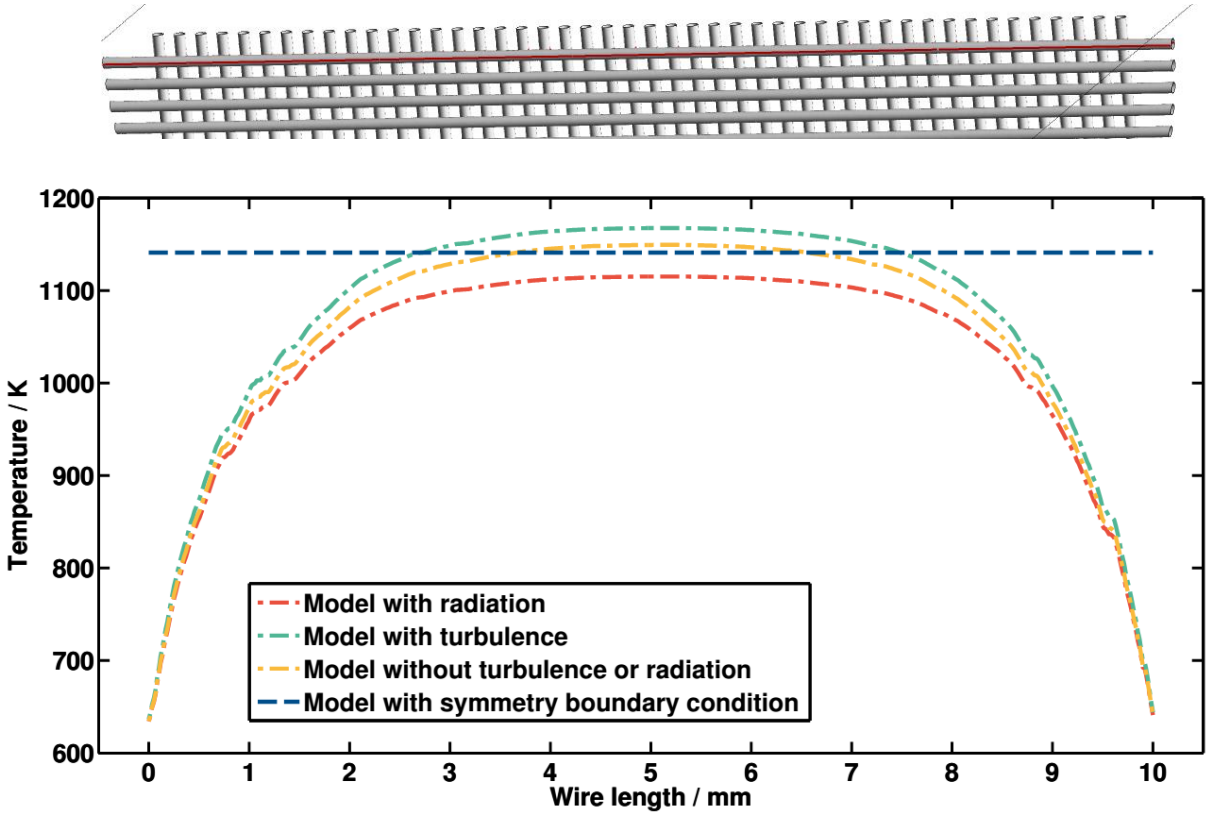

Figure 10.3: (a) Part of the catalytic gauze. The values for the this plot are taken from the first wire in the gauze, along the red line. (b) Temperature distribution along a perimeter of catalytic wire in the models without turbulence and radiation, with included turbulence model, with included radiation model and endless wire model without turbulence and radiation.

It is observable that the temperature is different in the middle of the wire (1168 K in the model with turbulence, 1115 K in the model with radiation and 1149 K in the model without turbulence or radiation) but becomes equalized in the region near the reactor wall in all models. The temperature distribution in the model with symmetry boundary conditions is uniform; the thermal wall effects do not appear.

According to calculated Reynolds numbers (~1500), in the presented model the fluid flow is in the transient region. The evaluation with k-epsilon-model shows that the turbulence has a minor role in the reactor with 10 mm diameter. Higher temperature (~20 K) in the model with included turbulence is explainable by higher NH_3 conversion (82 % with turbulence compared to 80 %), which causes a larger heat production by the reaction.

The radiation has a greater impact on the combustion temperature. The heat loss caused by radiation decreases the wire temperature by 35 K. However, regarding the proportion to the absolute wire temperature it is only ~ 3 %. The small radiation impact can be approved by a

simple estimation and comparison of radiative heat loss with heat loss caused by convection. The heat transferred by convection can be expressed by the following equation 10.1:

$$\dot{Q}_{convection} = \alpha_w \cdot A \cdot (T_{wire} - T_{bulk}) \qquad \text{Eq. 10.1}$$

The radiation heat loss can be calculated by equation 10.2:

$$\dot{Q}_{radiation} = \varepsilon_{Pt} \cdot A \cdot \sigma \cdot ({T^4}_{wire} - {T^4}_{bulk}) \qquad \text{Eq. 10.2}$$

By use of data provided from simulations, it is possible to compute the heat transfer coefficient α_w and calculate the $\dot{Q}_{convection}$ and $\dot{Q}_{radiation}$. The result shows that the proportion of radiation heat loss (0.001 W) to the heat transport caused by convection (0.055 W) is about 2 %. In this estimation is assumed that the first wire radiates in all directions. The detailed influence of radiation on ammonia oxidation in the CFD model is described in the chapter 6. In a technical reactor, where several gauze layers are usual, the contribution of radiative heat loss is smaller because the wire is in radiative interaction with previous and following wires with a similar temperature. The impact of radiation shown here is based on simulations with 5 bar operating pressure. The radiative heat loss become significant at low pressure (1-2 bar) ammonia burners.

Figure 10.4 shows the temperature and the differential N_2O selectivity along a perimeter of the first wire in the gauze (red line). The differential selectivity is calculated by the Eq. 10.3.

$$S_{N_2O} = 200 \cdot \frac{r_{netN_2O}}{r_{netNH_3}} \qquad \text{Eq. 10.3}$$

The net reaction rate $r_{net\ NH3}$ describes the consumption of ammonia in the process. And the net reaction rate r_{netN2O} is the overall production of nitrous oxide.

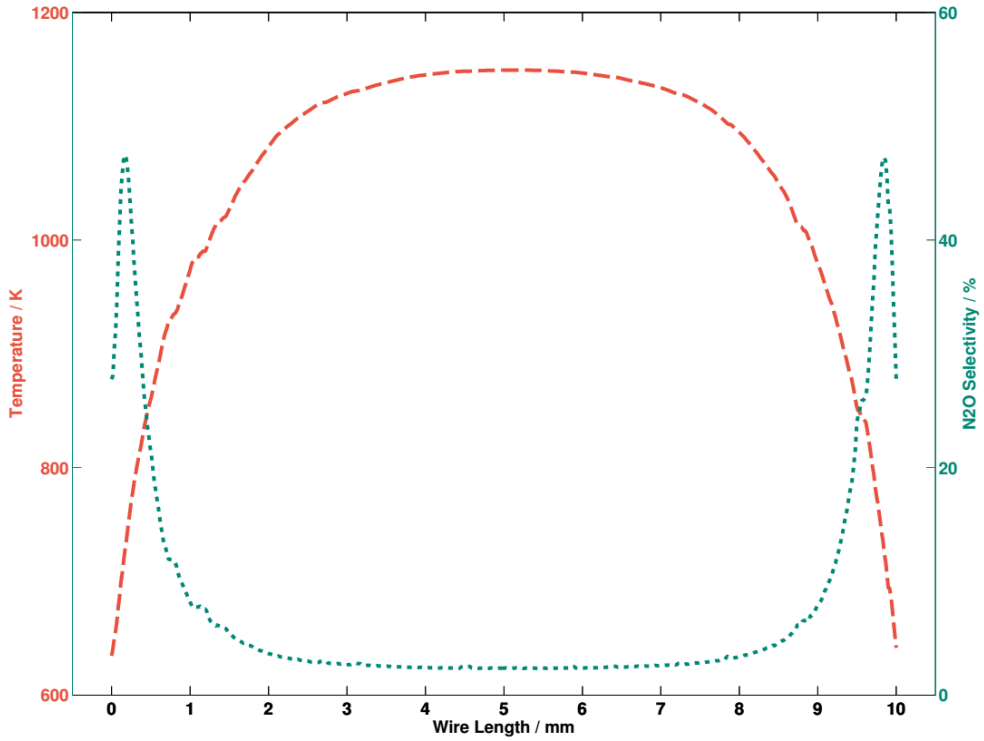

Figure 10.4: The distribution of temperature and N_2O selectivity along the perimeter of the first wire in the gauze (red line).

The results indicate that the temperature and selectivity profiles of the single wire, and according to the entire gauze, are not uniform. 2.5 mm of the wire from each end are influenced by thermal wall effect and do not have an optimal combustion temperature. In Figure 10.5, the scale of cold gauze region is observable. 2.5 mm is 50 % of the wire length and, considering the results regarding gauze surface area, the thermal influenced part amounts to about 75 % of the entire surface area.

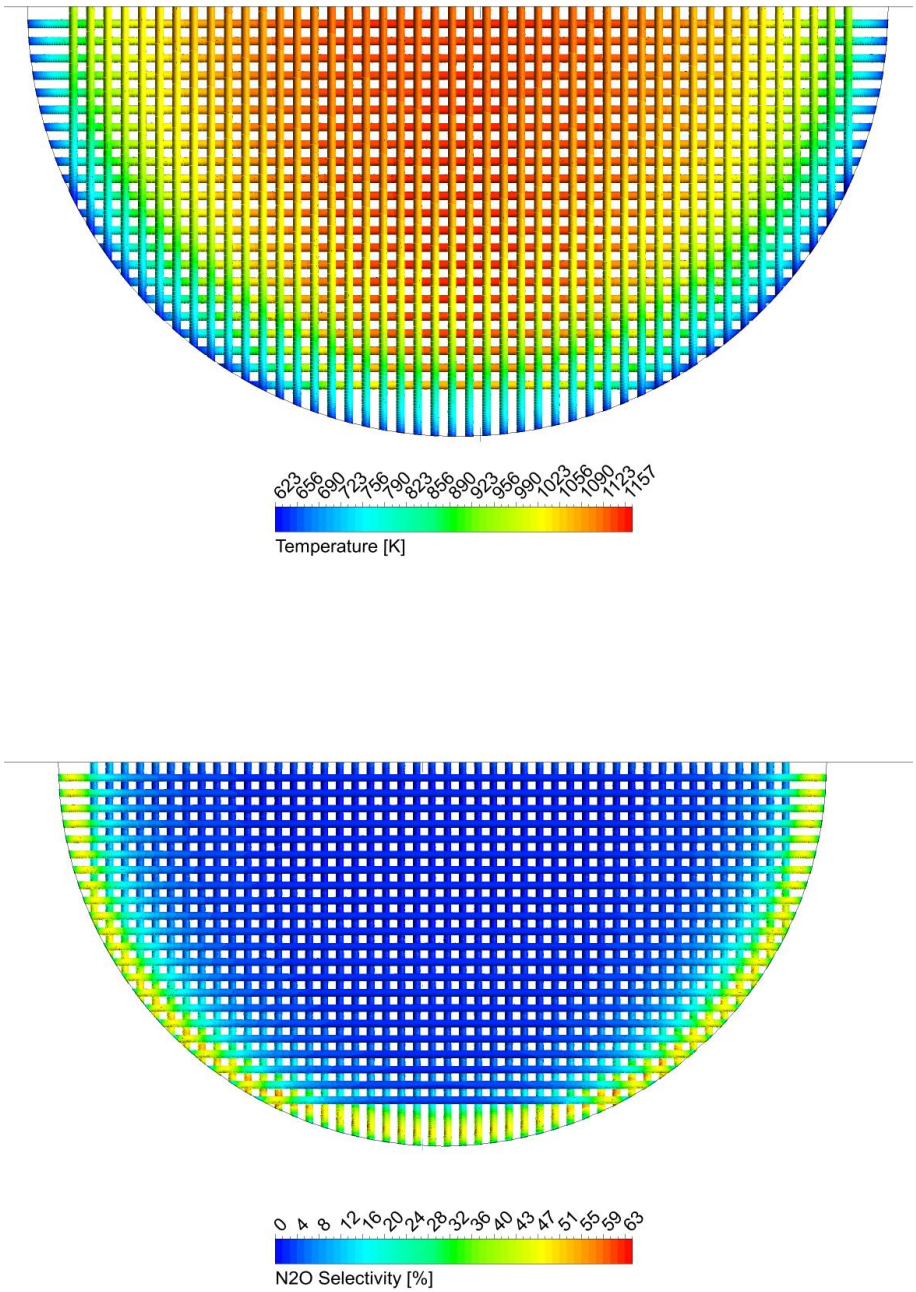

Figure 10.5: (a) Temperature profile, (b) N_2O selectivity profile of the catalytic gauze in the laboratory scale ammonia converter provided by CFD simulation.

Furthermore, the lower temperature is a reason for a rise in the N_2O selectivity. The peak of N_2O production in the used kinetic mechanism is observable at the temperature of 750 K. Those findings show that the thermal wall effect can significantly influence the results provided by the small laboratory scale ammonia converter. On the other hand, the impact

caused by a region of approximately 2.5 mm in an industrial plant with a diameter up to several meters is negligible. The comparability of results provided by laboratory scale reactor with data from industrial plants appears difficult due to described thermal wall effects.

To avoid or diminish the impact of thermal wall effects on the ammonia combustion in a small diameter laboratory reactor, two methods can be applied. The first possibility is to heat the steel wall of the pipe reactor by the external heat source. The second option is to construct a laboratory scale reactor with a larger diameter.

First, we describe the results of simulations with different wall temperatures. In the best case, the real reactor should be well insulated to reduce the heat loss. Furthermore, the temperature of the wall should be held near the combustion temperature. However, most conventional thermocouples allow maximal temperature about 700 °C (973 K), that temperature might be sufficient to stabilize the temperature profile on the gauze and decrease the N_2O selectivity. For the examination of this hypothesis, the reactor wall temperature is varied from 150 to 700 °C (423 – 973 K). Also a simulation with a symmetry boundary condition on the wire ends is performed to illustrate the case that approximately occurred in an industrial plant with a large diameter. Figure 10.6 shows the temperature distribution along the wire perimeter at different wall temperatures.

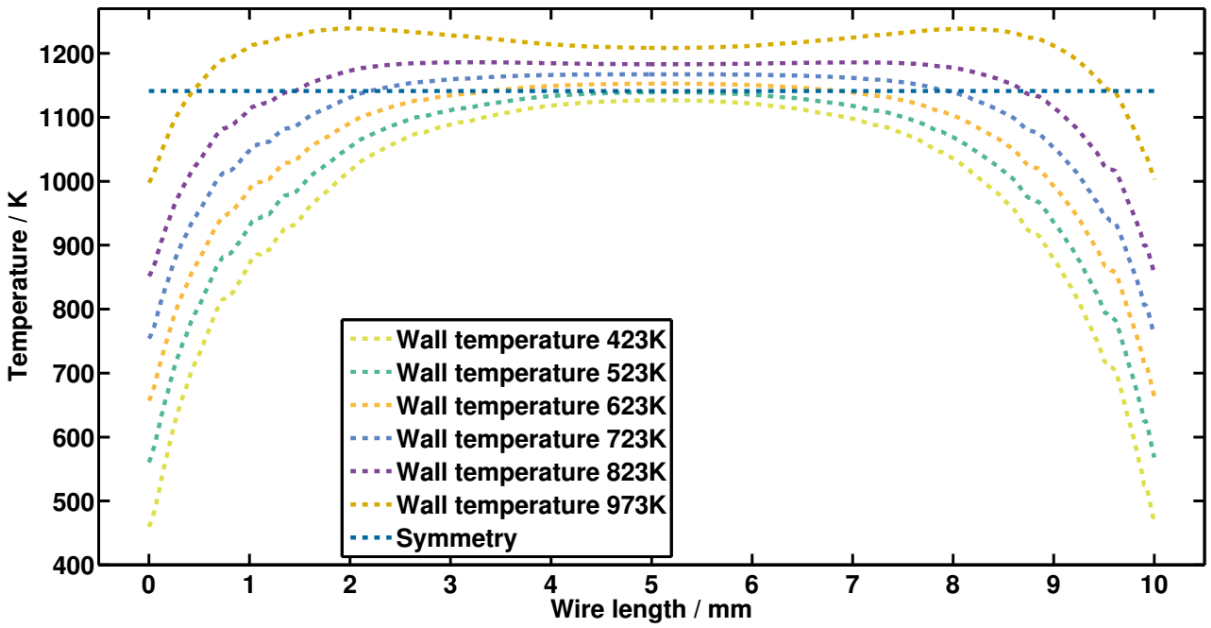

Figure 10.6: Temperature distribution along the wire perimeter at different reactor wall temperature.

The following table 10.1 presents the NH_3 conversion and nitrous oxide selectivity on the outlet of the model.

Table 10.1: Conversion and N_2O selectivity from models with different reactor wall temperature.

The temperature of the reactor wall [K]	NH_3 conversion [%]	N_2O selectivity [%]
423	74.4	10.8
523	79.5	9.7
623	81.1	8.0
723	82.4	4.8
823	83.5	2.8
973	84.9	1.4
Symmetry	83	1.8

The results show that the increase in the wall temperature elevates the ammonia conversion and reduces the amount of N_2O produced by ammonia oxidation. The temperature profile along a perimeter of the wire is similar, but the highest combustion temperature is different in all cases. That observation can be explained by heat produced from exothermal ammonia oxidation reaction. By heating the reactor wall, the cold area in the catalytic gauze is reduced, which leads to a higher ammonia conversion and also to a higher maximal wire temperature. Furthermore, it is observable that the temperature profile in the model with wall heated to 973 K has two maxima and minima in the middle of the wire. Due to the heat transport, the fluid temperature in the wall region is increased. The amount of heat transported by fluid combined with the heat produced by the reaction on the catalyst provides the rise of gauze temperature near the wall (maxima) above the combustion temperature (minima) in the middle of the wire.

That effect is illustrated in Figure 10.7. The temperature shown here is plotted along a line located 0.2 mm in front of the catalytic gauze and parallel to it. The oncoming reaction mixture temperature is higher than the temperature on the inlet of the reactor (~ 60 K by 973 K wall temperature and ~ 8 K by 523 K wall temperature). The temperature falls with

distance to the wall, but even in the middle of the reactor, it is higher compared to the inlet. Due to the higher mixture temperature, the gauze temperature is increased as well.

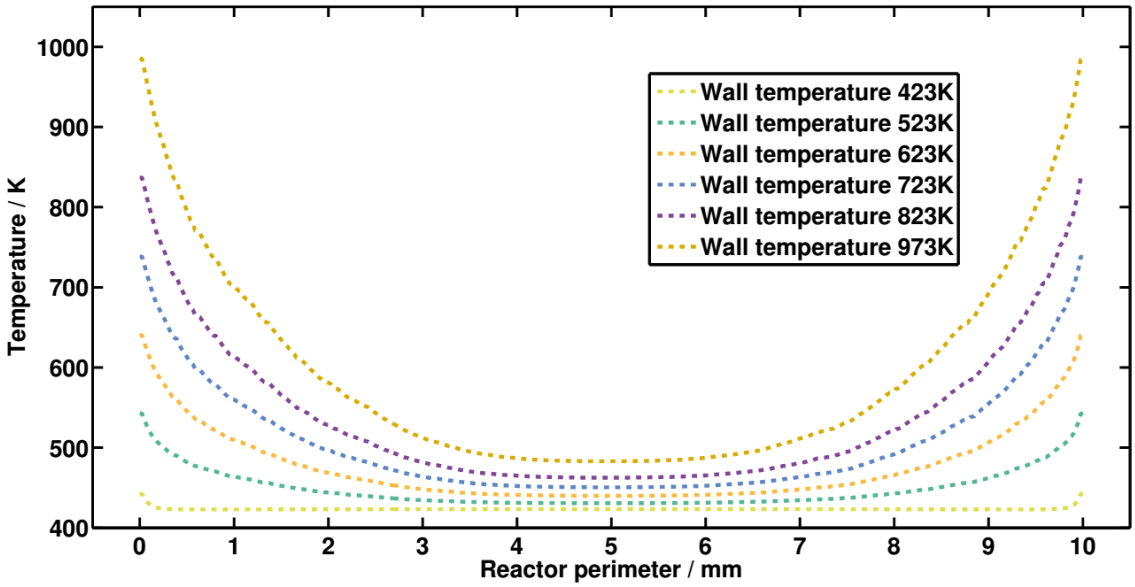

Figure 10.7: The mixture temperature by different wall heating 0.2 mm before the Pt gauze.

High artificial increases of the gauze temperature by heating the reactor wall (wall temperature 600 – 700 °C) lead to higher ammonia conversion as well as lower N_2O selectivity (Figure 10.8) but do not reproduce the conditions in the industrial plant. Furthermore, that aspect can influence the interpretation of the results provided by a laboratory reactor because the assumption that the mixture temperature oncoming on the catalytic gauze is the same as the inlet temperature is incorrect.

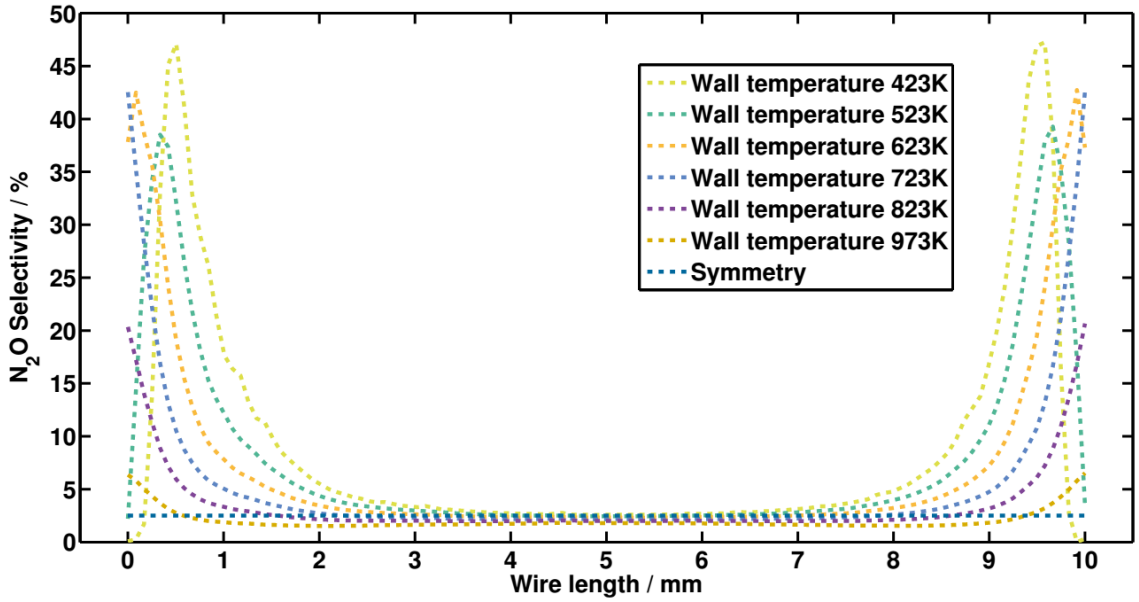

Figure 10.8: The distribution of the nitrous oxide selectivity along a catalytic wire.

Figure 10.8 displays the distribution of the differential N_2O selectivity along a catalytic wire by different reactors' wall temperatures. By heating the reactor wall, it appears possible to shift the maximum of nitrous oxide production. In case of the lowest wall temperature, that peak is located completely on the catalytic wire. By the increase of the wall temperature, the maximum and the cold temperature region move toward the reactor wall and disappear almost completely at a temperature of 700 °C (973 K). Nonetheless, such a high wall temperature leads to the artificial rise of catalyst temperature and a decrease of the N_2O selectivity (minima in the Plot of selectivity at 973 K wall temperature). By the engineering of a laboratory scale ammonia converter, it is reasonable to include external reactor wall heater, which is able to hold a temperature between 600 and 700 °C. That approach decreases the cold gauze area and improves the comparability with a large industrial ammonia burner.

As mentioned before, a second possible way to reduce the impact of the thermal wall effects and improve the ration of cold and hot areas on the catalytic gauze is to increase the diameter of the reactor. Taking into account the limited capabilities of a usual laboratory regarding reactants supply and utilization of products of the ammonia oxidation, the reactor cannot be constructed very large. Nevertheless, depending on the reactor wall temperature, the cold region accounts for about 1-2.5 mm and the beneficial ratio between cold and hot gauze areas can be found by performing CFD simulations of reactors with different diameters.

The following figure 10.9 shows the comparison of wire temperature distribution in the reactor models with 10 mm and 30 mm diameter. Due to symmetry plane, only a half of the wire perimeter is plotted (5 mm by a reactor with 10 mm diameter and 15 mm by a reactor with 30 mm diameter). The integral NH_3 conversion of larger reactor amounts to 86 % with an N_2O selectivity of 4 %, compared to 80 % and 8 % respectively.

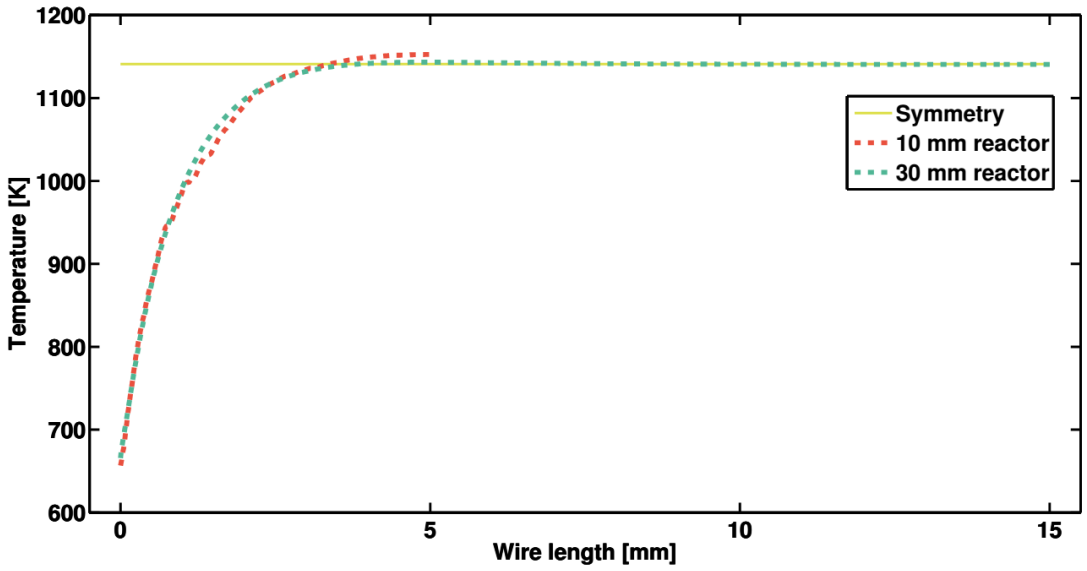

Figure 10.9: Temperature distribution along a wire perimeter in small (10 mm diameter), large (30 mm diameter) reactors and the model with symmetry boundary condition. The wall temperature in 10 mm and 30 mm reactors is set to 632 K.

In that case, the influenced wire part is still ~5 mm (2.5 mm on one end), which is about 16 % of the wire located in the middle of the gauze. The thermal wall effect, in that case, influences only 30 % of overall gauze area, compared to 75 % in case of the reactor with a 10 mm diameter. Furthermore, the wire temperature in the case of a 30 mm reactor and a model with symmetry boundary are aligned, the temperature of the 10 mm reactor gauze is higher. Due to the enlargement of the reactor, the increase in the mixture temperature by wall heating is less significant than in case of a small reactor. The mixture temperature near the catalyst can be assumed equal to inlet temperature.

10.3. Summarizing remarks

Despite more than a century of research, experimental investigation of ammonia combustion process remains challenging. It is shown that complex flow simulations with an included detailed reaction mechanism provide an image of the amount of factors which significantly influence ammonia combustion. The computational model of a small-scaled laboratory reactor indicates several aspects which should be considered:

- The temperature of the catalytic gauze, ammonia conversion and N_2O selectivity are impacted by the thermal transport between the reactor wall and catalyst.
- The external heating of the reactor wall can improve the equalization of the gauze temperature profile and drop the N_2O selectivity.
- The oncoming temperature of the reaction mixture on the catalyst is higher than the inlet temperature by small-sized reactor and intensive external heating. This can lead to significant misinterpretation by analyzing of results provided by a laboratory scale reactor.
- Enlargement of the reactor diameter beneficially increases the hot/cold area ratio of the catalyst and decreases the N_2O selectivity.

Consequently, it is shown that the use of new computational approaches like CFD simulations can improve the understanding of the process. The promise of the approach presented in this contribution is that CFD simulations can support the engineering of a laboratory scale reactor as well as industrial plants.

11. Summary and concluding remarks

The current work set out to understand the ammonia oxidation under industrial conditions. Ammonia oxidation is a step in the production of nitric acid by the Ostwald process. Pt and Pt/Rh knitted and woven gauzes are used as catalyst in the ammonia oxidation. More than 50 million tons of nitric acid are produced worldwide annually in the more than 100 years old Ostwald process. Although the industrial process is very well rationalized and optimized, some of the effects ongoing during the reaction are not completely understood. The most interesting aspects according to the industrial point of view are:

- the reduction of N_2O emission
- rational design of Pt gauzes, which are used as catalysts in the process
- the reduction of the loss of precious metals during the production campaign

The combination of modern computer-based methods allows us to investigate the interplay between mass transfer and kinetics phenomena. The acquired knowledge provides us with the possibility to address the previously mentioned issues, to improve the design of the catalyst and to reduce the emission of nitrous oxide and platinum losses.

Investigation of three major subjects has been made in this work.

- The influence of the gauze geometry and the size and position of the single wire in the catalytic package.
- CFD simulations of restructured wires based on tomography images aiming at better understanding of restructuring process.
- Simulation of laboratory scale reactor and the influence of radiation.

For all models CFD simulations have been performed with a detailed chemical kinetic mechanism, which has been published by Krähnert. The mechanism consists of ten reaction and 6 reaction species. The validation of general trends has been done using experiments in the pilot plant using the same condition and same catalyst geometry.

11.1. Gauze Geometry

The industrial experience shows that knitted catalytic gauzes have a beneficial influence on the ammonia oxidation. The mechanical stability is increased and the production of nitrous oxide is decreased in the reactors, where knitted gauzes are used. Nowadays, the design of the gauze geometry and catalytic package is mostly based on empirical, experiential data. A science-based understanding of this behavior hasn't been presented until now.

The influence of the position of single wires in the gauze has been tested using the combination of computational fluid dynamics and detailed kinetics modeling. It has been shown that the position of the wire to the flow direction plays a significant role in the catalytic performance. Oblique wires to flow direction have better performance and produce less N_2O.

Moreover, in this work it has been shown why knitted gauzes positively influence the process and outperform old woven gauzes. It is suggested that the local mass transfer coefficient, which is different along the catalyst surface, is responsible for the increased or decreased N_2O production. Using the "degree of rate control," including the mass transfer steps, has shown that increased mass transfer coefficients promote nitrous oxide production.

The design of catalyst geometries can be improved using the knowledge which has been acquired by CFD simulations with included detailed kinetics. The geometry of the gauzes can be designed avoiding the area with "hot spot" mass transfer coefficients and increased N_2O production. Furthermore, using the CFD simulations, the prototype for the geometry can be modeled and tested "in silico" without producing a large number of test samples. This will reduce the costs needed for the design process and the time to market for a new catalysts geometry.

11.2. CFD simulations of restructured wires

During the ammonia oxidation process the platinum-rhodium gauzes undergo a morphological change of the catalyst surface. Cauliflower structures appear on the previously smooth wires. This process influences the reaction performance. At the beginning of the production campaign, the selectivity toward N_2O drops slightly during the first 10 to 20 hours of operation. After that period, the catalysts show the best performance. Then the NO selectivity slowly begins to decrease. This can be explained by enrichment of Rhodium on the wires' surface, which is less selective compared to Platinum. Furthermore, the restructuring process leads to a mechanical degradation of the catalyst and loss of Platinum.

There exists a number of published works where the degradation and morphological surface change process is described. Nonetheless, the mechanism of wire restructuring is not completely understood. Furthermore, it is not completely understood how and why the restructuring process influences the reaction performance of ammonia oxidation.

Computational fluid dynamics simulation has been developed based on computer tomography images of the restructured wire. The combination of these two approaches opens a way to understand and investigate the restructuring process from a new point of view.

It has been shown that the selectivity on the restructured surface are not uniform. The cauliflower excrescences are much stronger involved in the ongoing reaction and produce the largest amount of N_2O.

The next step of the investigation of the restructuring mechanism can be the development of the kinetic model for the formation of volatile PtO_2. This model can be coupled with CFD modeling and can provide a dynamic picture of the cauliflower structure's growth.

Better understanding of the restructuring and cauliflower structure growth process can lead to methods for reducing platinum loses and improvement of gauze durability and reaction performance.

11.3. Laboratory scale reactor model

Ammonia oxidation is a very established industrial process. But the investigation of reaction kinetics under industrial conditions remains challenging. For this purpose, a laboratory scale reactor has been built at TU Darmstadt. The reactor is described in the work from Thomas Heydt [Hey2018]. The reactor can reproduce conditions of a middle pressure industrial ammonia burner. A variation of the reaction conditions and their influence on product selectivity can be studied in this reactor. Furthermore, a fast test of different catalyst gauze types becomes possible.

Supporting the practical work, several CFD models of the bench scale reactor have been developed and tested. CFD simulations have been done for reactors with two different diameters (10 and 30 mm). It was found that the 10 mm reactor has very strong wall effects, which influence the production rates of NO and N_2O. The heat loss of the catalyst to the wall has a significant impact. Due to a large catalyst area with a low temperature, the production of N_2O becomes very high. The proportion of NO and N_2O on a reactor outlet is not representative for an industrial ammonia oxidation burner. The enlargement of the reactor

diameter leads to an improvement of production rates, which become similar to industrial observed rates. The cold temperature area of the catalytic gauze gets negligibly small compared to the catalyst area with the proper combustion temperature. It leads to a decrease in the nitrous oxide production rate.

Furthermore, the influence of thermal radiation on reaction performance has been investigated by CFD models. It was found that the radiation in the catalyst package doesn't play a significant role. The heat loss by radiation is considerably smaller than the loss due to convection. The CFD simulations can be performed without taking into account the radiation without any significant impairment of the production rate of NO and N_2O. On the other side, the exclusion of radiation models during CFD simulations considerably accelerate the calculations' time.

Nowadays, the computational power of modern PC and usage of Lichtenberg cluster allowed us to perform very complex and large CFD simulations. Nonetheless, there are still not enough resources for modeling of reactors without making some simplifications. But rising availability of powerful computers, as well as the increasing computational power, will give us a chance to perform increasingly better simulations and to include more complexity in the reactor models.

The developed approach of this work can be used as a basis for a future investigation of ammonia oxidation, reaching from morphological catalyst surface change to CFD modeling of the whole industrial ammonia burner. The developed models not only provide a better understanding of the ammonia oxidation process from an academic point of view but also can be used in commercial improvements of the reactor and the catalytic gauzes.

12. Appendix

12.1. Reaction mechanism

Table 12.1: Lumped mechanism and parameter used in this work. The mechanism is published by Kraehnert and Baerns [Kra208].

#	Reaction equation	A_0 / s^{-1}	E_a / kJ mol^{-1}	b
R1	$NH_3 + Pt_t \longrightarrow NH_3(t)$	1.95×10^2	0	1
R2	$NH_3(t) \longrightarrow NH_3 + Pt_t$	5.45×10^9	61	0
R3	$O_2 + 2\,Pt_h \longrightarrow 2\,O(h)$	8.99×10^1	0	1
R4	$2\,O(h) \longrightarrow O_2 + 2\,Pt_h$	9.37×10^8	181	0
R5	$NH_3(t) + \frac{3}{2}\,O(h) \longrightarrow N(h) + \frac{3}{2}\,H_2O + \frac{1}{2}\,Pt_h + Pt_t$	1.72×10^{15}	100	0
R6	$NO(h) \longrightarrow NO + Pt_h$	8.87×10^{16}	155	0
R7	$NO + Pt_h \longrightarrow NO(h)$	8.84×10^6	64	1
R8	$2\,N(h) \longrightarrow N_2 + 2\,Pt_h$	2.56×10^{17}	139	0
R9	$N(h) + O(h) \longrightarrow NO(h) + Pt_h$	1.93×10^{16}	135	0
R10	$NO(h) + N(h) \longrightarrow N_2O + 2\,Pt_h$	4.00×10^{17}	155	0

a) A_0 in $m^3\,s^{-1}\,mol^{-1}\,K^{-1}$ for R1, R3, R19, R22.

Chemkin file for the implementation of Kraehnert mechanism in Ansys FLUENT.

ELEMENTS

H N O

END

SPECIES

H2O O2 N2O NH3 NO N2

END

SITE/platinum_t/ SDEN/2.7063e-9/

Pt_t_NH3 Pt_t

END

SITE/platinum_h/ SDEN/2.7063e-9/

Pt_h_O Pt_h_N Pt_h_NO Pt_h

END

THERMO ALL

300.0 1000.0 3000.0

Pt_t Pt1 I100.000 50000.000 2000.00 1

0.00000000E+00 0.00000000E+00 0.00000000E+00 0.00000000E+00
0.00000000E+00 2

0.00000000E+00 0.00000000E+00 0.00000000E+00 0.00000000E+00
0.00000000E+00 3

0.00000000E+00 0.00000000E+00 0.00000000E+00 0.00000000E+00
4

Pt_h Pt1 I100.000 50000.000 2000.00 1

0.00000000E+00 0.00000000E+00 0.00000000E+00 0.00000000E+00
0.00000000E+00 2

0.00000000E+00 0.00000000E+00 0.00000000E+00 0.00000000E+00
0.00000000E+00 3

0.00000000E+00 0.00000000E+00 0.00000000E+00 0.00000000E+00
4

Pt_h_N N 1 Pt1 I100.000 50000.000 2000.00 1

0.00000000E+00 0.00000000E+00 0.00000000E+00 0.00000000E+00
0.00000000E+00 2

0.00000000E+00 0.00000000E+00 0.00000000E+00 0.00000000E+00
0.00000000E+00 3

0.00000000E+00 0.00000000E+00 0.00000000E+00 0.00000000E+00
4

Pt_t_NH3 H 3 N 1 Pt1 I100.000 50000.000 2000.00 1

0.00000000E+00 0.00000000E+00 0.00000000E+00 0.00000000E+00
0.00000000E+00 2

0.00000000E+00 0.00000000E+00 0.00000000E+00 0.00000000E+00
0.00000000E+00 3

0.00000000E+00 0.00000000E+00 0.00000000E+00 0.00000000E+00
4

Pt_h_NO N 1 O 1 Pt1 I100.000 50000.000 2000.00 1

0.00000000E+00 0.00000000E+00 0.00000000E+00 0.00000000E+00
0.00000000E+00 2

0.00000000E+00 0.00000000E+00 0.00000000E+00 0.00000000E+00
0.00000000E+00 3

0.00000000E+00 0.00000000E+00 0.00000000E+00 0.00000000E+00
4

Pt_h_O O 1 Pt1 I100.000 50000.000 2000.00 1

0.00000000E+00 0.00000000E+00 0.00000000E+00 0.00000000E+00
0.00000000E+00 2

0.00000000E+00 0.00000000E+00 0.00000000E+00 0.00000000E+00
0.00000000E+00 3

0.00000000E+00 0.00000000E+00 0.00000000E+00 0.00000000E+00
4

END

REACTION KJOULES/MOLE

NH3 + Pt_t => Pt_t_NH3 1950000000 1 0

Pt_t_NH3 => NH3 + Pt_t 54500000000 0 60.9

O2 + 2 Pt_h => 2 Pt_h_O 3.321878579610538e+17 1 0

2 Pt_h_O => O2 + 2 Pt_h 3.462291689760928e+18 0 181

Pt_t_NH3 + 1.5 Pt_h_O => Pt_h_N + 1.5 H2O + 0.5 Pt_h + Pt_t
1.221699906383159e+29 0 99.5

Pt_h_NO => NO + Pt_h 8.87e+17 0 154.8

NO + Pt_h => Pt_h_NO 88400000000000 1 63.5

2 Pt_h_N => N2 + 2 Pt_h 9.459409525921e+26 0 139

Pt_h_N + Pt_h_O => Pt_h_NO + Pt_h 7.131507962901378e+25 0 135.4

Pt_h_NO + Pt_h_N => N2O + 2 Pt_h 1.478032738425156e+27 0 155.2

END

Chemkin file for the implementation of Warner mechanism in Ansys FLUENT.

```
ELEMENTS
O H N
END
SITE/PT_SURFACE/ SDEN/ 2.30E-9/
!!! H/O Species
O(S)
H(S)
OH(S)
H2O(S)
!!! N/NH Species
N(S)
NH(S)
NH2(S)
NH3(S)
!!! NOx Species
NO(S)
N2O(S)
!!! OTHER Species
PT(S)
END
!!! Thermodynamic Data
THERMO ALL
100.0 1000.0 3000.0
NH3(S) 1N 1H 3PT 1 I 100.00 3000.00 1000.00 1
2.17915324E+00 7.26849360E-03-2.69178779E-06 4.54287906E-10-2.71433315E-
14 2
-1.45135907E+04 3.99273891E+00 3.34241379E+00 3.43446639E-03
1.27863243E-06 3
-6.37513111E-10-2.34995874E-13-1.47687903E+04-1.77806641E+00 4
!!! (Offermans et al., 2006) BE = 68 kJ.mol^-1 (DFT)
```

NH2(S) 1N 1H 2PT 1 I 100.00 3000.00 1000.00 1
1.71669018E+00 7.62114962E-03-3.59236475E-06 8.26981980E-10-7.49879804E-14 2
-2.44791589E+03 4.72063218E-01 1.35768510E+00 5.50885006E-03 8.31537399E-06 3
-1.52155765E-08 6.53113642E-12-2.31259253E+03 2.80640104E+00 4
!!! (Ford et al., 2005) BE = 221 kJ.mol^-1 (DFT)
NH(S) 1N 1H 1PT 1 I 100.00 3000.00 1000.00 1
5.86199672E-01 6.84807100E-03-3.91059345E-06 1.08149012E-09-1.16324910E-13 2
-1.54224415E+03-4.31609174E+00-1.28060929E+00 1.51420781E-02-1.73280604E-05 3
1.05016386E-08-2.54620456E-12-1.21901093E+03 4.46151454E+00 4
!!! (Offermans et al., 2006) BE = 387 kJ.mol^-1 (DFT)
N(S) 0N 1PT 1 I 100.00 3000.00 1000.00 1
1.96919325E+00 1.88398288E-03-1.36888064E-06 4.44045369E-10-5.32413516E-14 2
6.16414771E+03-1.09139664E+01-1.59984969E+00 1.95380992E-02-3.41063330E-05 3
2.72327729E-08-8.18958988E-12 6.74870443E+03 5.55922994E+00 4
!!! (Ford et al., 2005) BE = 420 kJ.mol^-1 (DFT)
O(S) 1O 1PT 1 I 100.00 3000.00 1000.00 1
1.92592070E+00 1.99656985E-03-1.41675557E-06 4.41314164E-10-5.05330631E-14 2
-1.50915955E+04-1.01949142E+01-1.31631954E+00 1.95180840E-02-3.46898753E-05 3
2.73919721E-08-8.00734518E-12-1.46653745E+04 4.32238398E+00 4
!!! (Ford et al., 2005) BE = 221 kJ.mol^-1 (DFT)
NO(S) 1N 1O 1PT 1 I 100.00 3000.00 1000.00 1
4.67243631E+00 1.71538940E-03-9.28022686E-07 2.33981646E-10-2.25738433E-14 2
-2.94473136E+03-1.20033669E+01 2.16207431E+00 1.51321550E-02-

2.93812114E-05 3
2.69315104E-08-9.17331742E-12-2.50258937E+03-4.64062062E-01 4
!!! (Gorte et al., 1981) BE = 105 kJ.mol^-1 (TPD)
N2O(S) 1N 2O 1PT 1 I 100.00 3000.00 1000.00 1
3.84168620E+00 5.86084971E-03-3.50595685E-06 9.79852525E-10-1.04543641E-13 2
6.68110228E+03 6.81815687E+00 1.96374556E+00 1.42179821E-02-1.72471250E-05 3
1.09025542E-08-2.76526890E-12 7.01233574E+03 1.56615770E+01 4
!!! (Burch et al., 2004) BE = 16 kJ/mol^-1 (DFT)
OH(S) 92491O 1H 1PT 1 I 100.00 3000.00 1000.00 1
2.30917943E+00 4.26151036E-03-2.29210689E-06 6.07642012E-10-6.32110661E-14 2
-2.07770472E+04-2.02502513E+00 1.40684324E+00 5.08701854E-03 4.58534420E-06 3
-1.20144399E-08 5.75824781E-12-2.05887201E+04 2.69585468E+00 4
!!! (Offermans et al., 2006) BE = 213 kJ.mol^-1 (DFT)
H2O(S) 1O 1H 2PT 1 I 100.00 3000.00 1000.00 1
3.03746527E+00 3.11083573E-03-8.05945292E-07 5.55502687E-11 4.93506619E-15 2
-3.47044200E+04-5.51938562E-01 3.13196626E+00 4.06548042E-03-3.45299906E-06 3
2.10771977E-09-4.49326348E-13-3.48160821E+04-1.40633721E+00 4
!!! (Fisher et al., 1980) BE = 40 kJ.mol^-1 (TPD)
230
H(S) 0H 1PT 1 I 100.00 3000.00 1000.00 1
1.25010550E+00 1.94380290E-03-9.30291952E-07 2.11966754E-10-1.87836301E-14 2
-4.14155140E+03 1.50875130E+00 2.03803156E+00-3.79595190E-04 6.42739939E-07 3
8.84393013E-10-7.28769748E-13-4.31823172E+03-2.44381249E+00 4
!!! (Offermans et al., 2006) BE = 261 kJ.mol^-1 (DFT)

PT(S) PT 1 S 100.0 3000.0 1000.0 1

0.00000000E+00 0.00000000E+00 0.00000000E+00 0.00000000E+00

0.00000000E+00 2

0.00000000E+00 0.00000000E+00 0.00000000E+00 0.00000000E+00

0.00000000E+00 3

0.00000000E+00 0.00000000E+00 0.00000000E+00 0.00000000E+00 4

PT(B) PT 1 S 100.0 3000.0 1000.0 1

0.00000000E+00 0.00000000E+00 0.00000000E+00 0.00000000E+00

0.00000000E+00 2

0.00000000E+00 0.00000000E+00 0.00000000E+00 0.00000000E+00

0.00000000E+00 3

0.00000000E+00 0.00000000E+00 0.00000000E+00 0.00000000E+00 4

!!! Surface-Coverage Dependent Enthalpy of Oxygen

HFCOV

O(S) O(S) -3608

END

END

REACTIONS JOULES/MOLE USRPROD

!!! ADSORBTION REACTIONS

!!! Reaction 1 (based on Gohndrone, 1989)

NH3 + PT(S) = NH3(S) 3.00E-02 0.00 0.0

STICK

!!! Reaction 2 (Park, 1999}

O2 + 2PT(S) = 2O(S) 3.00E-02 0.00 0.0

STICK

!!! Reaction 3 (Park, 1999; Forsth, 2002)

H2O + PT(S) = H2O(S) 7.00E-01 0.00 0.0

STICK

!!! Reaction 4 (Deutschmann et al., 2000; Försth, 2002)

H2 + 2PT(S) = 2H(S) 4.60E-02 0.00 0.0

STICK

!!! AMMONIA ACTIVATION

!!! Reaction 5 (Offermans et al., 2006)

NH3(S) + O(S) = NH2(S) + OH(S) 5.22E+20 0.00 42000

!!! Reaction 6 (Offermans et al., 2006)

NH2(S) + O(S) = NH(S) + OH(S) 2.66E+21 0.00 87000

!!! Reaction 7 (Offermans et al., 2006)

NH(S) + O(S) = N(S) + OH(S) 3.31E+21 0.00 84000

!!! Reaction 8 (Offermans et al., 2006)

NH3(S) + OH(S) = NH2(S) + H2O(S) 6.97E+19 0.00 73000

!!! Reaction 9 (Offermans et al., 2006)

NH2(S) + OH(S) = NH(S) + H2O(S) 1.48E+21 0.00 22000

!!! Reaction 10 (Offermans et al., 2006)

NH(S) + OH(S) = N(S) + H2O(S) 2.22E+20 0.00 35000

!!! Reaction 11 (Offermans et al., 2006)

NH3(S) + PT(S) = NH2(S) + H(S) 2.44E+20 0.00 93000

!!! Reaction 12 (Offermans et al., 2006)

NH2(S) + PT(S) = NH(S) + H(S) 2.18E+21 0.00 110000

!!! Reaction 13 (Offermans et al., 2006)

NH(S) + PT(S) = N(S) + H(S) 3.13E+21 0.00 118000

!!! SURFACE WATER MECHANISM

!!! Reaction 14 (Park, 1999)

O(S) + H(S) = OH(S) + PT(S) 4.35E+19 0.00 50626

COV/O(S) 0.0 0.0 5440/

COV/H(S) 0.0 0.0 -13810/

!!! Reaction 15 (Park, 1999)

H2O(S) + O(S) = OH(S) + OH(S) 4.35E+19 0.00 52718

COV/O(S) 0.0 0.0 89900/

!!! Reaction 16 (Park, 1999)

OH(S) + H(S) = H2O(S) + PT(S) 4.35E+18 0.00 51882

COV/O(S) 0.0 0.0 -51880/

COV/H(S) 0.0 0.0 -12970/

!!! SURFACE MECHANISM and DISORBTIONS

!!! Reaction 17 (Asscher et al., 1984; Rebrov et al., 2002)

N(S) + O(S) = NO(S) + PT(S) 4.35E+21 0.00 121200

!!! Reaction 18 (based on Zhu, 2003)

NO + PT(S) = NO(S) 9.00E-01 0.00 0.0

231

STICK

!!! Reaction 19 (Rebrov et al., 2002)

2N(S) = N2 + 2PT(S) 4.35E+19 0.00 79100

!!! Reaction 20 (Dumesic, 1993; Rebrov, (2002, 2003)}

N(S) + NO(S) = N2O(S) + PT(S) 4.35E+18 0.00 92900

!!! Reaction 21 (Traversac, 2008}

N2O(S) = N2 + O(S) 2.00E+14-0.45 154700

!!! Reaction 22: (Traversac, 2008}

N2O + PT(S) = N2O(S) 2.00E-03 0.00 0.0

STICK

END

12.2. Look up tabulation

For the acceleration of calculation time of CFD simulations hermite rate maps have been used. Detailed description of using Look up tabulation approach for ammonia oxidation is given in the thesis of Klingenberger [Kli2017b].

Precalculated in FORTRAN code steady state source terms of a set of gas phase species are stored in the Look up tables as a function of the relevant dimensions. The source terms are calculated with Eq 13.1.

$$\dot{s}_i = \Gamma F_\Gamma \sum_j \upsilon_{i,j} r_j \qquad \text{Eq. 12.1}$$

Γ ist he site density, F_Γ is the surface enlargement factor (10), $\upsilon_{i,j}$ is the stoichiometric coefficient of specie I, r_j is the reaction rate.

Three key species, NH_3, N_2O and N_2 have been chosen as key species and the source terms of this species have been calculated. Three tables are required for this scheme. The source terms of other species can be calculated according to the reaction scheme via stoichiometric considerations (Eq. 13.2 – 13.4) [Kli217b].

$$\dot{s}_{O_2} = \frac{5}{4}\dot{s}_{NH_3} + \frac{2}{2}\dot{s}_{N_2} + \frac{1}{2}\dot{s}_{N_2O} \qquad \text{Eq. 12.1}$$

$$\dot{s}_{H_2O} = -\frac{4}{6}\dot{s}_{NH_3} \qquad \text{Eq.12.2}$$

$$\dot{s}_{NO} = -\frac{4}{4}\dot{s}_{NH_3} - \frac{4}{2}\dot{s}_{N_2} + \frac{4}{2}\dot{s}_{N_2O} \qquad \text{Eq.12.3}$$

12.3. Species properties

Following values has been used in all models for molar weights, enthalpy and entropy of formation for reactions species.

Table 12.2: Used values for molar weight, enthalpy and entropy of formation.

Species	M / g mol^{-1}	$\Delta_f H^{298.15\,K}$ / kJ mol^{-1}	$\Delta_f S^{298.15\,K}$ / J mol^{-1} K^{-1}
O_2	31.99	0	205.04
NH_3	17.03	-45.9	192.63
NO	30.00	90.29	210.65
N_2	28.01	0	191.51
N_2O	44.01	82.06	219.88
H_2O	18.02	-241.84	188.71

The heat capacity C_p, viscosity η_m and thermal conductivity λ_m of the mixture are calculated as the mole-weighted average of the individual species properties in the software Ansys FLUENT according to eq 12.4 – 12.6.

$$C_p, m = \sum \chi_i \, C_{p,i} \qquad \text{Eq. 12.4}$$

$$\eta_m = \sum \chi_i \, \eta_i \qquad \text{Eq.12.5}$$

$$\lambda_m = \sum \chi_i \, \lambda_i \qquad \text{Eq.12.6}$$

The polynomials used in the simulations are listed in the tables 12.2-.12.4

Table 12.3: The coefficients used for the calculation of temperature-dependent heat capacity of each species. The polynomial is $C_{p,l}(T) = A_i + B_iT + C_iT^2 + D_iT^3 + E_iT^4$

Species	A / J kg^{-1} K^{-1}	B / J kg^{-1} K^{-2}	C J/ kg -1 K^{-3}	D J/ kg^{1} K^{-4}	E J/ kg^{-1} K^{-5}
O_2	922.68	-0.28	0.0012	-1.12e0-6	2.76e-10
NH_3	1974.88	-0.74	0.0052	-4.22e-6	1.9e-09
NO	1107.57	-0.79	0.0018	-1.26e-06	3.04e-10
N_2	1047.92	-0.13	0.00036	-1.54e-07	9.26e-12
N_2O	527.7	1.41	-0.00086	1.58e-07	1.85e-11
H_2O	1885.17	-0.47	0.0017	-9.903e-07	2.5e-10

Table 12.4: The coefficients used for the calculation of temperature-dependent viscosity of each species. The polynomial is $\eta_m(T) = A_i + B_iT + C_iT^2 + D_iT^3$

Species	A / kg $m^{-1}s^{-1}$	B / kg $m^{-1}s^{-1}K^{-1}$	C J/ kg $m^{-1}s^{-1}K^{-2}$	D / kg $m^{-1}s^{-1}K^{-3}$
O_2	-4.94e-07	8.07e-08	-4.04e-11	1.01e-14
NH_3	-7.62e-07	3.67e-08	-4.71e-13	4.8e-17
NO	-6.24e-08	7.38e-08	-3.76e-11	9.26e-15
N_2	4.47e-07	6.38e-08	-2.66e-11	5.41e-15
N_2O	-1.52e-06	6.13e-08	-2.48-11	5.32e-15
H_2O	2.28e-08	1.74e-08	3.24e-11	-1.43e-14

Table 12.5: The coefficients used for the calculation of temperature-dependent thermal conductivity of each species. The polynomial is $\lambda_m(T) = A_i + B_iT + C_iT^2 + D_iT^3 + E_iT^4 ++ F_iT^5$

Species	A / W $m^{-1}K^{-1}$	B / W $m^{-1}K^{-2}$	C W $m^{-1}K^{-3}$	D W $m^{-1}K^{-4}$	E/W $m^{-1}K^{-5}$	F/ W $m^{-1}K^{-6}$
O_2	0.0088	5.26e-05	4.79e-08	-6.11e-11	2.82e-14	-4.49e-18
NH_3	-0.021	0.0002	-2.07e-07	3.39e-10	-2.22e-13	5.19e-17
NO	0.0057	8.09e-05	-3.63e-08	5.58e-11	-4.47e-14	1.23e-17
N_2	-0.0037	0.00014	-2.22e-07	2.72e-10	-1.62e-13	3.68e-17
N_2O	-0.0056	7.96e-05	7.09e-09	-9.01e-12	-5.51e-15	3.68e-18
H_2O	0.011	-2.66e-05	2.7e-07	-1.4e-10	5.29e-14	-6.65e-18

The diffusion coefficients of species in the mixture (Di,m) are calculated according to the eq. 12.7

$$D_{i,m} = \frac{1 - X_i}{\sum_{j,j \neq i} X_j / D_{ij}} \qquad \text{Eq. 12.7}$$

here X_i is the mole fraction of species i in the mixture, D_{ij} is the binary diffusion coefficient of species i in species j.

The temperature dependent binary diffusion coefficients are calculated according to the following polynomial:

$$D_{ij}(T) = A_0 + A_1 T + A_2 T^2 + A_3 T^3 + A_4 T^4 + A_5 T^5 \qquad \text{Eq. 12.8}$$

The factor for the polynomials are given on the next page in the table 12.6

Table 12.6: polynomial factors for the calculations of binary diffusion coefficients.

Stoffe i, j	D_{ij} / $m^2 s^{-1}$					
	A_0	A_1	A_2	A_3	A_4	A_5
N_2, O_2	-5,664620 10^{-7}	6,186878 10^{-9}	3,639719 10^{-11}	-1,353205 10^{-14}	5,162264 10^{-18}	-9,044900 10^{-22}
N_2, NH_3	-6,647336 10^{-7}	5,960731 10^{-9}	4,545821 10^{-11}	-1,845477 10^{-14}	7,305542 10^{-18}	-1,305120 10^{-21}
N_2, NO	-5,858139 10^{-7}	5,635366 10^{-9}	3,844106 10^{-11}	-1,511216 10^{-14}	5,908251 10^{-18}	-1,049030 10^{-21}
N_2, N_2O	-4,023660 10^{-7}	2,745272 10^{-9}	3,707327 10^{-11}	-1,653713 10^{-14}	6,733894 10^{-18}	-1,216400 10^{-21}
N_2,H_2O	4,789802 10^{-8}	-2,690304 10^{-9}	7,208239 10^{-11}	-3,424392 10^{-14}	1,363913 10^{-17}	-2,392960 10^{-21}
O_2, NH_3	-6,733189 10^{-7}	6,759411 10^{-9}	4,353771 10^{-11}	-1,678511 10^{-14}	6,508976 10^{-18}	-1,150780 10^{-21}
O_2, NO	-5,716859 10^{-7}	6,115301 10^{-9}	3,669088 10^{-11}	-1,375846 10^{-14}	5,269677 10^{-18}	-9,254000 10^{-22}
O_2, N_2O	-4,632176 10^{-7}	3,792459 10^{-9}	3,436911 10^{-11}	-1,450013 10^{-14}	5,816289 10^{-18}	-1,045230 10^{-21}
O_2, H_2O	-2,518342 10^{-7}	-4,515544 10^{-11}	6,887435 10^{-11}	-3,282918 10^{-14}	1,337239 10^{-17}	-2,393660 10^{-21}
NH_3, NO	-6,625794 10^{-7}	5,783188 10^{-9}	4,628122 10^{-11}	-1,901480 10^{-14}	7,559729 10^{-18}	-1,353250 10^{-21}
NH_3, N_2O	-3,619380 10^{-7}	1,836299 10^{-9}	4,639876 10^{-11}	-2,153286 10^{-14}	8,818235 10^{-18}	-1,592000 10^{-21}
NH_3, H_2O	4,630071 10^{-6}	-3,993456 10^{-8}	1,433338 10^{-10}	-1,765678 10^{-13}	1,306577 10^{-16}	-3,547018 10^{-20}
NO, N_2O	-3,817961 10^{-7}	2,470908 10^{-9}	3,754792 10^{-11}	-1,692875 10^{-14}	6,908016 10^{-18}	-1,248290 10^{-21}
NO, H_2O	1,199644 10^{-7}	-3,298939 10^{-9}	7,344023 10^{-11}	-3,468028 10^{-14}	1,369991 10^{-17}	-2,387360 10^{-21}
N2O, H_2O	6,448520 10^{-7}	-6,158896 10^{-9}	6,001135 10^{-11}	-2,103722 10^{-14}	6,195776 10^{-18}	-8,177800 10^{-22}

13. Bibliography

Ahl1999 A. F. Ahlström-Silversand, C. U. I. Odenbrand, *Chemical Engineering Journal* **1999**, *73*, 205–216.

And1926 L. Andrussow. *Angew. Chem.*, **1926**, *39*, 321-332.

And1926a L. Andrussow. *Ber. Dtsch. chem. Ges.*, **1926**, *59*, 458-461.

And1927 L. Andrussow. *Angew. Chem.*, **1927**, *40*, 166-174.

And1927a L. Andrussow. *Ber. Dtsch. chem. Ges.*, **1927**, *60*, 536-540.

And1927b L. Andrussow. *Ber. Dtsch. chem. Ges.*, **1927**, *60*, 2005-2018.

And1927c L. Andrussow. *Z. Anorg. Allg. Chem.*, **1927**, *166*, 60-62.

And1928 L. Andrussow. *Angew. Chem.*, **1928**, *41*, 205-206.

And1928a L. Andrussow. *Angew. Chem.*, **1928**, *41*, 262-263.

And1951 L. Andrussow. Angew. Chem., **1951**, 15, 350-355.

Ape1948 L. Apel'baum, M. Temkin,

Zhurnal fizicheskoi khimii **1948**, *22*, 179–194.

App2000 M. Appl, *Ullmann's Encyclopedia of Industrial Chemistry*, Wiley-VCH Verlag GmbH & Co.KGaA, Weinheim, Online-Version, **2000**.

Bae2005 M. Baerns, R. Imbihl, V. A. Kondratenko, R. Krähnert, W. K. Offermans, R. A. van Santen, A. Scheibe, *J. Catal.*, **2005**, *232*, 226-238.

Bae2006 M. Baerns, A. Behr, A. Brehm, J. Gmehling, H. Hofmann, U. Onken, A. Renken, *Technische Chemie*, WILEY-VCH Verlag GmbH & Co. KGaA, Weinheim, **2006**.

Ber1996 E. Bergene, O. Tronstad, A. Holmen, *J. Catal.*, **1996**, 160, 141-147.

Bir1906 K. Birkeland, *Trans. Faraday Soc.*, **1906**, 2, 98-116.

Van2006 V. Vantchurin, E. Golovnya, E. Bruschtein, *kataliz v promishlenosti*, **2006**, 5, 52-57

Bod1922 Bodenstein, *Z. Phys. Chem.*, **1922**, *100*, 68-123.

Bod1927 M. Bodenstein, *Angew. Chem.*, **1927**, *40*, 174-177.

Bod1935 M. Bodenstein, *Z. Elektrochem.*, **1935**, *41*, 466.

Bod1935a M. Bodenstein, *Helvetica Chimica Acta*, **1935**, *18*, 743-759.

Bod1941 M. Bodenstein, *Z. Elektrochem.*, **1941**, *47*, 501-518.

Bod1942 M. Bodenstein, W. Krauß, A. v. Nagel, *Z. Elektrochem.*, **1942**, *48*, 167.

Bra1995 J. M. Bradley, A. Hopkinson, D. A. King, *J. Phys. Chem.*, **1995**, *99*, 17032-17042.

Bra1997 J. M. Bradley, A. Hopkinson, D. A. King, *Surf. Sci.*, **1997**, *371*, 255-263.

Bur2002 R. Burch, S. T. Daniells, P. Hu, *J. Chem. Phys.,* **2002***, 117*, 2902-2908.

Bur2004 R. Burch, S. T. Daniells, J. P. Breen, P. Hu*, J. Catal.*, **2004**, *224*, 252-260.

Cam1994 C. T. Campell, *Topics in Catalysis* **1994**, *1*, 353–366.

Cam2001 C. T. Campell, *Journal of Catalysis* **2001**, *204*, 520?524.

Chi1968 T. H. Chilton, "*Strong Water Nitric Acid: Sources and Methods of Manufacture and Uses*". **1968**, Cambridge: MIT Press.

Con1967 H. Connor, *Platinum Metals Rev.*, **1967**, *11*, 2-9.

Dea1988 V. W. Dean, M. Frenklach, J. Phillips, *J. Phys. Chem.*, **1988**, *92*, 5731-5738.

Del2014 A. Della Torre, G. Montenegro, G.R. Tabor, M.L. Wears, *Int. J. Heat Fluid Fl.*, **2014**, 50, 72-82

Deu1996 O. Deutschmann, R. Schmidt, F. Behrendt, J. Warnatz, J.,

Symposium (International) on Combustion **1996**, *26*, 1747–1754.

Edx2015 Online Course from EDX, "*A hands-on Introduction to Engineering Simulations*". **2015**

Eyd1909 S. Eyde, *J. of the Royal Society of Arts*, **1909**, *57(2949)*, 568-576.

Fan2016 X. Fan, et al., *Catal. Today*, 2016,

Fer2008 J. H. Ferziger, M. Peric, *Numerische Strömungsmechanik*, Springer-Verlag, Berlin Heidelberg, **2008**.

Fog1964 Y. M. Fogel, B. T. Nadykto, V. F. Rybalko, V. I. Shvachko, I. E. Korobchanskaya, *Kinetika i Kataliz*, *1964*, *5(3)*, 496-504.

For2005 D. C. Ford, Y. Xu, M. Mavrikakis, *Surf. Sci.,* **2005***, 587*, 159-174.

Ful1966 E. N. Fuller, P. D. Schettler, J. C. Giddings, *Ind. Eng. Chem.*, **1966**, *58(5)*, 18-27.

Gla1978 J.L. Gland, V.N. Korchak, J. Catal. 53, **1978**, 9

Gla1980 J.L. Gland, B.A. Sexton, G. B. Fischer, *Surf. Sci*., **1980**, 587

Goh1986 J.M. Gohndrone, C. W. Olsen, A. L. Backman, T. R. Gow, E. Yagasaki, R. I. Masel, J. Vac, *Sci. Technol. A*, **1986**, 7(3), 1986-1990

Han2005 L. Hannevold, O. Nilsen, A. Kjekshus, H. Fjellvåg, *Appl. Catal. A: General*, **2005**, *284*, 163-176.

Haa2016 M. Haas, *Master Thesis*, TU Darmstadt, **2016**

Hec1982 R. M. Heck, J. C. Bonacci, W. R. Hatfield, T. H. Hsiung, *Ind. Eng. Chem. Process Des. Dev.*, **1982**, *21*, 73-79.

Hen1824 W. Henry, Phil. Trans, Phil. Trans

Hen2012 J. Henderson Jr., *Computational Fluid Dynamics: The Basics with Applications*, McGraw Hill Education, New Delhi, **2012**

Hes1992 J. Hess, J. Phillips, *J. Catal.*, **1992**, *136*, 149-160.

Hey2018 T. Heydt, *PhD Thesis*, TU Darmstadt, **2018.**

Hor1991 B. Horner, *Platinum Metals Rev.*, **1991**, *35(2)*, 58-64.

Hor1993 B. Horner, *Platinum Metals Rev.*, 1993, 37(2), 76-85.

Imb2007 R. Imbihl, A. Scheibe, Y. F. Zeng, S. Gunther, R. Kraehnert, V. A. Kondratenko, M.Baerns, W. K. Offermans, A. P. J. Jansen, R. A. van Santen, R. A., *Phys. Chem. Chem. Phys.*, **2007**, *9*, 3522-3540.

Jes2013 A. Jess, P. Wasserscheid, Chemical Technology: An Integral Textbook, Wiley-VCH, Weinheim, **2013**.

Kee2003 R. J. Kee, M. E, Coltrin, P. Glarborg, *Chemically Reacting Flow Theory and Practice*, John Wiley & Sons Inc., Hoboken, U.S.A., **2003**.

Kli2017a M. Klingenberger, O. Hirsch, M. Votsmeier, *Comput. Chem. Eng*., **2017**, 98, 21-30.

Kli2017b M. Klingenberger, *Dissertation*, TU Darmstadt, **2017**.

Kon2005 E. V. Kondratenko, J. Pérez-Ramirez, *Applied Catalysis A: General,* **2005***, 289*, 97–103.

Kra2005 R. Krähnert, *Dissertation*, TU Berlin, **2005**.

Kra2008 R. Krähnert, M. Baerns, M. *Chem. Eng. J.,* **2008***, 137*, 361-375.

Lyu1994 M. Lyubovsky, V. Barelko, *J. Catal*., **1994**, 149, 23-35.

Mar1972 P. Mars, D. van Krevelen, *Chem. Eng. Sci*., **1954**, 3, 41-59.

Mas1998 W. Massmann, *Atmos. Environ*., **1998**, 32, 1112-1127.

Mat1998 N. Matsunage, M. Hori, A. Nagashima, *Nippon Kikai Gakkai Fonbunshu, B-Hen* **1998**, 64, 1433-1439.

McC1983 A. R. McCabe, G. D. W. Smith, *Platinum Metals Rev.*, **1983**, *27(1)*, 19-25.

McC1986 A. R. McCabe, G. D. W. Smith, A. S. Pratt, *Platinum Metals Rev.*, **1986**, *30(2)*, 54-62.

McG199 H. A. McGee, *Molecular Engineering*, McGraw-Hill Inc., US, **1991**.

Mit1953 A. Mittasch, *Salpetersäure aus Ammoniak*, Verlag Chemie GmbH, Weinheim, **1953**.

Nie2013 T. Nien, J. Mmbaga, R. Hayes, M. Votsmeier, *Chemical Engineering Science* **2013**, *93*, 362–375.

Nie2013a T.-W. Nien, PhD thesis, University of Alberta, **2013**.

Nil2001 O. Nilsen, A. Kjekshus, H. Fjellvåg, *Applied Catalysis A: General*, **2001**, *207*, 43-54.

Nov2005 G. Novell-Leruth, A. Valcárcel, A. Clotet, J. M. Ricart, J. Pérez-Ramirez, *J. Phys. Chem. B,* **2005***, 109*, 18061-18069.

Nov2008 G. Novell-Leruth, J. M. Ricart, J. Pérez-Ramirez, *J. Phys. Chem. C,* **2008***, 112*, 13554-13562.

Owe2016 B. Owen, Proc *IMechE Part H: J Engineering in Medicine*, **2016**, 230(3), 201-210.

Per2001 J. Pérez-Ramirez, F. Kapteijn, G. Mul, J. A. Moulijn, *Chem. Commun.,* **2001**, 693-694

Per2003 J. Pérez-Ramirez, F. Kapteijn, K. Schöffel, J. A. Moulijn, *Applied Catalysis B: Environmental*, **2003**, *44*, 117-151.

Per2004 J. Pérez-Ramirez, E. V. Kondratenko, *Chem. Commun.,* **2004**, 376-377.

Per2004a J. Pérez-Ramirez, E. V. Kondratenko, V. A. Kondratenko, M. Baerns, *J. Catal. ,* **2004***, 227*, 90-100.

Per2005 J. Pérez-Ramirez, E. V. Kondratenko, V. A. Kondratenko, M. Baerns, *J. Catal.,* **2005***, 229*, 303–313.

Per2005a J. Pérez-Ramirez, B. Vigeland, *Angew. Chem. Int. Ed.*, **2005**, *44*, 1112-1115.

Per2007 J. Pérez-Ramirez, E. V. Kondratenko, *J. Catal.,* **2007***, 250*, 240-246.

Per2009 J. Pérez-Ramirez, E. V. Kondratenko, G. Novell-Leruth, J. M. Ricart, *J. Catal.,* **2009***, 261*, 217-223.

Pet1999 L. Petzold, "*Design of New DASPK for Sensitivity Analysis*", **1999**

Pur2013 J. Pura, et al., *Catal. Today*, **2013**, 208, 48-55

Pur2015 J. Pura, et al., *Solid State Phenom*., **2015**, 227, 229-232

Pur2016 J. Pura, et al., *Applied Surface Science*, **2016**, *388*, 670-677.

Raf2012 M. Rafti, J. L. Vicente, A. Albesa, A. Scheibe, R. Imbihl, *Surf. Sci.,* **2012***, 606*, 12-20.

Ran2014 P. Ranut, E. Nobile, L. Mancini, *Appl. Therm. Eng*., **2014**, 69, 230-240

Tay2013 C. A. Taylos, T. A. Fonte, J. K. Min*, J. Am. Coll. Cardiol*., **2013**, 61, 2233-2241.

tkIS2017 Thyssenkrupp Industrial Solution booklet, 2017, URL: https://d2zo35mdb530wx.cloudfront.net/_binary/UCPthyssenkruppBAIS/en/products-and-services/fertilizer-plants/nitrate-plants/nitric-acid-plants/link-tkis-brochure-nitric-acid-screen--002-.pdf

Reb2001 E. Rebrov, M. de Croon, J. Schouten, *Catalysis Today,* **2001***, 69*, 183-192.

Reb2002 E. Rebrov, M. de Croon, J. Schouten, *Chem, Eng. J.*, **2002**, *90*, 61-76.

Reb2003 E. Rebrov, M. de Croon, J. Schouten, *Chem. Eng. Res. Des.*, **2003**, *81*, 744-752.

Reb2003a E. Rebrov, S. Duinkerke, M. de Croon, J. Schouten, *Chem. Eng. J.,* **2003***, 93*, 201-216.

Sat1970 C. N. Satterfield, D. H. Cortez, *Industrial & Engineering Chemistry Fundamentals* **1970**, *9*, 613–620.

Sch1990 M. Schaefer, „*Numerik im Maschinenbau*“, Springer-Verlag, Berlin Heidelberg, **1990**.

Sch2003 A. Scheibe, *Dissertation*, Universität Hannover, Hannover, Germany, **2003**.

Sch2003a A. Scheibe, S. Günther, R. Imbihl, *Catal. Let.*, **2003**, *86*, 33-37.

Sch2005 A. Scheibe, M. Hinz, R. Imbihl, *Surf. Sci.*, **2005**, *576*, 131-144.

Sch2005a A. Scheibe, U. Lins, R. Imbihl, *Surf. Sci.*, **2005**, *577*, 1-14.

Sha1974 M. A. Shah, D. Roberts, *Adv. Chem. Ser.*, **1975**, *133*, 259-270.

Thi2000 M. Thiemann, E. Scheibler, K. W. Wiegand, *Ullmann's Encyclopedia of Industrial Chemistry*, Wiley-VCH Verlag GmbH & Co. KGaA, Weinheim, Online-Version, **2000**.

Tra2007 X. Traversac, *Ph.D.-Thesis*, University of Sydney, Australien, **2007**.

Uhde2017 ThyssenKrupp Industrial Solutions, *Nitric acid – a true all-rounder*,

https://www.thyssenkrupp-industrial-solutions.com/de/produkte-undservices/duengemittelanlagen/nitrate-plants/nitric-acid-plants/, Firmenbroschüre online abgerufen am **21.02.2017.**

Umi2006 M. Schleth, Beitrag von Umicore AG & Co.KG Platinum Engineered Materials zur ANNA 2009 in Little Rock, http://pem.umicore.com/storage/pem/publicationpem-anna-

2009.pdf, online abgerufen am **05.01.2017.**

Vot2009 M. Votsmeier, *Chemical Engineering Science* **2009**, *64*, 1384–1389.

Vot2010 M. Votsmeier, A. Scheuer, A. Drochner, H. Vogel, J. Gieshoff,

Catalysis Today **2010**, *151*, 271–277.

Wan2014 C.-C. Wang, J.-Y. Wu, T. L. M. Pham, J.-C. Jiang, *ACS Catal.*, **2014**, *4*, 639-648.

War2013 M. Warner, *Ph.D.-Thesis*, University of Sydney, Australien, **2013**.

War2015 M. Warner, B. S. Haynes, *Proceedings of the Combustion Institute,* **2015***, 35*, 2215-2222.

Wu1985 N. L. Wu, J. Phillips, *J. Phys. Chem.*, **1985**, *89*, 591-600.

Wu1988 N. L. Wu, J. Phillips, *J. Catal.*, **1988**, *113*, 129-143.

Yaw2009 C. L. Yaws, *Transport properties of chemicals and hydrocarbons*, Elsevier Inc., Oxford, U.K., **2009**.

Zer2014 E. Zermatten, et al., *Ann. Biomeg. Eng*., **2014**, 42(5), 1085-2094.

Zha2013 Yu. I. Zhavrin, V. N. Kosov, I. V. Poyarkov, M. K. Asembaeva, O. V. Fedorenko, A. T. Naysanbaeva, Journal of Engeneering Physics and Thermophysics, **2013**, 86, 676.

Artur Wiser 27.08.2020

Europa-Allee 121

60486 Frankfurt am Main

Erklärung

Ich erkläre hiermit, dass ich meine Dissertation selbstständig und nur mit den angegebenen Hilfsmitteln angefertigt noch keinen Promotionsversuch unternommen habe.

Frankfurt, den 27.08.2020

Artur Wiser

Artur Wiser 27.08.2020

Europa-Allee 121

60486 Frankfurt am Main

Erklärung

Ich erkläre hiermit, dass die vorliegende elektronische Version meiner Dissertation identisch mit der vorliegenden schriftlichen Fassung ist.

Frankfurt, den 27.08.2020

Artur Wiser